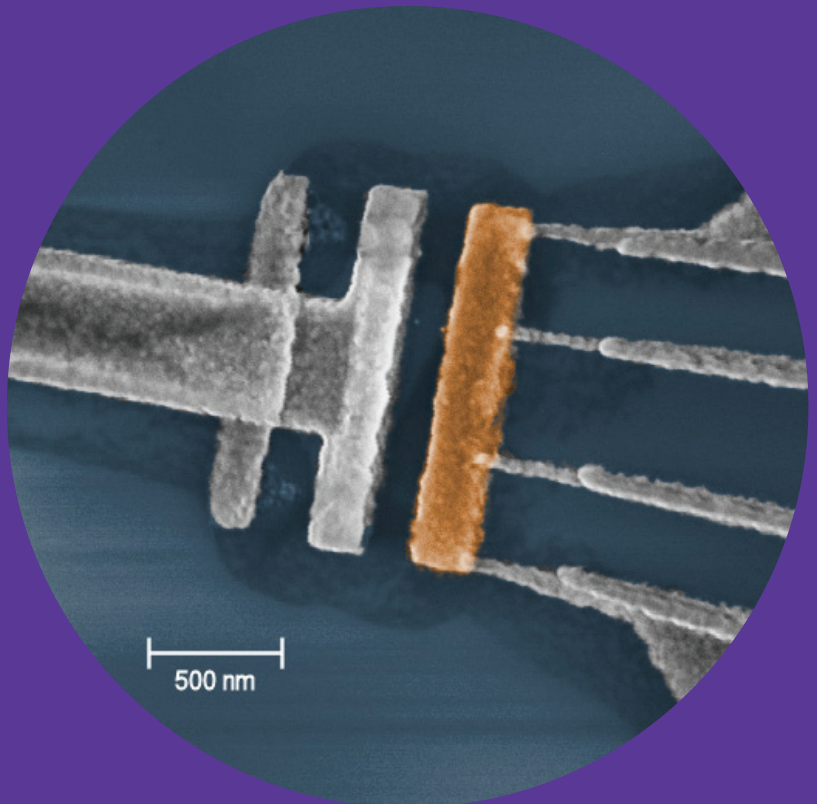


# Electrostatic control of quasiparticle transport in superconducting hybrid nanostructures

---

Olli-Pentti Saira



# Electrostatic control of quasiparticle transport in superconducting hybrid nanostructures

**Olli-Pentti Saira**

A doctoral dissertation completed for the degree of Doctor of Technology to be defended, with the permission of the Aalto University School of Science, at a public examination held at the lecture hall TUAS1 on March 28, 2013 at noon.

**Aalto University**  
**School of Science**  
**Olli V. Lounasmaa Laboratory**  
**PICO group**

**Supervising professor**

Jukka Pekola

**Thesis advisor**

Mikko Möttönen

**Preliminary examiners**

Teun Klapwijk, TU Delft, Netherlands

Joel Ullom, NIST, United States

**Opponent**

Gerd Schön, Universität Karlsruhe, Germany

Aalto University publication series

**DOCTORAL DISSERTATIONS** 48/2013

© Olli-Pentti Saira

ISBN 978-952-60-3628-1 (printed)

ISBN 978-952-60-5076-8 (pdf)

ISSN-L 1799-4934

ISSN 1799-4934 (printed)

ISSN 1799-4942 (pdf)

<http://urn.fi/URN:ISBN:978-952-60-5076-8>

Unigrafia Oy

Helsinki 2013

Finland

Publication orders (printed book):

[osaira@gmail.com](mailto:osaira@gmail.com)

**Author**

Olli-Pentti Saira

**Name of the doctoral dissertation**

Electrostatic control of quasiparticle transport in superconducting hybrid nanostructures

**Publisher** School of Science**Unit** Olli V. Lounasmaa Laboratory**Series** Aalto University publication series DOCTORAL DISSERTATIONS 48/2013**Field of research** Low temperature physics**Manuscript submitted** 11 December 2012**Date of the defence** 28 March 2013**Permission to publish granted (date)** 31 January 2013**Language** English **Monograph** **Article dissertation (summary + original articles)****Abstract**

A flow of electric current in a metal is the result of the collective motion of mobile conduction electrons within a relatively static background formed by ionized atoms. An electric current of 1 ampere used in everyday appliances corresponds to a flow rate of about  $6 \cdot 10^{18}$  electrons per second. In this thesis, I have studied experimentally and theoretically certain metallic nanostructures where electric charge can be measured and transported at a precision of one electron.

Before this thesis, single-electron effects in hybrid structures consisting of superconductors (S) and normal metals (N) had not been thoroughly investigated. Many of the new results presented in this thesis concern the SINIS-type single-electron transistor. This structure consists of superconducting source and drain electrodes with a normal metallic island in between. The island is contacted to the electrodes via tunnel junctions (I). Due to a phenomenon known as the Coulomb blockade, the electric and heat currents through the transistor can be significantly altered by changing the gate charge by a fraction of the elementary charge.

Several physical phenomena in the SINIS transistor were observed for the first time in the experiments of this thesis: We showed that the cooling power incident on the normal metal of the transistor can be modulated by the gate charge. We also demonstrated that the SINIS transistor can be used as an electron turnstile. The electric current through the turnstile is equal to the product of the elementary charge and the frequency of an external driving signal. A device that realizes this current-frequency-dependence with a sufficiently high accuracy could be used in electrical metrology in the future.

As an important technological advance in the study of hybrid structures, we demonstrate that single-electron tunneling events between a superconductor and a normal metal can be detected in real time with a capacitively coupled single-electron transistor. By counting individual electrons, electric currents less than 1 attoampere can be measured, which is impossible with traditional room-temperature electronics. By measuring the rate of electron tunneling events, we were able to study the coupling of high frequency microwaves and so-called nonequilibrium quasiparticles to the measured samples. Finally, we have determined the distribution of heat dissipated in the process of charging a metallic island by a single electron.

**Keywords** tunnel junctions, Coulomb blockade, electronic transport, superconductivity, quasiparticles in superconductors, nonequilibrium thermodynamics

**ISBN (printed)** 978-952-60-3628-1**ISBN (pdf)** 978-952-60-5076-8**ISSN-L** 1799-4934**ISSN (printed)** 1799-4934**ISSN (pdf)** 1799-4942**Location of publisher** Espoo**Location of printing** Helsinki**Year** 2013**Pages** 195**urn** <http://urn.fi/URN:ISBN:978-952-60-5076-8>



**Tekijä**

Olli-Pentti Saira

**Väitöskirjan nimi**

Kvasipartikkelien kuljetuksen hallinta hilajännitteellä nanomittakaavan suprajohde-normaalimetalli-hybridirakenteissa

**Julkaisija** Perustieteiden tiedekunta**Yksikkö** Olli V. Lounasmaa -laboratorio**Sarja** Aalto University publication series DOCTORAL DISSERTATIONS 48/2013**Tutkimusala** Matalien lämpötilojen fysiikka**Käsikirjoituksen pvm** 11.12.2012**Väitöspäivä** 28.03.2013**Julkaisuluvan myöntämispäivä** 31.01.2013**Kieli** Englanti **Monografia** **Yhdistelmäväitöskirja (yhteenveto-osa + erillisartikkelit)****Tiivistelmä**

Metallisessa johtimessa kulkeva sähkövirta syntyy vapaiden johtavuuselektronien liikkeestä verrattain liikkumattomien ionien muodostamassa hilassa. Arkipäiväisen sähkölaitteen käyttämä 1 ampeerin virta vastaa noin  $6 \cdot 10^{18}$  elektronin virtausta sekunnissa. Tässä väitöskirjassa on tutkittu kokeellisesti ja teoreettisesti metallisia nanorakenteita, joissa sähkövarauksen mittaaminen ja liikuttelu eri johtimien välillä on mahdollista yksittäisen elektronin tarkkuudella.

Ennen tätä väitöskirjaa yksielektroni-ilmiöitä ei ollut tutkittu kattavasti suprajohteita (S) ja normaalimetalleja (N) sisältävissä niin sanotuissa hybridirakenteissa. Monet väitöskirjan tuloksista koskevat SINIS-tyyppin yksielektronitransistoria. Tämä rakenne koostuu suprajohtavista lähde- ja nieluelektrodeista sekä niiden välissä olevasta normaalimetallisesta saarekkeesta, joka on kytketty elektrodeihin tunneliliitoskontakteilla (I). Coulombin saarroksi kutsutun ilmiön vuoksi alkeisvarauksen murto-osan suuruiset muutokset SINIS-transistorin hilavarauksessa voivat aiheuttaa merkittävän muutoksen transistorin sähkö- ja lämpövirrassa.

Väitöskirjaan kuuluvissa kokeissa havaittiin monia fysikaalisia ilmiöitä SINIS-transistoreissa ensimmäistä kertaa: Osoitimme, että transistorin normaalimetalliin kohdistuvaa jäähdytystehoa voidaan säätää muuttamalla transistorin hilavarausta. Demonstroimme myös SINIS-transistorin käytön elektronien kääntöporttina, jonka läpi kulkeva sähkövirta on alkeisvarauksen ja ulkoisen ajataajuuden tulo. Kääntöporttia, joka toteuttaa tämän taajuusvirta-riippuvuuden riittävän tarkasti, voitaisiin käyttää tulevaisuudessa sähköisten suureiden metrologiassa.

Tärkeänä mittausteknisenä edistysaskeleena väitöskirjassa näytetään kokeellisesti, että yksittäisten elektronien tunneleminen normaalimetallin ja suprajohteen välillä voidaan havaita reaaliajassa kapasitiivisesti kytketyllä yksielektronitransistorilla. Yksittäisten alkeisvarausten laskeminen mahdollistaa alle 1 attoampeerin sähkövirtojen mittaamisen, mikä on mahdotonta perinteisellä huoneenlämpötilassa toimivalla elektroniikalla. Selvittämällä elektronien tunnelointitapahtumien taajuuden saimme tietoa korkeataajuisien mikroaaltojen sekä niin sanottujen epätasapainokvasipartikkelien kytketymisestä mitattuihin näytteisiin. Lisäksi määritimme jakauman lämpö määrälle, joka dissipoituu, kun metallisen saarekkeen varausta muutetaan yhdellä alkeisvarauksella käyttämällä ulkoista hilaelektrodia.

**Avainsanat** tunneliliitokset, Coulombin saarto, elektronien kuljetusilmiöt, suprajohtavuus, kvasipartikkelit suprajohteissa, epätasapainotermodynamiikka

**ISBN (painettu)** 978-952-60-3628-1**ISBN (pdf)** 978-952-60-5076-8**ISSN-L** 1799-4934**ISSN (painettu)** 1799-4934**ISSN (pdf)** 1799-4942**Julkaisupaikka** Espoo**Painopaikka** Helsinki**Vuosi** 2013**Sivumäärä** 195**urn** <http://urn.fi/URN:ISBN:978-952-60-5076-8>



# Preface

This thesis documents the scientific research results and findings to which I have contributed while working in the PICO group lead by professor Jukka Pekola. I first joined the group as a research assistant in the summer 2006 when it belonged to the Low Temperature Laboratory of Helsinki University of Technology. When I finally ended my graduate studies around the New Year's Eve of 2013, the laboratory was known as the O. V. Lounasmaa laboratory (OVLL) of Aalto University. Despite the passing of years and natural in- and out-flux of group members, the day-to-day life of working in the group stayed much the same: under Jukka's supervision, it was always easy to focus on essential research questions and the grass-roots level work needed to get things done. Without a doubt, he deserves the greatest acknowledgement for making this thesis a reality.

My history with the advisor of this thesis, docent Mikko Möttönen, starts one year earlier, in the year 2005. I thank him for introducing me to the standards and conventions of the physics community via the assignments and, later, publications that I authored in his group. Since then, we have maintained a close and straightforward companionship in matters both related and unrelated to physics, which has greatly benefited the completing of this thesis.

Most of the new results reported in this thesis are based on measurements of very small artifacts at very low temperatures – smaller than 1 micrometer at less than 0.1 kelvin above the absolute zero. To realize such measurements, the physicist, or a student aspiring to become one, must master various technical skills ranging from electron beam lithography to mechanical design and operating of complex gas-handling systems. To a large extent, these techniques were taught hands-on to me by Dr. Matthias Meschke, to whom I'm grateful for his patience.

For helpful advice, honest feedback, and insightful questions related to my research I wish to thank also professor Pertti Hakonen, staff scientist Alexander Savin, docent Tero Heikkilä, and senior scientist Sorin Paraoanu from OVLL, and research leader Antti Manninen from MIKES.

For the opportunity to do my graduate studies in Aalto University and OVLL, I wish to thank the former director of the laboratory, professor Mikko Paalanen, the head of the Applied Physics department, professor Matti Kaivola, and the professor in charge of my graduate course program, Risto Nieminen. For the access to the cleanroom facilities of Micronova nanofabrication center, I thank director Veli-Matti Airaksinen, process engineer Paula Heikkilä, and the rest of the cleanroom staff. I'm grateful to the secretaries of the OVLL for their invaluable assistance in dealing with the formalities of the university administration. I thank the staff of the OVLL mechanical workshop, especially foreman Arvi Isomäki and technician Markku Korhonen, for realizing my mechanical designs and pointing out why some of them could not be realized.

As important as the role of administration and support staff is, the big picture of the graduate school experience is shaped by the daily interactions with fellow students and post-doc level researchers. At times when my life seemed to be a part of my PhD project, and not the other way around, I was privileged to be sharing office space, equipment access, and free time with great people such as Juha Vartiainen, Antti Kemppinen, Andrey Timofeev, Tommy Holmqvist, Sergey Kafanov, Nikolai Chekurov, Thomas Aref, Paolo Solinas, Youngsoo Yoon, Hung Nguyen, Wonjae Kim, Antti Peltonen, Joonas Peltonen, Juha Muhonen, Ville Maisi, Simone Gasparinetti, Timothe Faivre, Jonne Koski, and Klaara Viisanen. I wish to devote a special acknowledgement to Anna Feshchenko for the unforgettable time I spent instructing her Master's thesis with one hand in a cast due to a broken wrist.

I thank Väisälä Foundation and the Finnish Academy of Science and Letters for funding three years of my graduate studies.

Finally, I am grateful to my parents Pentti and Sinikka Saira for an endless supply of love and support.

Delft, February 25, 2013,

Olli-Pentti Saira

# Contents

<b>Preface</b>	<b>i</b>
<b>Contents</b>	<b>iii</b>
<b>List of Publications</b>	<b>v</b>
<b>Author's Contribution</b>	<b>vii</b>
<b>1. Introduction</b>	<b>1</b>
<b>2. Theoretical basis</b>	<b>5</b>
2.1 Quasiparticle transport in tunnel junctions . . . . .	5
2.1.1 Orthodox theory of single-electron tunneling . . . . .	5
2.1.2 Evaluation of tunneling matrix elements . . . . .	8
2.2 Circuit considerations . . . . .	12
2.2.1 $P(E)$ theory . . . . .	12
2.2.2 Charging energy . . . . .	18
2.3 Superconducting structures . . . . .	22
2.3.1 Quasiparticles in BCS superconductors . . . . .	22
2.3.2 The NIS junction . . . . .	24
2.4 Heat flows in mesoscopic systems . . . . .	31
<b>3. Experimental methods</b>	<b>37</b>
3.1 Sample fabrication . . . . .	37
3.2 Refrigeration . . . . .	40
3.3 Electrical wiring and shielding . . . . .	41
3.4 Electron counting with SETs . . . . .	44
<b>4. Results on NIS devices</b>	<b>51</b>
4.1 Gate control of electronic refrigeration . . . . .	51
4.2 Effect of the electromagnetic environment . . . . .	56

4.3	Sub-gap processes in SINIS single-electron transistors . . .	63
4.4	A quantized current source: The SINIS turnstile . . . . .	68
4.5	Statistical mechanics of driven single-electron transitions .	73
<b>5.</b>	<b>Numerical methods</b>	<b>81</b>
5.1	Master equations for single-electron transport . . . . .	81
5.2	Computation of the distribution of dissipated heat in a driven two-level system . . . . .	84
	<b>Bibliography</b>	<b>87</b>
	<b>Publications</b>	<b>93</b>

# List of Publications

This thesis consists of an overview and of the following publications which are referred to in the text by their Roman numerals.

**I** J. P. Pekola, F. Giazotto, and O.-P. Saira. Radio-Frequency Single-Electron Refrigerator. *Phys. Rev. Lett.*, **98**, 037201 (4 pages), 2007.

**II** O.-P. Saira, M. Meschke, F. Giazotto, A. M. Savin, M. Möttönen, J. P. Pekola. Heat Transistor: Demonstration of Gate-Controlled Electron Refrigeration. *Phys. Rev. Lett.*, **99**, 027203 (4 pages), 2007.

**III** J. P. Pekola, J. J. Vartiainen, M. Möttönen, O.-P. Saira, M. Meschke, D. V. Averin. Hybrid single-electron transistor as a source of quantized electric current. *Nature Phys.*, **4**, 120–124, 2008.

**IV** J. P. Pekola, V. F. Maisi, S. Kafanov, N. Chekurov, A. Kemppinen, Yu. A. Pashkin, O.-P. Saira, M. Möttönen, J. S. Tsai. Environment-Assisted Tunneling as an Origin of the Dynes Density of States. *Phys. Rev. Lett.*, **105**, 026803 (4 pages), 2010.

**V** O.-P. Saira, M. Möttönen, V. F. Maisi, J. P. Pekola. Environmentally Activated Tunneling Events in a Hybrid Single-Electron Box. *Phys. Rev. B*, **82**, 155443 (6 pages), 2010.

**VI** S. V. Lotkhov, O.-P. Saira, J. P. Pekola, and A. B. Zorin. Single-charge escape processes through a hybrid turnstile in a dissipative environment. *New J. Phys.*, **13**, 013040 (14 pages), 2011.

- VII** A. Kemppinen, S. V. Lotkhov, O.-P. Saira, A. B. Zorin, J. P. Pekola, and A. J. Manninen. Long hold times in a two-junction electron trap. *Appl. Phys. Lett.*, **99**, 142106 (3 pages), 2011.
- VIII** V. F. Maisi, O.-P. Saira, Yu. A. Pashkin, J. S. Tsai, D. V. Averin, and J. P. Pekola. Real-time observation of discrete Andreev tunneling events. *Phys. Rev. Lett.*, **106**, 217003 (4 pages), 2011.
- IX** O.-P. Saira, A. Kemppinen, V. F. Maisi, and J. P. Pekola. Vanishing quasiparticle density in a hybrid Al/Cu/Al single-electron transistor. *Phys. Rev. B*, **85**, 012504 (4 pages), 2012.
- X** J. P. Pekola and O.-P. Saira. Work, free energy and dissipation in voltage driven single-electron transitions. *J. Low Temp. Phys.*, **169**, 70–76, 2012.
- XI** O.-P. Saira, Y. Yoon, T. Tanttu, M. Möttönen, D. Averin, J. Pekola. Test of Jarzynski and Crooks fluctuation relations in an electronic system. *Phys. Rev. Lett.*, **109**, 180601 (5 pages), 2012.

# Author's Contribution

## **Publication I: "Radio-Frequency Single-Electron Refrigerator"**

The author wrote the master-equation based simulation code and performed the simulations with it.

## **Publication II: "Heat Transistor: Demonstration of Gate-Controlled Electron Refrigeration"**

The author carried out a significant part of the sample fabrication and measurements. He analyzed the data, and wrote the manuscript.

## **Publication III: "Hybrid single-electron transistor as a source of quantized electric current"**

The author performed initial simulations that eventually led to the experiments. He did part of the sample fabrication and participated in the measurements.

## **Publication IV: "Environment-Assisted Tunneling as an Origin of the Dynes Density of States"**

The author performed calculations and simulations supporting the main theoretical result.

## **Publication V: "Environmentally Activated Tunneling Events in a Hybrid Single-Electron Box"**

The author carried out most of the sample fabrication, measurements, and data analysis, and wrote most of the manuscript.

**Publication VI: “Single-charge escape processes through a hybrid turnstile in a dissipative environment”**

The author suggested the theoretical model and used it to simulate the experiments.

**Publication VII: “Long hold times in a two-junction electron trap”**

The author carried out a part of the measurements. In the notation of the journal article, the author's measurements are those performed in cryostat C<sub>B</sub>.

**Publication VIII: “Real-time observation of discrete Andreev tunneling events”**

The author implemented the measurement setup for real-time detection of tunneling events and assisted in data analysis.

**Publication IX: “Vanishing quasiparticle density in a hybrid Al/Cu/Al single-electron transistor”**

The author carried out most of the study, except for the fabrication of the reference sample and a part of the measurements. In the notation of the journal article, the measurements in cryostat PT were done by one of the coauthors.

**Publication X: “Work, free energy and dissipation in voltage driven single-electron transitions”**

The author carried out a significant part of the theoretical studies and wrote a part of the manuscript.

**Publication XI: “Test of Jarzynski and Crooks fluctuation relations in an electronic system”**

The author designed the sample, did most of the measurements, analyzed the data, and wrote the manuscript.

# 1. Introduction

At the microscopic level, the flow of electric current in a metal corresponds to a collective motion of mobile conduction electrons within a background created by relatively static atomic nuclei and valence electrons [1]. The electron is a fundamental particle whose charge is equal to  $-e$ , where  $e$  is the elementary charge. The value of  $e$  in SI units is approximately  $1.602 \times 10^{-19}$  C [2]. An electric current of 1 ampere used in a typical electrical appliance corresponds to a flow rate of about  $6 \times 10^{18}$  electrons per second. Hence, the granularity of electric charge is not observed in everyday settings. However, a convincing proof of the quantization of electric charge was presented by Robert Millikan already a century ago in 1913 [3]. By performing the famous oil droplet experiment, he was able to measure changes in the motion of the droplets as they randomly acquired individual electrons or ions from the air that was ionized with x-rays. Partly for this work, Millikan was awarded the Nobel Prize in physics in 1923 [4].

In this thesis, we study metallic nanostructures where electric charge can be transferred in a *controlled fashion* between conductors one electron at a time. We also demonstrate the detection of individual electron tunneling events between a superconductor and a normal metal in real time, and measure small electric currents by counting the passage of individual electrons. Although such demonstrations are standard in semiconductor quantum dots with tunable barriers [5, 6], the use of electron counting techniques to study of hybrid superconductor–normal metal structures is new. Also, another recurring theme in the experiments is electronic cooling and heat transport in the presence of single-electron charging effects.

The physical platform on which we performed most of these experiments is the SINIS-type single-electron transistor (SET). This structure consists of superconducting (S) source and drain electrodes with a normal metallic

(N) island in between. The island is contacted to the electrodes via tunnel junctions (I). Due to a phenomenon known as the Coulomb blockade, electric transport through the transistor can be significantly altered by a fraction-of- $e$  change in the gate charge of the transistor [7, 8]. In the existing literature, hybrid structures consisting of superconducting and normal electrodes have been studied in various configurations [9, 10, 11], where they were employed as electronic coolers and probes of electronic temperature, for example. The new results and experimental techniques we present here are based on an interplay between the superconducting gap parameter  $\Delta$  and the charging energy  $E_c$ , which has not been studied thoroughly in hybrid structures in earlier works.

The overview part of this thesis is organized as follows: In Section 2, we give a general description of the physical phenomena observed in the experiments in terms of established theory. The experimental results concerning density of non-equilibrium quasiparticles in thin film aluminum are also presented in Section 2 along with the relevant theory of quasiparticle dynamics in the superconductor. Section 3 contains a description of the experimental methods used for the low-temperature transport measurements. We describe briefly the sample fabrication and refrigeration techniques that are well known in the field of mesoscopic physics. More emphasis is given to the discussion of the filtering and shielding solutions incorporated in the design of the sample stages, and analysis of the performance and back-action of the SET-based electron counting scheme used in many of the experiments.

The most important new experimental results are presented in Section 4 with supporting theory. Publications I, II, X and XI highlight different aspects of heat flow in the presence of charging effects. The heat transistor experiment reported in Pub. II was the first experimental demonstration of Coulombic control of refrigeration, and also the first demonstration of NIS thermometry in a device with strong charging effects. The experimental results were found to be in excellent agreement with a theoretical model based on the orthodox theory, which should motivate further studies of more complex designs. One such study was Pub. I, where we propose theoretically a cyclic electronic refrigerator based on a NIS-type single-electron box [12] subject to a radio frequency gate drive. The same structure with a much slower gate drive was the subject of Pubs. X and XI, where we analyzed theoretically and experimentally the statistics of dissipated heat instead of the time-averaged cooling power. This work

was based on an earlier proposal [13], where it was noted that such an analysis would constitute a first test of certain fluctuation relations of non-equilibrium thermodynamics [14, 15] in an electronic system.

The remaining Pubs. III–IX concern the transport of electric charge in hybrid structures. In Pub. III, we demonstrated that a hybrid SET can be used as an electron turnstile that produces the current  $I = ef$ , where  $f$  is the frequency of an external drive signal. A major motivation for the rest of the studies was to improve the accuracy of the hybrid turnstile from the about 1% level of the original demonstration towards the  $10^{-7}$  level required for a metrological current source [16]. The first step in this direction was taken in Pub. IV, where coupling of microwave radiation from higher temperature parts of the cryostat was identified as the source of subgap leakage observed in NIS junctions. Further advances in microwave shielding brought about by improved sample and sample stage design are reported in Pubs. V, IX, and VII. The  $2e$  Andreev tunneling process, another source of subgap leakage in NIS and SINIS structures, was studied quantitatively in Pub. VIII, and could also be observed in the data of Pub. IX. Furthermore, the sample of Pub. IX was also suitable for probing the density of non-equilibrium quasiparticles in the superconducting leads. For a sample fabricated with a direct NS contact as a quasiparticle trap, we were able to infer a record-low upper bound on the density of nonequilibrium quasiparticles  $n_{\text{qp}} < 0.033 \mu\text{m}^{-3}$ . Similarly, we obtained an upper bound of  $\gamma < 1.6 \times 10^{-7}$  for the Dynes parameter [17, 18] of the thin film aluminum leads, which is also the lowest number reported to date. In Pubs. VI and VII, the charge escape rate from a mesoscopic trapping node through a SINIS SET was studied. In the setup with the best microwave shielding, we were able to observe charge trapping times of about 10 h, which is an evidence for the applicability of SINIS structures for certain applications of electronic metrology.

Finally, Section 5 contains a description of two efficient numerical methods that we employed in the analysis of electric transport in Coulomb-blockaded NIS structures.



## 2. Theoretical basis

### 2.1 Quasiparticle transport in tunnel junctions

#### 2.1.1 Orthodox theory of single-electron tunneling

The studies of single-electron transport presented in this thesis are enabled by electrical measurements of tunnel junctions, such as the one depicted in Fig. 2.1. A tunnel junction [9, 19] is an arrangement where two conductive electrodes are separated by a thin insulating layer. Charge carriers in the electrodes can penetrate the potential barrier of the insulator via quantum mechanical tunneling, thus allowing for an electric current to pass through while inducing only a weak perturbation to the electronic properties of the electrodes.

The theoretical basis for modeling of electron transport in the sequential tunneling regime is thoroughly presented in two classic review articles, one by Averin and Likharev [20], and the other by Ingold and Nazarov [21]. Owing to the key role orthodox theory has in the interpretation of the experimental results presented here, the essential steps of the calculation are reproduced below. Furthermore, many of the experiments highlight conditions where the system's behavior departs in some way from the basic model. These scenarios and their theoretical modeling are discussed in later sections.

The starting point of the orthodox theory is a second quantization description of the tunnel junction and the electrodes with the Hamiltonian

$$H = H_L + H_R + H_T, \quad (2.1)$$

where  $H_L$  and  $H_R$  correspond to the two electrodes referred to as the left (L) and right (R) lead, respectively, and  $H_T$  is the tunneling Hamiltonian

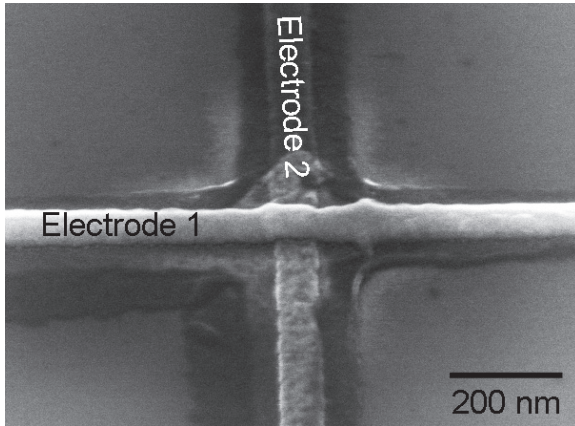


**Figure 2.1.** Scanning electron micrograph taken at a slightly oblique angle showing the crossing of two metallic electrodes on an oxidized silicon substrate. Due to an insulating oxide barrier covering the bottom (vertical) electrode, a tunnel junction is formed between the electrodes at the intersection.

that accounts for the tunnel coupling between the leads. A Hamiltonian of this form was originally introduced by Cohen *et al.* [22]. Neglecting electron spin for now, the lead Hamiltonians can be written generally as

$$H_L = \sum_{\mathbf{k}} \epsilon_{\mathbf{k}}^L a_{\mathbf{k}}^\dagger a_{\mathbf{k}} \quad H_R = \sum_{\mathbf{k}'} \epsilon_{\mathbf{k}'}^R b_{\mathbf{k}'}^\dagger b_{\mathbf{k}'}, \quad (2.2)$$

where  $a_{\mathbf{k}}$  and  $b_{\mathbf{k}'}$  ( $a_{\mathbf{k}}^\dagger$  and  $b_{\mathbf{k}'}^\dagger$ ) are annihilation (creation) operators for quasiparticle states with wave vectors  $\mathbf{k}$  and  $\mathbf{k}'$  in the left and right leads, respectively, and  $\epsilon_{\mathbf{k}}^L$  and  $\epsilon_{\mathbf{k}'}^R$  are the excitation energies. The tunneling Hamiltonian is given by

$$H_T = \sum_{\mathbf{k}, \mathbf{k}'} \left( T_{\mathbf{k}\mathbf{k}'} a_{\mathbf{k}}^\dagger b_{\mathbf{k}'} + \text{h. c.} \right), \quad (2.3)$$

where  $T_{\mathbf{k}\mathbf{k}'}$  is the tunnel matrix element between states  $\mathbf{k}$  and  $\mathbf{k}'$ , and the conjugate term denoted by h. c. describes the coupling in the opposite direction. The origin of tunnel coupling is a finite overlap between wave functions in the different leads. Evaluation of the tunnel matrix elements from first principles is deferred until the next section, as the calculation has many subtleties and is not crucial to the derivation of orthodox theory.

In Sec. 2.2.1, the above formulation will be augmented with a description of the coupling of finite-frequency electromagnetic modes to the tunneling process. The simpler case of a dc voltage bias  $V$  applied over the junction can be treated with an energy conservation argument, as will be shown shortly. External electric fields can also couple directly into the electrodes, although voltage drops in the leads are usually neglected when

dealing with opaque small-area junctions. Nevertheless, with suitable device parameters, it is possible to observe Joule heating [23] or absorption of microwave photons in the thin-film electrodes [24]. Part of the energy absorbed in the film in the form of quasiparticles excitations could then diffuse into the junction site, and affect the observed tunneling current. Heat flows in thin-film structures will be discussed in detail in Sec. 2.4.

Due to the continuum of electronic states available for tunneling, charge transfer from, say, lead L to lead R can be described in the first order by a Markovian transition rate  $\Gamma_{L \rightarrow R}$ . This rate can be evaluated by treating  $H_T$  as a weak perturbation and applying Fermi's Golden rule. The result is the transition rate between microscopic states  $s_i$  and  $s_f$  of the whole system, given by

$$\Gamma_{s_i s_f} = \frac{2\pi}{\hbar} |\langle s_f | H_T | s_i \rangle|^2 \delta(E_{s_i} - E_{s_f}), \quad (2.4)$$

which should be integrated over the possible initial and final states. Recalling the form of  $H_T$  in Eq. (2.3) and the orthogonality of the basis states, a nonzero amplitude for left-to-right tunneling is obtained only in the case  $|s_f\rangle = b_{\mathbf{k}'}^\dagger a_{\mathbf{k}} |s_i\rangle$ . Thus, we obtain

$$\Gamma_{L \rightarrow R}^\sigma = \frac{2\pi}{\hbar} \sum_{\mathbf{k}, \mathbf{k}'} |T_{\mathbf{k}\mathbf{k}'}|^2 \left\langle a_{\mathbf{k}}^\dagger a_{\mathbf{k}} b_{\mathbf{k}'} b_{\mathbf{k}'}^\dagger \right\rangle_0 \delta(\epsilon_{\mathbf{k}} - \epsilon_{\mathbf{k}'} + eV), \quad (2.5)$$

where the superscript  $\sigma$  indicates that the result is for one spin species only,  $\langle \dots \rangle_0$  denotes an average over the statistical ensemble of initial states, and the effect of voltage bias has been inserted by hand to the energy conservation condition. In Fermionic statistics,  $\left\langle a_{\mathbf{k}}^\dagger a_{\mathbf{k}} b_{\mathbf{k}'} b_{\mathbf{k}'}^\dagger \right\rangle_0 = P_L(\mathbf{k}) [1 - P_R(\mathbf{k}')]$ , where we have denoted by  $P_L(\mathbf{k})$  and  $P_R(\mathbf{k}')$  the occupation probability of states  $\mathbf{k}$  and  $\mathbf{k}'$  in the left and right leads, respectively. If, furthermore, the leads are in thermal equilibrium, the occupation probabilities follow the Fermi-Dirac distribution: In the left lead, for example,

$$P_L(\mathbf{k}) = \frac{1}{1 + \exp[(\epsilon_{\mathbf{k}}^L - \epsilon_F^L)/k_B T_L]}, \quad (2.6)$$

where  $T_L$  is the temperature and  $\epsilon_F^L$  is the Fermi energy of the lead. The fact that both probabilities  $P_L$  and  $P_R$  appear as independent factors is a manifestation of the perturbative nature of the tunneling Hamiltonian approach, which is the appropriate picture for opaque junctions. The opposite limit of a transmission approaching unity can be addressed by a Landauer-Büttiker-type scattering approach, where the reservoirs act as perfect sinks of carriers [25].

The remaining summation in Eq. (2.5) over wave vectors weighted with the squared matrix element is often deferred by introducing a tunneling resistance  $R_T$  that incorporates information about the average matrix element and density of states near the Fermi level. The end result is an integral

$$\begin{aligned} \Gamma_{L \rightarrow R} &= \frac{1}{e^2 R_T} \int_{-\infty}^{\infty} dE_L \int_{-\infty}^{\infty} dE_R f_L(E_L) n_L(E_L) \\ &\quad [1 - f_R(E_R)] n_R(E_R) \delta(E_L - E_R + eV) \\ &= \frac{1}{e^2 R_T} \int_{-\infty}^{\infty} dE f_L(E) n_L(E) [1 - f_R(E + eV)] n_R(E + eV), \end{aligned} \quad (2.7)$$

where  $n_L(E)$  [ $n_R(E)$ ] is the density of states (DOS) in lead L (R) relative to the constant density of states absorbed in the prefactor  $R_T$ , and the occupation probability assumes the form

$$f_{L,R}(E) = [1 + \exp(E/k_B T_{L,R})]^{-1} \quad (2.8)$$

as the energies are measured relative to the Fermi level. The case  $n_L(E) = n_R(E) = 1$  corresponds to a junction between two normal metallic electrodes. Various non-constant densities have been used to describe, e. g., quasiparticle excitations in a superconductor, which is the central theme of this thesis and discussed in more detail in Secs. (2.3.1) and (2.3.2). In addition to pure superconductors, tunneling spectroscopy is widely used in the literature to study the proximity effects occurring at a clean interface between a superconductor and a normal or ferromagnetic metal [26, 27, 28]. Equation (2.7) is convenient for modeling of experimental results, as the parameter  $R_T$  is equal to the asymptotic resistance of the junction, which can be determined in many cases even by a handheld multimeter. However, from a theoretical point of view the result is unsatisfying, as the dependence of  $R_T$  on the physical dimensions of the junction is not elaborated. These issues will be addressed in the next section.

### 2.1.2 Evaluation of tunneling matrix elements

In order to demonstrate the influence of the barrier properties on the tunneling transport, we will calculate explicitly the tunneling matrix elements for a rectangular barrier between two normal conductors in the ballistic plane-wave case, and evaluate the double sum over wave vectors in Eq. (2.5). Figure 2.2 illustrates the assumed geometry of the conductors and the barrier.

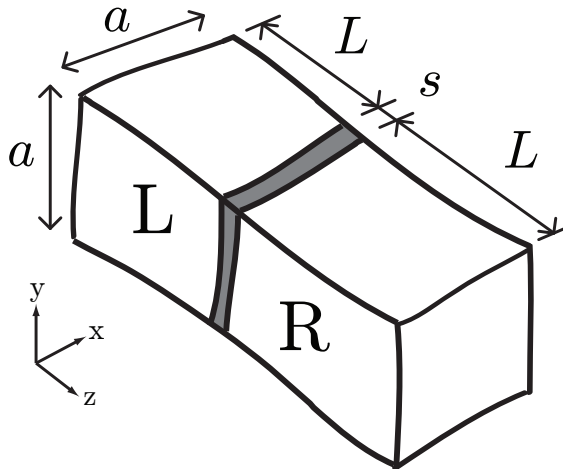


**Figure 2.2.** Two rectangular conductors connected by a tunnel barrier in between.

Before presenting the calculation, let us consider the range of applicability of the ballistic picture. The elastic mean free path  $l_{\text{el}}$  of electrons in the typical conductors of this work – evaporated aluminum and copper thin-films – at low temperatures is of the order of 10 nm [29, 30]. On the other hand, taking 100 nm as the typical lateral dimension of the tunnel junction and the adjacent electrodes, we see that the electronic wave functions at the junction site are not simple plane waves, but instead show interference patterns resulting from scattering [31]. The results of the ballistic calculation for one-electron transport are not sensitive to the interference, and remain valid in the diffusive case as well [31]. Later in this thesis, we will present results concerning the coherent tunneling of two electrons across a tunnel junction between a normal metal and a superconductor. Also in this two-electron case, we will use a theory based on the ballistic picture to explain the experimental results. However, in order to obtain a quantitative agreement, we will introduce  $A_{\text{ch}}$ , the area per quantum channel, as a semi-phenomenological fitting parameter that will also account for the diffusive enhancement of the two-electron conductivity that is not explicitly included in the model. The theory for two-electron tunneling in an NIS junction is presented in Sec. 2.3.2.

For performing the overlap integrals, explicit wave functions are needed for the quasiparticle states in the leads. We write down the stationary single-particle Schrödinger equation

$$-\frac{\hbar^2}{2\mu}\nabla^2\psi(\mathbf{r}) + U(z)\psi(\mathbf{r}) = E\psi(\mathbf{r}), \quad (2.9)$$

where  $\mu$  is the effective mass, and the tunnel barrier is modeled by a rectangular potential barrier  $U(z) = U_0$  for  $0 < z < s$  and  $U(z) = 0$  otherwise. In the classic treatment of tunnel current by Simmons [32], the rectangular shape of the potential barrier is modified to account for biasing and the so-called image force experienced by a charged particle in the vicinity of conductors, but these effects are ignored here for simplicity. On the other hand, Simmons's result is a barrier penetration calculation for single-particle wave functions, and as such is not a suitable starting point for theoretical modeling of, e. g., coherent tunneling processes involving multiple electrons.

Due to the assumed homogeneity of the barrier in the  $xy$  plane, the 3D wave function factorizes into  $\psi(\mathbf{r}) = \varphi(x, y)\phi(z)$ , where the transverse part  $\varphi(x, y)$  is the solution of a particle-in-a-box problem and  $\phi(z)$  corresponds to 1D barrier penetration. The transverse solutions read

$$\varphi_{nm}(x, y) = \frac{2}{a} \sin\left(\frac{n\pi}{a}x\right) \sin\left(\frac{m\pi}{a}y\right), \quad E_{xy} = \frac{\pi^2 \hbar^2}{2\mu a^2} (n^2 + m^2), \quad (2.10)$$

where  $n, m \in \mathbb{Z}_+$  and the conductor boundaries are taken to lie at  $x, y = 0$  and  $x, y = a$ . The longitudinal component of the wave function satisfies

$$-\frac{\hbar^2}{2\mu} \partial_z^2 \phi(z) + V(z)\phi(z) = E_z \phi(z). \quad (2.11)$$

We look for solutions that are free-electron like in one of the leads (say, L) and decay exponentially inside the barrier. Requiring a node of the wave function at  $z = -L$  and first-order continuity at  $z = 0$ , we obtain a family of solutions

$$\psi_q^L(z) = \begin{cases} -\sqrt{\frac{2}{L}} \sin(k_z z - \theta) & \text{for } z \leq 0 \\ \sqrt{\frac{2}{L}} \sin(\theta) e^{-\kappa z} & \text{for } z > 0 \end{cases}, \quad (2.12)$$

$$k_z = \frac{q\pi - \theta}{L}, \quad \kappa = \sqrt{\frac{2\mu U_0}{\hbar^2} - k_z^2}, \quad \tan \theta = \frac{k_z}{\kappa}, \quad E_z = \frac{\hbar^2 k_z^2}{2\mu},$$

where  $q \in \mathbb{Z}_+$ . Long  $L$  limit was assumed above for state normalization. The above choice of exponentially decaying wave functions in the forbidden lead (i. e., lead R for a state occupying mostly lead L, and vice versa) is the same as originally employed by Bardeen [33]. Prada and Sols [34] discuss different theoretical approaches to the problem of electron tunneling through NIS structures, and also use the "Bardeen model" as their starting point with a more careful analysis of its range of validity than is presented here.

Let us now return to the double sum over wave vectors  $\mathbf{k}$  in Eq. (2.5). Following Bardeen's calculation, matrix elements between the standing

wave states defined above can be evaluated as

$$T_{\mathbf{k}\mathbf{k}'} = U_0 \int_{z>a} d\mathbf{r} \psi_{\mathbf{k}}^L(\mathbf{r})^* \psi_{\mathbf{k}'}^R(\mathbf{r}) \quad (2.13)$$

in the limit of vanishing energy difference  $E_{\mathbf{k}} - E_{\mathbf{k}'}$ . We note that the tunneling matrix element vanishes between states with different transverse momenta. For the sums in  $z$  direction with a continuum of momentum states, we perform the standard substitution  $\sum_{k_z} \rightarrow \frac{L}{\pi} \int dk_z$  and change the integration variable to  $E = E_{xy} + E_z$ . We arrive at

$$\Gamma_{L \rightarrow R}^{\sigma} = \frac{L^2 \mu}{\pi \hbar^3} \int_0^{\infty} dE P_L(E) [1 - P_R(E')] \sum_{n,m \geq 1} \frac{|T_{\mathbf{k}\mathbf{k}'}|^2}{\sqrt{E_z E'_z}}, \quad (2.14)$$

where  $E' = E + eV$ . Finally, we evaluate the matrix elements by direct integration. The occupation factors imply that only electrons within an energy range of few times  $\max\{eV, k_B T\}$  from  $E_F$  can participate in the tunneling processes. The relevant energy scale over which the matrix elements change is given by the barrier height measured from the Fermi level, i. e.,  $\Phi_0 = U_0 - E_F$ . In the limit of small bias voltages and temperatures  $eV, k_B T \ll \Phi_0$ , we can assume  $E = E' \approx E_F$  when dealing with the matrix elements. The tunneling rate can now be written as

$$\Gamma_{L \rightarrow R} = \frac{1}{2\pi \hbar} \sum_{\sigma} \sum_{n,m \geq 1} T \left( \frac{E_F}{U_0} - \frac{\pi^2 \hbar^2}{2\mu a^2 U_0} (n^2 + m^2) \right) \int_0^{\infty} dE P_L(E) [1 - P_R(E')], \quad (2.15)$$

$$T(\epsilon_z) = 16 \epsilon_z (1 - \epsilon_z) e^{-2s \sqrt{\frac{2\mu U_0}{\hbar^2} (1 - \epsilon_z)}}, \quad (2.16)$$

where the summation over the spin index  $\sigma$  in Eq. (2.15) amounts to a multiplication by factor 2. Physical interpretation can be given to the different factors that constitute Eq. (2.15): The prefactor can be written as  $1/(e^2 R_K)$ , where the von Klitzing constant  $R_K$  is the electrical resistance of one perfectly transmitting channel. Terms in the  $n, m$ -summation show which longitudinal channels contribute to the tunnel conductance. Factor  $T(\epsilon_z)$  is equal to the penetration probability of an electron that impinges orthogonally on the barrier with longitudinal kinetic energy  $E_z = \epsilon_z U_0$ . Equation (2.16) for  $T(\epsilon_z)$  has been published in, e. g., Ref. [34].

To describe the typical opaque  $\text{AlO}_x$  barrier of this work, we take  $\mu = 0.5 m_e$ ,  $s = 1.1$  nm and  $U_0 = 2$  eV based on Gloos *et al.* [35]. Substituting these values into Eq. 2.16, the transmission probability  $T(\epsilon_z)$  evaluates to  $4 \times 10^{-5}$ . Furthermore, we note that  $T(\epsilon_z)$  has an exponential dependence on the longitudinal energy in the relevant energy range in the vicinity of the Fermi level. Hence, majority of the tunneling electrons

have small transverse momentum, i. e., the incident angle of tunneling electrons is small. This is known as the focusing effect [36, 37]. To obtain an analytical formula for the effective channel number, we expand  $T(\epsilon)$  as

$$T(\epsilon_F + \delta) = T(\epsilon_F) e^{s \sqrt{\frac{2\mu U_0}{\hbar^2(1-\epsilon_F)}} \delta}, \quad (2.17)$$

where  $\epsilon_F = E_F/U_0$ . We arrive at the channel number estimate

$$\mathcal{N} = \frac{\sum_{n,m \geq 1} T(E_z/U_0)}{T(E_F/U_0)} \approx \sqrt{\frac{\mu \Phi_0}{2\pi^2 s^2 \hbar^2}} a^2. \quad (2.18)$$

We note that the final answer depends only on  $\Phi_0$ , and not on the absolute barrier height  $U_0$  or the Fermi energy  $E_F$ . The result can be also expressed in terms of area per channel, which evaluates to  $1.4 \text{ nm}^2$  in the prototypical  $\text{AlO}_x$  case based on the barrier parameters stated above. However, one should be aware of the considerable scatter in the barrier parameters reported in the literature. For Pub. VIII, we used  $d = 2 \text{ nm}$  based on high-resolution transmission electron microscopy (HRTEM) measurements reported in Ref. [38], leading to  $a^2/\mathcal{N} = 2.5 \text{ nm}^2$  instead.

## 2.2 Circuit considerations

### 2.2.1 $P(E)$ theory

A thorough treatment of the electromagnetic environment and its coupling to charge tunneling has been presented in great detail by Ingold and Nazarov [21]. The resulting framework is known as the  $P(E)$  theory, of which we will reproduce only the most essential results here.

In the network theory picture on which the theory is based, the junction is viewed simply as a capacitance  $C_j$ . Ideally, this models the parallel plate capacitor formed by the junction electrodes and the insulating dielectric. The possibility of charge transport between the capacitor plates via tunneling is accounted for in a perturbative manner. For a quantum description of such a circuit element, one introduces the operator  $Q$  for the charge on the junction electrodes, and the phase operator  $\varphi$  conjugate to it, defined as

$$\varphi(t) = \frac{e}{\hbar} \int_{-\infty}^t dt' U(t'), \quad (2.19)$$

where  $U = Q/C_j$  is the operator for voltage drop across the junction. The tunneling Hamiltonian of Eq. (2.3) is modified to read

$$H_T = \sum_{\mathbf{k}, \mathbf{k}'} \left( T_{\mathbf{k}\mathbf{k}'} a_{\mathbf{k}}^\dagger b_{\mathbf{k}'} e^{-i\varphi} + \text{h. c.} \right). \quad (2.20)$$

The operator  $e^{-i\varphi}$  appearing in the above equation has the effect of changing the junction charge by  $e$ , as  $Qe^{-i\varphi} = e^{-i\varphi}(Q - e)$ . After a Golden Rule calculation similar to the one presented before, the tunneling rate formula corresponding to Eq. (2.7) can be shown to assume the form

$$\Gamma_{L \rightarrow R} = \frac{1}{e^2 R_T} \int_{-\infty}^{\infty} d\lambda \int_{-\infty}^{\infty} dE f_L(E) n_L(E) [1 - f_R(E + \lambda)] n_R(E + \lambda) P(eV - \lambda), \quad (2.21)$$

where  $P(E)$  can be interpreted as the probability density to emit energy  $E$  into the environmental modes in the tunneling process. Negative values of  $E$  correspond to energy absorption. The above parametrization of the double integral was chosen to show explicitly that the  $P(E)$  function acts as a convolution kernel when evaluating  $\Gamma(eV)$ . In the most general case, the function  $P(E)$  can be calculated as the Fourier transform

$$P(E) = \frac{1}{2\pi\hbar} \int_{-\infty}^{\infty} dt e^{\frac{i}{\hbar}Et} \left\langle e^{i\tilde{\varphi}(t)} e^{-i\tilde{\varphi}(0)} \right\rangle_R, \quad (2.22)$$

where  $\tilde{\varphi}(t) = \varphi(t) - Vt$  is the fluctuating part of the phase over the junction, and the ensemble average  $\langle \dots \rangle_R$  is taken over realizations of the noisy environment. Sometimes, the word ‘reservoir’ is used to emphasize the fact that the environment is composed of a large number of degrees of freedom, and can absorb or emit energy to the studied system without a noticeable change in the state of the reservoir.

It can be shown that  $\int_{-\infty}^{\infty} dE P(E) = 1$  always, enabling its interpretation as a probability density. It is also possible to write the  $P(E)$  in a form where the probability to emit or absorb  $k$  photons at specific environmental modes appears explicitly (see, e. g., Ch. 20.2.2 of Ref. [39]). The phenomenon where a tunneling event is associated with absorption of a photon from the environment is generally referred to as photon-assisted tunneling (PAT). The  $P(E)$  function for an equilibrium environment at temperature  $T$  satisfies a detailed balance relation

$$P(-E) = e^{-E/k_B T} P(E). \quad (2.23)$$

For completeness, we note that calculations going beyond the network theory approximation have been presented in, e. g., Ref. [40] and the appendices of Ref. [21], where propagation of electrons and electric fields in the electrodes is explicitly included in the model.

Above, the problem of describing the environmental influence was reduced to the evaluation of the phase-correlation function appearing in

Eq. (2.22). The standard continuation here is to invoke the equality

$$\left\langle e^{i\tilde{\varphi}(t)} e^{-i\tilde{\varphi}(0)} \right\rangle_R = e^{J(t)}, \quad (2.24)$$

where the correlation function  $J(t)$  is defined as

$$J(t) = \langle [\tilde{\varphi}(t) - \tilde{\varphi}(0)] \tilde{\varphi}(0) \rangle_R. \quad (2.25)$$

Equation (2.24) can be proven using Wick's theorem [21] provided that the ensemble average is taken over an equilibrium distribution of the reservoir.

*Weak noise limit* — In the context of this thesis, the  $P(E)$  formalism is applied in cases where environmental fluctuations are coupled weakly to the junction. For physical insight, we will expand Eq. (2.24) to first order in  $J(t)$  and substitute back to Eq. (2.22) to obtain

$$P(E) = [1 - \langle \tilde{\varphi}(0)^2 \rangle_R] \delta(E) + \frac{1}{2\pi\hbar} \int_{-\infty}^{\infty} dt e^{\frac{i}{\hbar}Et} \langle \tilde{\varphi}(t) \tilde{\varphi}(0) \rangle_R, \quad (2.26)$$

assuming the correlator  $\langle \tilde{\varphi}(0)^2 \rangle_R$  is finite. The same expression can be obtained by assuming  $\tilde{\varphi}(t) \ll 1$  and expanding Eq. (2.24) to second order in  $\tilde{\varphi}$ . Integration over  $E$  shows that the result is properly normalized. The form is thus appropriate for description of rare interactions caused by weak noise. We can write the result for  $E \neq 0$  in terms of the spectral density of phase or voltage fluctuations as

$$P(E) = \frac{1}{2\pi\hbar} S_{\tilde{\varphi}\tilde{\varphi}}[E/\hbar] = \frac{\pi}{R_K E^2} S_V(E/h), \quad (2.27)$$

where we have used the notation of Clerk *et al.* [41] for the phase noise, and Martinis *et al.* [42] for the voltage noise. The relationship between phase and voltage noise follows from the definition of  $\tilde{\varphi}$  and the Wiener-Khinchin theorem, which relates the spectral density to Fourier components. The expression for  $P(E)$  in terms of  $S_V(f)$  has been presented in, e. g., Ref. [42]. We identify the possibility to use the tunneling current as a spectrometer of the environmental noise, provided that the shape of the  $\Gamma(V)$  [or  $I(V)$ ] dependence is such that the  $P(E)$  can be deconvoluted from the measurement results. In Ref. [43] by Basset *et al.*, fluctuation spectroscopy was demonstrated in the Cooper pair and quasiparticle branches of the  $I(V)$  characteristic of Josephson junction.

*Noise from an electrical impedance* — Another essential result for the theoretical basis of this thesis is an expression for the phase correlation function  $J(t)$  of equilibrium noise originating from the electrical circuit

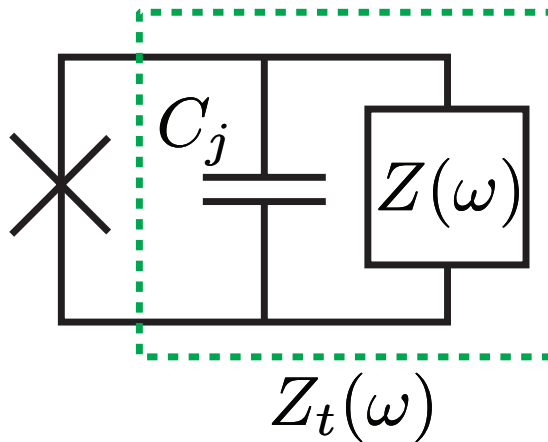


**Figure 2.3.** The impedance  $Z_t(\omega)$  determining the tunneling charge dynamics is that of a parallel connection of junction capacitance  $C_j$  and the impedance  $Z(\omega)$  of the embedding circuit as seen from the junction electrodes.

into which the junction is embedded. The result depends only on the total impedance  $Z_t(\omega)$ , defined as

$$Z_t(\omega) = \frac{1}{i\omega C_j + Z(\omega)^{-1}}, \quad (2.28)$$

where  $Z(\omega)$  is the impedance of the surrounding electrical circuit as seen from the junction, as illustrated in Fig. 2.3.  $Z_t(\omega)$  is the impedance that describes the relaxation of charge across the junction created by, e. g., an instantaneous tunneling of an electron across the barrier. For the charge relaxation process, the junction appears as a purely capacitive element. However, it should be noted that for realistic sample geometries, the effective shunt capacitance appearing in  $Z_t(\omega)$  includes in addition to  $C_j$  ( $\sim 1$  fF) some fraction of the much bigger lead capacitance (up to 10 pF in Pub. IV).

In a complete quantum treatment, the Hamiltonian should include a term  $H_{\text{env}}$  describing the internal dynamics of the electrical environment and the coupling to the junction coordinates  $Q$  and  $\varphi$ . The Caldeira–Leggett Hamiltonian [44] allows an arbitrary environmental impedance  $Z(\omega)$  to be modeled by a family of harmonic oscillators. However, the relevant phase correlator can be evaluated by an application of the Fluctuation-Dissipation Theorem (FDT) [45] without constructing  $H_{\text{env}}$  explicitly. The result is [21]

$$J(t) = 2 \int_{-\infty}^{\infty} \frac{d\omega}{\omega} \frac{\text{Re}[Z_t(\omega)]}{R_K} \frac{e^{-i\omega t} - 1}{1 - e^{-\beta\hbar\omega}}. \quad (2.29)$$

Using Eqs. (2.24) and (2.29), the  $P(E)$  function for an arbitrary impedance  $Z_t(\omega)$  can be evaluated by performing two nested integrals. In general, the integrals cannot be performed in closed form, and one must resort to numerical techniques. In the special case that  $\lim_{\omega \rightarrow 0} \frac{\text{Re}[Z_t(\omega)]}{\omega}$  is finite – in practice meaning that the junction is inductively shunted – a linear expansion to first order in  $\frac{\text{Re}[Z_t(\omega)]}{R_K}$  can be performed, yielding

$$P(E) = \frac{2}{E} \frac{\text{Re}[Z_t(E/\hbar)]}{R_K} \frac{1}{1 - e^{-\beta E}} \quad (2.30)$$

for  $E \neq 0$ , in agreement with Ref. [42]. In Ref. [46], the zero-temperature limit of the above formula is shown to hold for a general  $Z_t(\omega)$  and sufficiently large  $E$ . We stress that zero-temperature (quantum) fluctuations of the environment cannot emit energy, and hence cannot enable tunneling electrons to overcome energy barriers created by charging effects or the superconducting energy gap.

In the supplemental material of Pub. IV, we treat algebraically the experimentally relevant case of a finite-temperature dissipative element, which we model as parallel  $RC$  circuit. The exact result for  $J(t)$  reads

$$J(t) = \frac{\rho}{2} \left[ \cot(B) \left( 1 - e^{|\tau|} \right) - \frac{|\tau|}{B} - 2 \sum_{n=1}^{\infty} \frac{1 - e^{-n\pi|\tau|/B}}{n\pi [1 - (n\pi/B)^2]} - i \text{sign}(\tau)(1 - e^{-|\tau|}) \right], \quad (2.31)$$

where  $\rho = 2\pi R/R_K$ ,  $\tau = t/(RC)$ , and  $B = \hbar/(2k_B T_{\text{env}} RC)$ . The above series representation can be employed in numerical calculations. Furthermore, in the limit  $|E| \ll k_B T_{\text{env}}, \hbar/(RC)$  and  $\rho \ll 1$ , one obtains a particularly simple analytic result

$$P(E) = \frac{1}{\pi} \frac{\rho k_B T_{\text{env}}}{(\rho k_B T_{\text{env}})^2 + E^2}. \quad (2.32)$$

One should note that the above approximation does not capture the correct asymptotic behavior for large  $E$ . From Eq. (2.30), one expects an exponential  $e^{-|E|/k_B T}$  cutoff for large negative  $E$ , and an algebraic  $1/E^3$  decay for positive  $E$ . The Lorentzian form of Eq. (2.32) is nevertheless useful for describing sub-gap  $I(V)$  features of an NIS junction irradiated by the Nyquist noise of a weakly coupled hot ( $T_{\text{env}} \gtrsim \Delta/k_B$ ) resistor. This case was studied in detail in Pub. IV.

Furthermore, we demonstrated that engineering a capacitive shunt close to the junction increases the effective  $C$  in the environmental impedance, reducing the coupling of harmful high-energy photons to the junction. Note that the capacitance  $C$  does not appear in Eq. (2.32), but

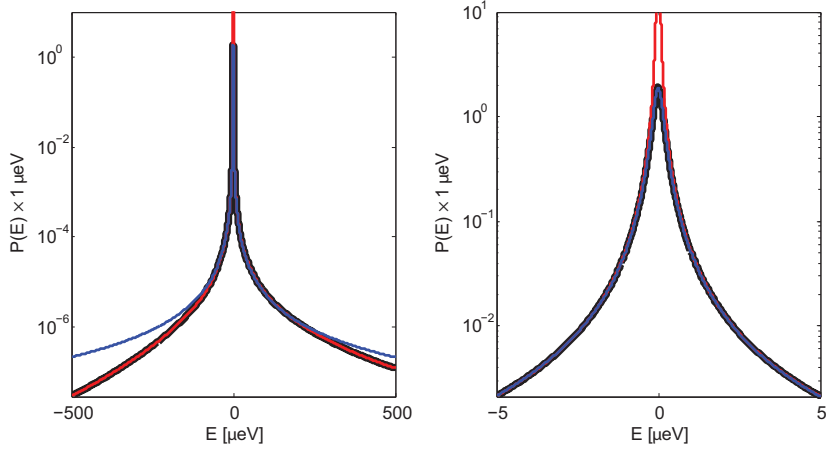


**Figure 2.4.** Exact and approximative  $P(E)$  functions for an  $RC$  environment with  $R = 2 \Omega$  and  $C = 1 \text{ pF}$  at temperature  $T_{\text{env}} = 4 \text{ K}$ . The right panel is a close-up of the behavior close to zero energy. The thick black curve is an exact result calculated by evaluating  $J(t)$  from Eq. (2.31) numerically with high resolution, and then taking the Fourier transform. Red and blue curves are the approximate results from Eqs. (2.30) and (2.32), respectively. The result of Eq. (2.30) tends to infinity at  $E = 0$ .

increasing the environmental  $RC$  product narrows the range of energies where it is valid. Figure 2.4 illustrates the  $P(E)$  functions calculated with the approximative formulas of Eqs. (2.30) and (2.32), and the exact numerical result based on Eq. (2.31) for a typical  $RC$  environment of Pub. IV. The sub-gap current in the experiments in the low-temperature limit is determined by the values of the  $P(E)$  function in the energy range  $-\Delta < E < 0$ . Detailed interpretation of experimental  $I(V)$  and  $\Gamma(\epsilon V)$  curves in the context of PAT is discussed in Sec. 4.2.

*Composite fluctuations* – The fluctuations coupling to a tunnel junction in a real low-temperature experiment can originate from multiple independent sources. The possibilities include equilibrium noise from circuit elements at different temperature stages of the cryostat, and non-equilibrium noise from actively driven components. Let us consider the case when the total phase fluctuation is a sum of independent components, i. e.,  $\tilde{\varphi} = \tilde{\varphi}_1 + \dots + \tilde{\varphi}_n$  with  $[\tilde{\varphi}_i, \tilde{\varphi}_j] = 0$ . It follows immediately from Eq. (2.22) that the total  $P(E)$  function is then the convolution

$$P = P_1 * \dots * P_n, \quad (2.33)$$

where  $P_i$  is the  $P(E)$  function evaluated for fluctuator  $\tilde{\varphi}_i$  alone.

In the case of a remote noise source, for example, it can be useful to consider separately the source fluctuations and the transfer function from

the source to the junction under study. A frequency-independent scaling of voltage (or, equivalently, phase) fluctuations by a factor  $\xi$  has the same effect as replacing the impedance  $Z_t(\omega)$  by  $\xi^2 Z_t(\omega)$ . A practical way to realize such voltage division is by a linear chain of tunnel junctions. This idea has been employed in earlier works for reducing the susceptibility of CBT temperature sensors to environmental fluctuations [47]. Consider a chain of  $N$  identical tunnel junctions with capacitance  $C$  in an environment described by resistance  $R$ . Direct evaluation of the impedance seen by one tunnel junction gives

$$Z_t(\omega) = \frac{R}{(\omega RC)^2 + N^2}. \quad (2.34)$$

We can arrive at the same expression from the voltage division viewpoint: the chain as a whole is equivalent to a capacitance  $C/N$ , but each junction feels only a fraction  $\xi = 1/N$  of the fluctuations over the chain. Hence,  $Z_t(\omega) = N^{-2} \frac{R}{(\omega RC/N)^2 + 1}$ , in agreement with Eq. (2.34) above. In the limit  $N \rightarrow \infty$ , the behavior approaches that of an ideal voltage bias. In the range of validity of Eq. (2.30), a similar relation can be written for a frequency-dependent attenuation  $\xi(\omega)$ . In the case of an electrical circuit containing sub-circuits at different temperatures, the  $P(E)$  functions can be evaluated independently for the sub-circuits taking into account the transfer function realized by the rest of the circuit. This "composite" scheme was used for modeling the electrical environment of Pub. VII, which consisted of an on-chip resistor and unwanted microwave radiation leaking from higher-temperature parts of the cryostat into the sample stage.

### 2.2.2 Charging energy

The electrostatic energy stored in a capacitor is  $Q^2/(2C)$ , where  $Q$  is the charge transferred between the capacitor plates and  $C$  is the capacitance. Substituting elementary charge  $e$  for  $Q$ , we obtain an energy scale for single-electron charging effects that we will refer to as charging energy<sup>1</sup>,

$$E_c = \frac{e^2}{2C}. \quad (2.35)$$

The condition where electronic transport is suppressed due to an energy barrier created by charging effects is called Coulomb blockade. According to a history of single-electronics presented in Ref. [50], charging effects in

<sup>1</sup>Note that  $E_c$  is sometimes defined as  $2e^2/C$  in works involving Cooper pair tunneling [48], and also  $e^2/C$  is used by some authors [49].

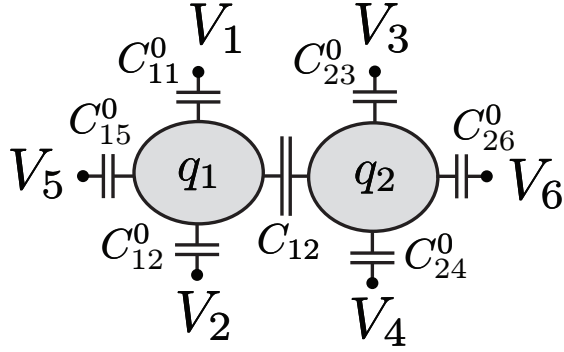


**Figure 2.5.** Capacitance network with  $N = 2$  islands and  $M = 6$  voltage terminals corresponding to two capacitively coupled SETs.

electrical transport were first observed as a zero-bias dip in conductance of granular metal films [51, 52, 53, 54]. However, a lithographical way of defining the geometrical arrangement of conductors and tunnel junctions is needed for realizing devices with more complex logical functions. The fabrication process of tunnel junctions utilized in this thesis is based on that developed by Fulton and Dolan [55, 7], and is explained in detail in Sec. 3.1.

For an illustrative reasoning about the energy scales relevant for single-electron devices, we take  $C = 1$  fF for a typical capacitance in lithographically realized structures. The resulting  $E_c$  is  $1.3 \times 10^{-23}$  J. We can then infer the following necessary conditions for observing strong Coulomb blockade in a tunnel junction device: temperature  $T < E_c/k_B = 0.9$  K, bias voltage  $V < E_c/e = 80$   $\mu$ eV, and shielding of junction from photon irradiation for frequencies  $f > E_c/h = 20$  GHz. To exclude also  $k$ -photon processes for  $k > 1$ , the shielding should be effective already for frequencies  $f > E_c/(kh)$ .

We will now derive a general expression for the change in the energy of a tunneling quasiparticle due to charging effects. Let there be  $N$  metallic islands and  $M$  voltage terminals. We will use subscript  $i$  for the terminals, and subscripts  $j$  and  $k$  for the islands. The relevant information about the geometry of the system is encoded in capacitance matrices  $C$  and  $C^0$  such that the capacitance between islands  $j$  and  $k$  is given by  $C_{jk}$ , and the capacitance between island  $j$  and terminal  $i$  by  $C_{ji}^0$ . The diagonal term  $C_{jj}$  describes the self-capacitance of island  $j$ , i. e., the capacitance to a ground potential surrounding the island at an infinite distance. By definition,  $C$  is symmetric. For island  $j$ , we denote the potential by  $v_j$  and

the total charge by  $q_j$ . The electric potential of terminal  $i$  is kept at  $V_i$  by an ideal voltage source. Illustration of a two-island configuration is given in Fig. 2.5.

We seek to describe the electrostatic energy of the system as a function of the voltages  $V_i$  and island charges  $q_j$ . Charge conservation for island  $j$  gives

$$\sum_k C_{jk}(v_j - v_k) + \sum_i C_{ji}^0(v_j - V_i) = q_j, \quad (2.36)$$

or, equivalently,

$$\underbrace{\left( \sum_k C_{jk} + \sum_i C_{ji}^0 \right)}_{C_{jj}^\Sigma} v_j - \sum_k C_{jk} v_k = q_j + \sum_i C_{ji}^0 V_i. \quad (2.37)$$

We introduce the diagonal matrix  $C^\Sigma$  whose elements are defined as indicated above. Furthermore, we define matrix  $A = C^\Sigma - C$ . Eq. (2.37) can be written equivalently in matrix form as

$$A\mathbf{v} = \mathbf{q} + C^0\mathbf{V}, \quad (2.38)$$

where the bold symbols are column vectors with a row for each island. The above equation gives a mapping between island charges and island voltages. The electrostatic energy  $U$  of the system is contained in the capacitors,

$$U = \frac{1}{2} \sum_{jk} \frac{1}{2} C_{jk} (v_j - v_k)^2 + \sum_{ij} \frac{1}{2} C_{ji}^0 (v_j - V_i)^2. \quad (2.39)$$

Note that each island pair is counted twice in the first summation, hence the factor 1/2. Let us expand Eq. (2.39) as

$$U = \frac{1}{2} \sum_j \left( \sum_k C_{jk} + \sum_i C_{ji}^0 \right) v_j^2 - \frac{1}{2} \sum_{jk} v_j C_{jk} v_k - \sum_{ij} V_i C_{ji}^0 v_j + \text{const.} \quad (2.40)$$

The constant term is a function of the external voltages  $V_i$  only, and can be neglected. From the above equation, we identify the matrix form

$$U = \frac{1}{2} \mathbf{v}^\top A \mathbf{v} - \mathbf{v}^\top C^0 \mathbf{V}. \quad (2.41)$$

Let us now consider a tunneling event where the charge state is changed from  $\mathbf{q}$  to  $\mathbf{q} + \delta\mathbf{q}$ . Incidentally, the potential is changed from  $\mathbf{v}$  to  $\mathbf{v} + \delta\mathbf{v}$ . First, we consider the case where a quasiparticle is transferred between two islands, say, from  $k$  to  $k'$ . The work done by a voltage source is equal to its voltage times the transferred charge. Thus, the work done by all the sources is

$$W = - \sum_{ij} C_{ji}^0 \delta v_j V_i = -\delta\mathbf{v}^\top C^0 \mathbf{V}. \quad (2.42)$$

The change in electrostatic energy is obtained from Eq. (2.41) as

$$\Delta U = \delta \mathbf{v}^\top A \mathbf{v} + \frac{1}{2} \delta \mathbf{v}^\top A \delta \mathbf{v} - \delta \mathbf{v}^\top C^0 \mathbf{V}, \quad (2.43)$$

where we have utilized the fact that  $A$  symmetric. Subtracting Eq. (2.43) from (2.42), we obtain the amount by which the energy of the quasiparticle is changed,

$$\Delta E = W - \Delta U = -\delta \mathbf{v}^\top A \left( \mathbf{v} + \frac{1}{2} \delta \mathbf{v} \right) = -\delta \mathbf{q}^\top A^{-1} \left( \mathbf{q} + \frac{1}{2} \delta \mathbf{q} + C^0 \mathbf{V} \right). \quad (2.44)$$

The rightmost form in the above equation inspires us to define a charging energy potential  $F_c$  as

$$F_c = \frac{1}{2} (\mathbf{q} + C^0 \mathbf{V})^\top A^{-1} (\mathbf{q} + C^0 \mathbf{V}), \quad (2.45)$$

so that  $\Delta E = -\Delta F_c$  for tunneling between two islands. Next, we consider tunneling between a voltage terminal and an island. If the electron is extracted from (deposited to) terminal  $i$ ,  $\pm e$  should be added to the charge transferred from terminal  $i$  in Eq. (2.42). Thus, for tunneling from (to) terminal  $i$ , we have

$$\Delta E = \pm e V_i - \Delta F_c. \quad (2.46)$$

Finally, we may express the island charges  $q_j$  in terms of the number of elementary charges  $n_j$  deposited on the island,  $q_j = e n_j$ , assuming the islands are initially neutral.

The potential  $F_c$  defined by Eq. (2.45) is a quadratic polynomial of the variables  $n_j$ . For any index  $j$ , it can be written as

$$F_c = E_{c,j} (n_j - n_{g,j})^2 + C_j, \quad (2.47)$$

where  $E_{c,j}$  is interpreted as the charging energy for island  $j$ , and  $n_{g,j}$  is the effective gate charge that depends on the voltages  $V_i$  and charge states of the other islands  $n_k$ ,  $k \neq j$ . The constant  $C_j$  contains terms without  $n_j$  dependence, which consequently do not affect the charge dynamics of island  $j$ . It is now evident from the forms of Eqs. (2.45) and (2.47) that one can tune the energy landscape of different  $\{n_j\}$  configurations via the macroscopic voltages  $V_i$ . The effect of voltage terminal  $V_i$  on island  $j$  is mediated as the induced gate charge term  $C_{ji}^0 V_i$ .

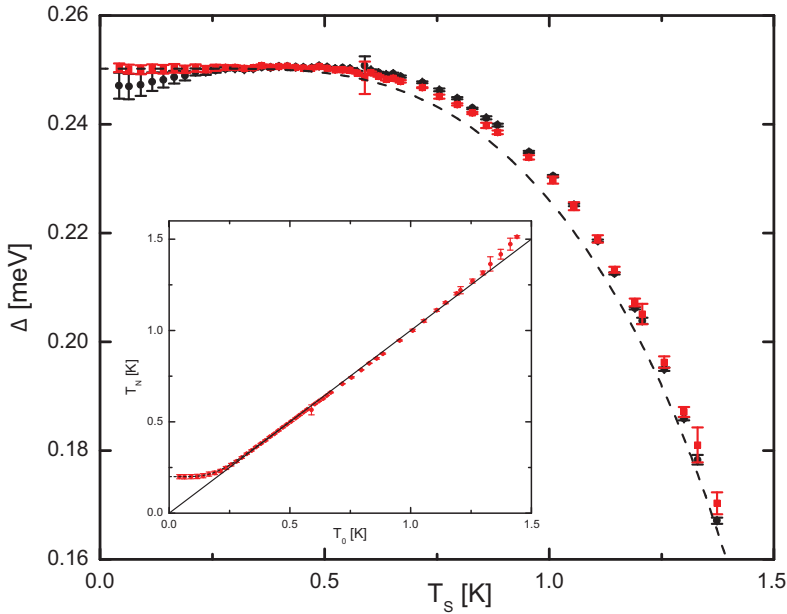


**Figure 2.6.** BCS gap of thin film aluminum as a function of temperature as determined by tunneling spectroscopy performed with an NIS junction. Using the theory of Sec. 2.3.2, we fitted either  $\Delta$  (black spheres), or  $\Delta$  and  $T_N$  (red squares) from the observed  $I$ - $V$  characteristics of the junction at different bath temperatures. Dashed line is the BCS theory prediction inferred from Eq. 2.50 with  $\Delta = 250 \mu\text{eV}$  in the weak coupling limit  $k_B T_c / (\hbar\omega_c) \ll 1$ . The inset shows the fitted  $T_N$  values versus the bath temperature, illustrating that the methods for determining the bath and junction temperatures are consistent at least in the temperature range  $0.25 \text{ K} < T < 1.3 \text{ K}$ , and that the normal electrode in this experiment was subject to a residual heating that caused its temperature to saturate around 200 mK.

## 2.3 Superconducting structures

### 2.3.1 Quasiparticles in BCS superconductors

Vanishing electrical resistance and the ability to repel magnetic fields are signatures of superconductivity that can be easily perceived at the macroscopic scale [56]. In more sophisticated structures, further unique phenomena pertaining to the quantum mechanical coherence properties of superconductors can be observed. At the microscopic level, superconductivity can be understood through Bardeen-Cooper-Schrieffer (BCS) theory [57, 58]. The theory predicts that an attractive interaction between conduction electrons will result in the realization of a superconducting ground state through the condensation of Cooper pairs, i. e., bound states

of two electrons. The origin of the attractive interaction between electrons is their coupling to the lattice phonons. Two characteristic features of the superconducting state are a finite, material-dependent energy gap  $\Delta$  against single-electron excitations, and a complex-valued order parameter with a well-defined phase.

From the BCS theory, the elementary excitations in a superconductor are known to be Bogoliubov quasiparticles. In the microscopic description, they consist of a phase-coherent pair of an electron and a hole having opposite wave vectors and spins. However, physical phenomena related to single-quasiparticle tunneling between a superconductor and a normal metal can be analyzed without an explicit treatment of the coherence factors. In the so-called semiconductor model [56], the essential property of superconducting electrode is its energy-dependent density of the quasiparticle states. The BCS expression for the quasiparticle density of states reads

$$N_S(E) = N_0 \frac{|E|}{\sqrt{E^2 - \Delta^2}} \Theta(|E| - |\Delta|), \quad (2.48)$$

where the energy  $E$  is taken relative to the Fermi level, and  $N_0$  is the density of states in the normal state. For aluminum,  $N_0 = 1.45 \times 10^{47} \text{ m}^{-3} \text{ J}^{-1}$  [1, 59]. From a device perspective, the most crucial features of  $N_S$  as defined in Eq. (2.48) are the complete absence of quasiparticle states for  $|E| < \Delta$ , and the singularities at  $|E| = \Delta$ . However, many recent transport experiments on tunnel junctions [60, 61, 62, 63, 64], also see Ref. [65] and the references within, display behavior that is better described by a phenomenological life-time broadened expression

$$N_S(E) = N_0 \left| \text{Re} \left[ \frac{E + i\Gamma}{\sqrt{(E + i\Gamma)^2 - \Delta^2}} \right] \right|, \quad (2.49)$$

where  $\Gamma$ , or its dimensionless equivalent  $\gamma = \Gamma/\Delta$ , is called the Dynes parameter. Values for  $\gamma$  in the cited studies fall in the range  $10^{-2} \dots 10^{-6}$ . The simple life-time broadened expression was originally introduced by Dynes *et al.* for studies of superconductivity in Pb–Bi-alloys [17], and later in granular aluminum films [18]. Particularly in Ref. [17], the experimentally measured broadening terms  $\Gamma$  were found to be in good agreement with the theoretically estimated quasiparticle recombination times  $\tau_r$  for  $\tau_r \lesssim 2 \times 10^{-10} \text{ s}$ .

A finite Dynes parameter induces a quasiparticle density of states equal to  $\gamma N_0$  at the midpoint of the gap. In transport measurements, this would appear as a leakage channel in parallel with the ideal BCS junction. When analyzing experimental  $I$ – $V$  characteristics, the fitted value of  $\gamma$

is sometimes interpreted as an indicator of junction quality on the basis that low-quality junctions often display large sub-gap leakage. As one of the main results of this thesis, we will show that the inherent limit for the  $\gamma$  parameter in opaque Cu/Al junctions fabricated with the standard process, if such a limit exists, is not larger than  $1.6 \times 10^{-7}$ . Leakage currents observed in typical transport measurements can be attributed to mechanisms other than real sub-gap states, some of which we will discuss in Secs. 4.2 and 4.3.

The temperature behavior of the gap parameter  $\Delta$  can be inferred from the relation [56]

$$\frac{1}{N_0 V} = \int_0^{\hbar\omega_c} \frac{\tanh \left[ \sqrt{\epsilon^2 + \Delta^2} / (2k_B T) \right]}{\sqrt{\epsilon^2 + \Delta^2}} d\epsilon, \quad (2.50)$$

where  $T$  is the temperature, and  $\hbar\omega_c$  and  $V$  describe the cut-off energy and strength of the attractive electron-electron interaction. The expected behavior is that  $\Delta$  achieves its maximum value at  $T = 0$ , and vanishes at a critical temperature  $T_c$ . The  $T_c$  of bulk aluminum is 1.2 K [66], whereas the figures observed in thin films are generally higher depending on film thickness, grain size, and oxygen impurity concentration [67, 59, 68]. For weak-coupling superconductors with  $k_B T_c / (\hbar\omega_c) \ll 1$ , one has the relation

$$\Delta(0) \simeq 1.76 k_B T_c \quad (2.51)$$

that links the zero-temperature gap and the critical temperature. In Fig. 2.6, we show the measured superconducting gap of an aluminum thin film in the temperature range 0.05 – 1.3 K. The experimental value of  $\Delta$  was determined by a fit to the measured  $I$ – $V$  characteristic of a Cu/Al NIS junction. The data agrees quite well with the theoretical curve obtained from a numerical solution of Eq. (2.50) for  $\Delta = 250 \mu\text{eV}$ .

### 2.3.2 The NIS junction

In this section, we will consider electric transport through an NIS junction in the framework of orthodox theory laid down in the previous chapters. The basic results are expressions for the electric and heat currents in terms of the change in energy for a tunneling quasiparticle, denoted by  $E$ . In the most elementary case of a low-impedance voltage bias, the change in energy is equal to  $\pm eV$ , where the sign is chosen according to whether the quasiparticle tunnels in the direction of the bias (+) or against it (–). In the model, the electric transport through the junction is described by only two parameters: the tunneling resistance  $R_T$  [discussed

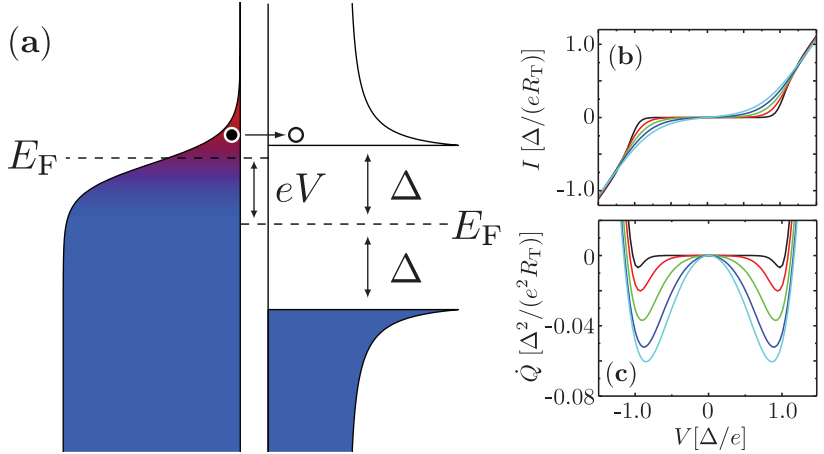


**Figure 2.7.** (a) Schematic illustration of electron transport through a NIS junction. The shaded regions represent the Fermi-Dirac distribution in the normal electrode (left), and the superconducting quasiparticle density of states according to BCS theory (right). The Fermi levels  $E_F$  in the two electrodes are indicated by the dashed lines, and they are shifted relative to each other by an applied voltage bias  $V$ . The panels on the right show electric current (b) and heat flow to the normal metal (c) through an NIS junction as a function of bias voltage at different temperatures calculated from orthodox theory with no sub-gap states. In the order of decreasing current and cooling power, the temperatures are  $0.25T_c$ ,  $0.2T_c$ ,  $0.15T_c$ ,  $0.1T_c$ , and  $0.05T_c$ .

in detail in Sec. (2.1.2)], and the gap parameter  $\Delta$  of the superconducting lead [see Sec. (2.3.1)]. Despite the apparent simplicity of the model, it can produce quantitatively correct predictions in many experimentally interesting cases.

In the NIS case, the general result of Eq. (2.7) yields

$$\Gamma_{N \rightarrow S}(E) = \frac{1}{e^2 R_T} \int_{-\infty}^{\infty} dE' n_S(E' + E) [1 - f_S(E' + E)] f_N(E'), \quad (2.52)$$

$$\Gamma_{S \rightarrow N}(E) = \frac{1}{e^2 R_T} \int_{-\infty}^{\infty} dE' n_S(E') f_S(E') [1 - f_N(E' + E)], \quad (2.53)$$

where  $n_S(E)$  is the normalized BCS density of states [see Sec. 2.3.1], and  $f_S(E)$  and  $f_N(E)$  are the quasiparticle occupation factors for the superconductor and normal metal. We assume that the quasiparticles in the normal and superconducting electrodes are in quasi-equilibrium, i. e., they follow a Fermi-Dirac distribution at some temperatures  $T_N$  and  $T_S$ , respectively. Under these assumptions, Fig 2.7(a) illustrates the density of states and occupation factors on both sides of an NIS junction.

It follows from basic symmetries of  $f_N$ ,  $f_S$  and  $n_S$  that  $\Gamma_{N \rightarrow S}(E)$  and  $\Gamma_{S \rightarrow N}(E)$  are equal. Hence, we can drop the subscripts and consider a single quasiparticle transition rate  $\Gamma(E)$ . For a voltage-biased junction,

the time-averaged current through the junction is related to the transition rates by

$$I(V) = e[\Gamma(eV) - \Gamma(-eV)]. \quad (2.54)$$

Figure 2.7(b) displays the theoretical large-scale  $I$ - $V$  characteristic at different temperatures. Approximately at voltage  $\pm\Delta/e$ , which we will refer to as the gap voltage, one finds an onset of current which becomes sharper as the temperature is decreased.

For many applications, it is important to consider the heat carried by the quasiparticles as well. A single quasiparticle of energy  $E$  deposited to (extracted from) an electrode adds (removes) an amount  $E - E_F$  of heat. The integrands of Eqs. (2.52) and (2.53) yield the distribution of energy for the tunneling quasiparticles. Consequently, we obtain the following integral forms for the average heat power incident on electrode N

$$\dot{Q}_{N \rightarrow S}^N(E) = -\frac{1}{e^2 R_T} \int_{-\infty}^{\infty} dE' E' n_S(E' + E) [1 - f_S(E' + E)] f_N(E'), \quad (2.55)$$

$$\dot{Q}_{S \rightarrow N}^N(E) = \frac{1}{e^2 R_T} \int_{-\infty}^{\infty} dE' (E' + E) n_S(E') f_S(E') [1 - f_N(E' + E)]. \quad (2.56)$$

Again, by symmetry, one has  $\dot{Q}_{S \rightarrow N}^N(E) = \dot{Q}_{N \rightarrow S}^N(E)$  and we drop the subscripts. Furthermore, we have the relation

$$\dot{Q}^S(E) = -\dot{Q}^N(E) + eT(E) \quad (2.57)$$

that can be derived by algebraic manipulation or by considering conservation of energy. The total heat load on each electrode of a voltage biased junction is obtained by summing up both tunneling directions, i. e.,

$$\dot{Q}_{\text{tot}}^N(V) = \dot{Q}^N(eV) + \dot{Q}^N(-eV), \quad (2.58)$$

$$\dot{Q}_{\text{tot}}^S(V) = -\dot{Q}_{\text{tot}}^N(V) + I(V)V. \quad (2.59)$$

A peculiar property of the NIS junctions is that for bias voltages slightly less than the gap voltage  $\Delta/e$ , one finds a region where  $\dot{Q}_{\text{tot}}^N(V)$  is negative, i. e., the normal electrode is cooled. Considering the preceding discussion on the heat carried by tunneling quasiparticles, it is evident that cooling can be brought upon by extracting quasiparticles from above the Fermi level or depositing them below it. In Fig. 2.7(c), we show the simulated total heat flow to the normal electrode as a function of voltage at different temperatures.

Equations (2.52)–(2.59) allow the electric and heat currents through an NIS junction to be evaluated for different bias voltages  $V$  and electrode temperatures  $T_S$  and  $T_N$ . The associated integrals cannot be evaluated

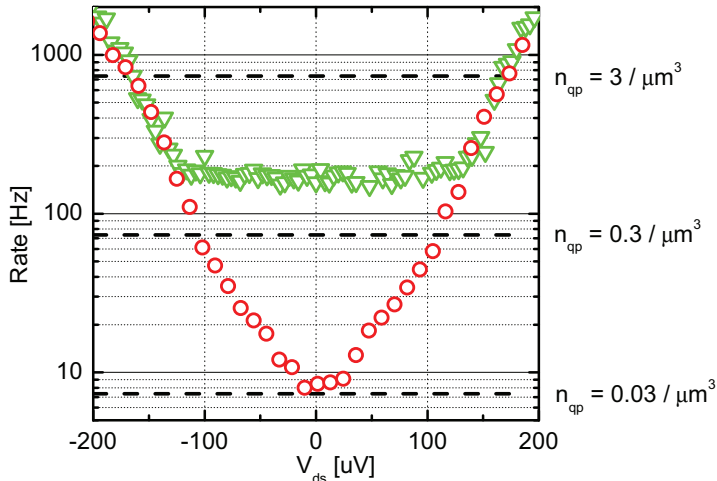


**Figure 2.8.** Determining the density of non-equilibrium quasiparticles from tunneling rate data of Pub. IX. Red spherical markers are data from a sample with direct NS-contacts for quasiparticle evacuation, whereas the green triangle markers correspond to a sample where quasiparticle evacuation occurs solely through the tunneling barrier oxide to the overlapping normal metal shadow. The thick dashed horizontal lines show the bias-independent tunneling rates induced by the stated densities of non-equilibrium quasiparticles according to Eq. (2.63). Relevant sample parameters here are  $N_0 = 1.45 \times 10^{47}$  and  $R_T = 0.55 \text{ M}\Omega$ , accounting for the parallel connection of the two  $1.1 \text{ M}\Omega$  junctions of the SET.

exactly in closed form, mandating the use of numerical methods for a direct application of the model. However, analytical approximations exist for different operation points, and the ones most relevant to the subsequent experiments are discussed below. A more extensive treatment of the NIS transport integrals is given in Ref. [69].

In anticipation of electron counting experiments and measurements performed on Coulomb blocked NIS devices, the primary quantity we are interested in is the directional tunneling rate  $\Gamma(E)$  instead of the  $I(V)$  dependence. When the energy gain in tunneling is large compared to  $\Delta$ , the tunneling rates are the same as for a fully normal junction,

$$\Gamma(E) = \frac{E}{e^2 R_T} \quad \text{for } E \gg \Delta. \quad (2.60)$$

The sub-gap behavior of a junction with electrodes thermalized to  $T_S, T_N \ll \Delta/k_B$  is captured well by the following approximation:

$$\Gamma(E) = \frac{\Delta}{e^2 R_T} \left[ K_1\left(\frac{\Delta}{k_B T_S}\right) + e^{E/k_B T_N} K_1\left(\frac{\Delta}{k_B T_N}\right) \right], \quad \text{for } |E| \lesssim \Delta \quad (2.61)$$

where  $K$  denotes the modified Bessel function of the second kind. Equation (2.61) illustrates that in the range  $0 < E < \Delta$ , there is a region where

the tunneling rate has an exponential dependence on  $E/(k_B T_N)$ . On the other hand, the effect of a finite  $T_S$  is to add a constant "background" rate that has no energy dependence for  $|E| \lesssim \Delta$ . These properties enable NIS junctions to be used as sensitive probes of the electron temperature of the normal electrode. Assuming  $T_N = T_S = T$ , Eq. (2.61) can be further simplified into

$$\Gamma(E) = \sqrt{\frac{\pi k_B T \Delta}{2}} \frac{e^{-\Delta/(k_B T)}}{e^2 R_T} \left[ 1 + e^{E/(k_B T)} \right] \quad (2.62)$$

by replacing the Bessel function by the first term in its asymptotic series expansion.

While  $T_S$  term of Eq. (2.61) has no influence on the total current  $e[\Gamma(E) + \Gamma(-E)]$  due to the lack of bias dependence, the tunneling events described by it are real and can be detected in an electron counting experiment. Consistently with Refs. [59] and [70], we define the volumetric density of quasiparticles as

$$n_{\text{qp}} = 2N_0 \int_{\Delta}^{\infty} dE n_S(e) f_S(E), \quad (2.63)$$

where  $N_0$  is the density of electronic states at Fermi level in the normal state. Now, the  $T_S$  term of Eq. (2.61) can be written in terms of  $n_{\text{qp}}$  as

$$\Gamma^{\text{qp}} = \frac{1}{e^2 R_T} \int_{\Delta}^{\infty} dE' n_S(E') f_S(E') \quad (2.64)$$

$$= \frac{n_{\text{qp}}}{2e^2 R_T N_0}. \quad (2.65)$$

Since  $N_0$  is a material parameter, and the junction resistance  $R_T$  can be calibrated from other measurements,  $n_{\text{qp}}$  can be reliably inferred from the observed value of  $\Gamma^{\text{qp}}$ . The insensitivity of  $\Gamma^{\text{qp}}$  to biasing conditions enables one to distinguish it from other sub-gap processes. In Fig. 2.8, we show a part of the measured sub-gap rates reported in Pub. IX. In the dataset for the sample having an effective quasiparticle trap, no plateau is observed and an upper bound of  $n_{\text{qp}} < 0.033 \mu\text{m}^{-3}$  can be inferred. In contrast, a clear plateau corresponding to  $n_{\text{qp}} = 0.69 \mu\text{m}^{-3}$  is observed for the reference sample lacking such a trap.

For describing cooler devices, approximations of the heat flow integral in Eq. (2.55) are important. The basic result, valid at  $T_N, T_S \ll \Delta/k_B$ , is that the cooling power of a single NIS junction assumes its maximum value of

$$\dot{Q}_{\text{opt}}^{\text{N}} = -0.59 \frac{\Delta^{1/2} (k_B T)^{3/2}}{e^2 R_T} \quad (2.66)$$

at the bias voltage given by

$$V_{\text{opt}} = (\Delta - 0.66 k_B T)/e. \quad (2.67)$$

In Sec. 4.1, we discuss cooler devices that exhibit significant charging effects. For these devices, the analysis of steady-state electric and heat transport can be carried out by considering typical trajectories in the charge configuration space, or by master equation methods. In both approaches, an essential quantity is the average heat  $\langle Q \rangle$  carried by a quasiparticle as a function of the energy  $E$ . From Eqs. (2.52), (2.55), and (2.57), we find

$$\langle Q^N(E) \rangle = \frac{\dot{Q}^N(E)}{\Gamma^N(E)} \approx E - \Delta - \frac{(1 + \xi)k_B T}{2}, \quad (2.68)$$

$$\langle Q^S(E) \rangle = -\langle Q^N(E) \rangle + E, \quad (2.69)$$

where the coefficient  $\xi$  in the analytical approximation of  $\langle Q^N(E) \rangle$  is a slowly increasing function of  $(E - \Delta)/k_B T$ , which vanishes in the limit  $E \rightarrow -\infty$  and is approximately equal to 0.26 at  $E = \Delta$ . A cooler device operating near the optimum bias of Eq. (2.67) thus extracts about  $k_B T$  of heat from the normal electrode per each tunneling electron.

To finish our theoretical overview of quasiparticle transport in NIS structures, we address the rate parameter for the two-electron Andreev process. For any device whose mode of operation is based on the sequential single-electron tunneling picture, coherent multi-electron processes constitute a mechanism for unwanted current leaks through the device. For electron pumps, for example, the lowest-order process that persists in the  $T \rightarrow 0$  limit sets the fundamental accuracy of the device. In Ref. [71], Averin and Pekola analyze the theoretical rates of multi-electron processes in NISIN and SINIS-type single-electron transistors. They find that two-electron Andreev tunneling is the dominating higher-order process in a SINIS SET with  $E_c < \Delta$ . Earlier, it was shown that Andreev-induced leakage can be observed in the  $I$ - $V$  characteristics of high-quality NIS junctions [65]. In this process, two electrons forming a Cooper pair are transferred coherently through the junction in either direction. Since no quasiparticle excitations are created in the superconductor, the threshold energy is zero.

In the experiments of this thesis,  $2e$  Andreev processes were observed in SINIS-type SETs and NIS-type single-electron boxes. The theoretical analysis of Ref. [71] was performed in the same quasi-1d ballistic geometry that we utilized in Sec. 2.1.2. The resulting expression for rate param-

eter as a function of the change in electrostatic energy  $E$  reads

$$\Gamma^{2e}(E) = \frac{1}{e^2 R_T} \times \frac{g}{16\pi\mathcal{N}} \int dE' f(E' - E/2) f(-E' - E/2) \times \left| \sum_{\pm} a(\pm E' + E_c - i\gamma_1/2) \right|^2, \quad (2.70)$$

$$a(E) = \frac{\Delta}{\sqrt{E^2 - \Delta^2}} \ln \left[ \frac{\Delta - E + \sqrt{E^2 - \Delta^2}}{\Delta - E - \sqrt{E^2 - \Delta^2}} \right], \quad (2.71)$$

where  $g = \hbar/(R_T e^2)$  is the normalized conductance of the junction,  $\mathcal{N}$  is the number of transport modes, and  $\gamma_1$  is a life-time broadening parameter. The origin of the life-time term  $\gamma_1$  are the competing one-electron processes, but in practice the dependence of the rate parameter on  $\gamma_1$  is weak, and a convenient small number can be used to suppress the divergences of the  $a(E)$  term. We present quantitative results calculated with Eqs. (2.70)–(2.71) in Sec. 4.3.

Compared to the single-electron rate of Eq. (2.52), the prefactor for the Andreev rate has an additional dependence on the quantity  $\zeta = g/\mathcal{N}$ , i. e., the normalized conductance per transport mode. Since both  $g$  and  $\mathcal{N}$  are proportional to the junction area, the parameter  $\zeta$  depends on the properties of the tunneling barrier only. From our previous treatment of first-order quasi-1d tunneling [see Eq. (2.15)], we find  $\zeta = T/(2\pi)$ , where  $T$  is the barrier penetration probability for a quasiparticle with longitudinal energy  $E_F$ . However, the barrier parameters needed to estimate  $T$  according to Eq. (2.16) are difficult to determine experimentally. Alternatively, one can write

$$\zeta = \frac{\hbar}{e^2} \times \frac{A_{\text{ch}}}{R_T A}, \quad (2.72)$$

where  $A_{\text{ch}}$  is a phenomenological parameter describing the area of one quantum channel. In Pub. VIII, we obtained  $\zeta = 4 \times 10^{-5}$  for a device with  $R_T A = 2.8 \text{ k}\Omega \mu\text{m}^2$  (junction size  $40 \text{ nm} \times 35 \text{ nm}$ ), yielding  $A_{\text{ch}} = 30 \text{ nm}^2$ . A further analysis of the data from Pub. IX, presented in Sec. 4.3, gives  $\zeta = 10^{-5}$  and  $R_T A = 14 \text{ k}\Omega \mu\text{m}^2$  (junction size  $110 \text{ nm} \times 110 \text{ nm}$ ), resulting in  $A_{\text{ch}} = 35 \text{ nm}^2$  for a device fabricated with the same fabrication process but different process parameters. We recall the theoretical estimates  $A_{\text{ch}} = 1.4 \text{ nm}^2$  and  $2.5 \text{ nm}^2$ , which we obtained earlier based on Eq. (2.18) and different parameters of  $\text{AlO}_x$  barriers reported in the literature. The large discrepancy between the theoretical and experimental values suggests a hypothesis that only 4–8% of the junction area participates actively in the tunneling process. At the microscopic level, this would follow from small variations in the thickness of the barrier oxide.

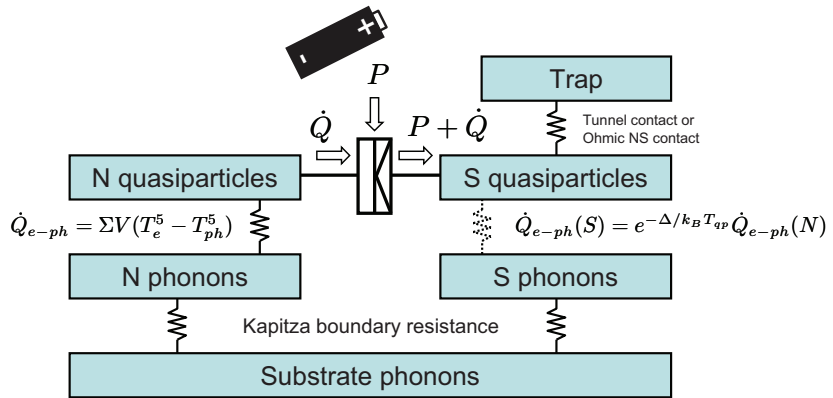


**Figure 2.9.** Schematic model of the heat flows in a mesoscopic NIS junction device.

However, it is theoretically known [31] and has been experimentally observed [72, 73, 74] that a phase-coherent, diffusive motion of quasiparticles in the electrodes can result in interference effects that increase the probability of two-electron Andreev tunneling. It is then interesting to compare our results to those of Greibe *et al.* [65] obtained for somewhat larger Al/AlO<sub>x</sub>/Cu junctions up to  $400 \times 400$  nm in size. Analyzing the observed subgap conductance curves within a theoretical model of diffusive Andreev tunneling, they infer a participation ratio of 13%, i. e., approximately twice as large as the figure we report. In light of these numbers, our devices may operate in a regime where the ballistic and diffusive contributions are of equal magnitude.

## 2.4 Heat flows in mesoscopic systems

In the design of any low-temperature experiment, thermal insulation and thermal anchoring are central topics. Issues related to thermalization are pronounced in the field of mesoscopic physics, where sample volumes and cross-sectional areas are small, and in experiments with superconducting components, owing to the vanishing electronic heat conductance. Figure 2.9 illustrates the relevant thermal reservoirs in a typical NIS junction device, such as an electronic cooler. We will only consider steady-state heat flows, in which case the heat capacities do not play a role in the analysis.

First, we address the electron system of the normal metal electrode, and its coupling to the lattice phonons. In the quasiclassical diffusive limit as

defined in, e. g., Ref. [75], the state of the electron gas is determined by its energy distribution, which we have denoted by  $f_N(E)$  in earlier sections. The processes that compete to determine the shape of the distribution are the electron-electron relaxation, characterized by the scattering time  $\tau_{e-e}$ , electron-phonon relaxation with scattering time  $\tau_{e-ph}$ , and quasiparticle injection with rate  $\tau_{inj}$ . The temperature of the electron gas is well defined only when the occupation is given by a Fermi-Dirac distribution. Following Giazotto *et al.* [75], we identify three separate regimes as follows: Full equilibrium occurs when  $\tau_{e-e}^{-1} \gg \tau_{e-ph}^{-1} \gg \tau_{inj}^{-1}$ , resulting in the electron gas to be thermalized to the lattice temperature  $T_{ph}$ . In quasi-equilibrium,  $\tau_{e-e}^{-1} \gg \tau_{inj}^{-1} \gg \tau_{e-ph}^{-1}$ , and the energy distribution is still a Fermi-Dirac one, but at a temperature  $T_N$  not necessarily equal to  $T_{ph}$ . By definition, an effective electronic cooler should be able to drive the electrons into quasi-equilibrium. Non-equilibrium is achieved when  $\tau_{inj}^{-1} \gg \tau_{e-e}^{-1}, \tau_{e-ph}^{-1}$ , and in this case the electrons do not have a well-defined temperature.

There are, however, ways to generalize the definition of temperature to cover also non-equilibrium distributions. One such generalization is presented in Ref. [76]. In this article, the authors are able to realize a non-thermal electron distribution in the normal electrode of a SINIS structure using 0.1–2 k $\Omega$  tunnel junctions for quasiparticle injection. Based on the fact that the tunnel junctions employed in this thesis are 100–1000 times more resistive than those of Ref. [76] while the device geometries are similar, significant non-equilibrium effects are not expected here.

The central theoretical results concerning the electron-phonon coupling are  $\tau_{e-ph}^{-1} \sim T^4$  for disordered samples [77] and  $\tau_{e-ph}^{-1} \sim T^3$  in the pure limit [78]. Experimental results on Cu films presented in Ref. [79] seem to agree with the  $T^4$  behavior, but the data is not strong enough to allow for a reliable determination of the exponent. They report  $\tau_{e-ph}^{-1} = 100$  kHz at 200 mK for a Cu island having dimensions of 500  $\mu\text{m} \times 45 \text{ nm} \times 300 \text{ nm}$ . The exponent  $T^3$  seems to be more prevalent in the literature [80, 11, 81, 75], and we will also employ it in our analysis. It can be shown that if the electron-phonon relaxation rate has a temperature dependence of  $T^p$ , the electron-phonon heat flow is proportional to  $T_{ph}^{p+2} - T_N^{p+2}$  [82]. Therefore, the heat flux to the normal metal electrons from the electron-phonon coupling is given by

$$\dot{Q}_{e-p} = \Sigma \mathcal{V} (T_{ph}^5 - T_N^5), \quad (2.73)$$

where  $\Sigma$  is a material parameter, and  $\mathcal{V}$  is the volume of N island. The values of  $\Sigma$  for copper found in the literature are (in units of  $\text{Wm}^{-3}\text{K}^{-5}$ )

$2.0 \times 10^9$  [80, 81], and  $(0.9 - 4) \times 10^9$  [11].

The phonon system of the normal electrode, at temperature  $T_{\text{ph}}$ , is treated here as a separate entity from the substrate phonons at  $T_0$  mainly for illustrative purposes only. In Ref. [83], it is argued that the comparable Kapitza boundary resistance between a metallic thin film and the interface layer of a substrate vanishes since the average phonon wavelength  $\lambda_p$  is larger than the film thickness. A quantitative upper bound for the Kapitza boundary resistance can be obtained using bulk values from Ref. [84]. The reported result from an acoustic mismatch calculation between copper and silicon reads

$$R_K = \frac{14.3 \text{ K}^4 \text{W}^{-1} \text{cm}^2}{T_{\text{ph}}^3 A}, \quad (2.74)$$

where  $A$  is the surface area of the interface. Comparing the above result to Eq. (2.73), we infer that the change in the phonon temperature of a normal electrode is less than 10% of the observed drop in the electron temperature assuming a film thickness of  $\nu/A = 20$  nm and  $T < 300$  mK. We note that Rajauria *et al.* [85] report of experiments performed in the standard SINIS cooler geometry where they observed a drop of 50 mK in the phonon temperature of the Cu island starting from a bath temperature of 489 mK.

In practical SINIS coolers, the evacuation of the quasiparticle excitations created in the superconductor by the tunneling current can be problematic. The heat flow of the electron-phonon coupling in a superconductor is reduced approximately by a factor  $e^{-\Delta/(kT_s)}$  compared to the normal state [86]. In high-performance designs, the superconductor heating has been mitigated by normal-metal quasiparticle traps connected directly to the superconducting electrode near the cooling junction [87], or by alternative cooler geometries that reduce the quasiparticle density near the junctions [88].

Fortunately, an NIS sample fabricated with the standard Fulton-Dolan process [see Sec. 3.1] almost always features a form of a quasiparticle trap even without deliberate planning: Typically at a distance of few micrometers from the junction, the superconducting electrode starts to overlap with its normal metallic copy, which is an unavoidable side-product of the shadow evaporation method. This phenomenon is well illustrated in the scanning electron micrograph of a real sample shown in Fig. 3.1(c). Quasiparticle excitations from the superconductor can then tunnel through the oxide barrier to the normal metal, where their excess energy is transported to the lattice via the much stronger electron-phonon coupling in

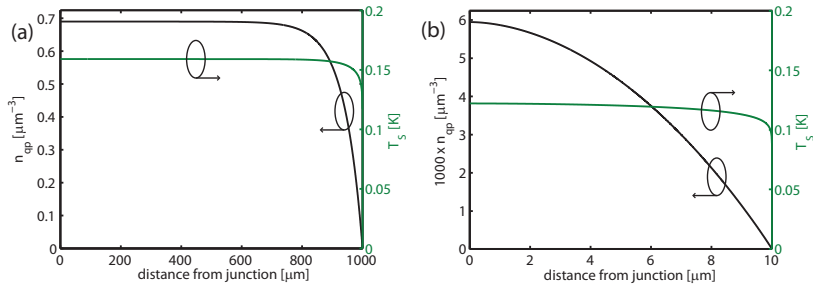


**Figure 2.10.** Induced quasiparticle density  $n_{qp}$  and the equivalent  $T_S$  by a homogeneous source term in a quasi-1d geometry where an ideal quasiparticle trap is placed at a distance of 1000  $\mu\text{m}$  [panel (a)] or 10  $\mu\text{m}$  [panel (b)] of a tunnel junction. The parameters correspond to the experimental conditions realized in Pub. IX.

the normal metal. Due to a combination of this trapping effect and relatively low injection currents, significant effects attributable to overheating of the superconducting electrodes were not observed in most of the experiments of this thesis.

The exception is the experiment of Pub. IX, where the employed electron counting technique allowed even low quasiparticle densities to be observed. For  $T_S \ll \Delta/k_B$ , Eq. (2.63) can be approximated as

$$n_{qp} = \sqrt{2\pi\Delta k_B T_S} N_0 e^{-\Delta/(k_B T_S)}, \quad (2.75)$$

illustrating that  $n_{qp}$  and  $T_S$  are interchangeable quantities, if a thermal distribution for the quasiparticle energies can be assumed. The measurement scheme of Pub. IX allowed the determination of  $n_{qp}$  with essentially zero quasiparticle injection. Hence, the observed finite quasiparticle density of  $n_{qp} = 0.69 \mu\text{m}^{-3}$  (corresponding to  $T_S = 159 \text{ mK}$ ) in the sample without an additional direct-contact quasiparticle trap is indicative of an external heat load incident on the superconducting electrodes creating quasiparticle excitations. Assuming that the quasiparticles are created homogeneously over the area of the superconducting lead, the injection rate per area can be estimated using Eq. (2.65) and the resistance-area product of the oxide. Since the SET junctions are realized with the same oxide, we can use the  $R_T A$  value of  $14 \text{ k}\Omega\mu\text{m}^2$  obtained for the junctions. In this manner, the injection rate is estimated to be  $6.6 \times 10^3 \text{ Hz}/\mu\text{m}^2$ , or  $2.2 \times 10^5 \text{ Hz}/\mu\text{m}^3$  assuming a constant volumetric injection over the film thickness  $h = 30 \text{ nm}$ .

These results can be compared directly with the figures obtained for superconducting resonators in Ref. [70] by Martinis *et al.* There, the authors

report a higher density of non-equilibrium quasiparticles,  $n_{\text{qp}} = 10/\mu\text{m}^3$ . However, due to the slower quasiparticle recombination rate in their purely superconducting sample, the corresponding volumetric injection rate is only  $2.4 \times 10^3 \text{ Hz}/\mu\text{m}^3$ . They also list possible mechanisms that could be responsible for the observed injection rate, including cosmic rays, background radioactivity, stray blackbody radiation from warmer parts of the cryostat, and heat release from sample materials. In another recent study on superconducting resonators [89], the quasiparticle density was observed to saturate similarly at  $25 - 55/\mu\text{m}^3$ . According to the authors, they can exclude the possibility that the quasiparticles observed in the experiment were generated by stray microwaves.

Finally, we discuss the results of Pub. IX obtained with a sample where the superconducting electrodes were terminated at a distance of approximately  $10 \mu\text{m}$  from the junction by a direct contact to a large normal metal electrode. The geometry of the trapping structure is visible in Fig. 3.1(b). In this case, we were able to infer the upper bound  $n_{\text{qp}} < 0.033 \mu\text{m}^{-3}$  ( $T_{\text{S}} < 122 \text{ mK}$ ) next to the junction. The combined trapping effect of the overlapping shadow and the direct contact can be estimated within the simple diffusion model presented in, e. g., Ref. [90]. The diffusion equation reads

$$-\nabla \cdot (\kappa \nabla n_{\text{qp}}) = -\alpha n_{\text{qp}} + j, \quad (2.76)$$

$$\kappa = l_0 v_F \sqrt{k_{\text{B}} T_{\text{S}} / (2\pi\Delta)}, \quad (2.77)$$

where  $l_0$  is the mean free path,  $v_F$  is the Fermi velocity,  $\alpha = (2e^2 N_0 R_{\text{T}} A h)^{-1}$  describes the effect of the shadow trap, and the constant term  $j$  is the volumetric injection rate. Since  $\kappa$  depends on  $T_{\text{S}}$ , a self-consistent solution is in principle needed. However, from Eq. (2.75) we can infer that the dependence is only logarithmic in  $n_{\text{qp}}$ , and an approximative solution with a constant  $\kappa$  is quite accurate. In order to model the situation of Pub. IX, it is sufficient to consider a 1d geometry with the boundary conditions  $\frac{\partial n_{\text{qp}}}{\partial x}(x = 0) = 0$  and  $n_{\text{qp}}(x = L) = 0$ , which describe the vanishing injection at the tunnel junction and the assumed ideal trapping at distance  $L$  from the junction, respectively. The solutions corresponding to  $L = 1000 \mu\text{m}$  and  $10 \mu\text{m}$  are plotted in Figs. 2.10(a) and (b). We observe that an ideally functioning trap that evacuates all quasiparticles at  $x = 10 \mu\text{m}$  would result in  $n_{\text{qp}} = 0.006 \mu\text{m}^{-3}$  at the junction. In reality, the reduction is probably less dramatic than the result of this simple calculation indicates. However, it shows that the observed reduction

Theoretical basis

of  $n_{\text{qp}}$  from  $0.69 \mu\text{m}^{-3}$  to less than  $0.033 \mu\text{m}^{-3}$  by adding a quasiparticle trap is plausible.

## 3. Experimental methods

### 3.1 Sample fabrication

The samples studied in the experiments of this thesis consisted of lithographically patterned metallic thin films on an oxidized silicon substrate. Tunnel junctions were realized with the Fulton–Dolan method [55, 7]. Below, we give a brief overview of the various stages of the sample fabrication process. All the utilized cleanroom processes are well established in the field of microfabrication, and are described more thoroughly in, e. g., Ref. [91]. The exact process parameters varied between sample fabrication runs. The figures given below represent typical values.

The starting point of the process is a polished silicon wafer. The wafer has a thermally grown silicon dioxide surface layer with a nominal thickness of 300 nm. A polymer resist is prepared on top of the wafer by spin coating: A few milliliters of dissolved resist is poured on top of the wafer, which is then rotated with a spinner that spreads the solution uniformly on the wafer surface. Next, a soft bake on a hotplate removes the remaining solvent. For this work, a two-layer resist stack was fabricated using commercially available resists from the company Microchem. For the first layer, we used a poly(methylmetacrylate-methacrylic acid) [P(MMA-MAA)] solution in ethyl lactate, spun at 4000 RPM for 40 s, and then baked at 170 °C for 1–2 minutes. The second layer was a polymethylmetacrylate (PMMA) solution in anisole, spun at 2500 RPM for 40 s, and baked similarly as the first layer. A typical thickness obtained with the above recipe was 500 nm using a weight-by-weight (w/w) concentration of 11% for the P(MMA-MMA) solution and 4% for the PMMA. After spin coating, the wafer was cut into smaller segments and chips down to about 10 mm per side, which were then processed individually.

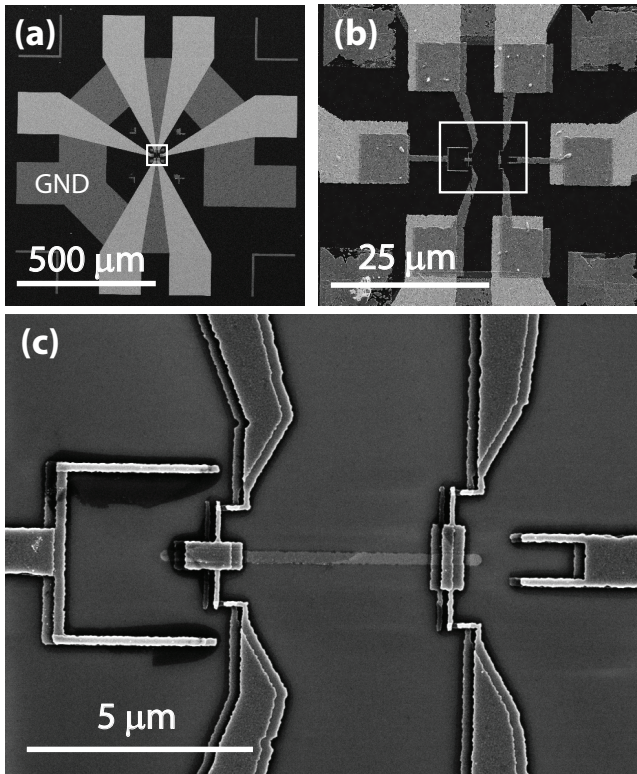


**Figure 3.1.** Scanning electron micrographs at three different magnifications of a sample fabricated with multi-step lithography. In panel (a), the metal film denoted by GND is the ground plane that is galvanically insulated from the sample leads on top of it by a 25 nm  $\text{AlO}_x$  layer. Similarly, the horizontal Cr wire visible in the middle of panel (c), which was engineered to capacitively couple the two SETs, is situated below the oxide. In panel (b), the contact areas between the Au leads leading to the bonding pads and the Al/Cu double-layer structure in the middle are shown.

In the next step, a computer-designed pattern is transferred on the resist by an electron beam writer. In this work, the exposure was performed by a modified LEO Supra 40 scanning electron microscope. The acceleration voltage was 20 kV, and a typical dose for the finest structures was  $400 - 800 \mu\text{C}/\text{cm}^2$ . The exposed parts of the resist are removed chemically in a process called development. The chip was soaked in a 25% volume-by-volume (v/v) solution of methyl isobutyl ketone (MIBK) in isopropanol (IPA) for 15–30 s, after which it was rinsed in pure IPA and blow dried with nitrogen. After development, the resist contains wide cavities with exposed substrate at the bottom.

Thin-film metal deposition was performed by physical vapor deposition (PVD) using a focused electron beam to heat the evaporated metal. Evap-

oration of metal from an open crucible in a vacuum chamber causes the metal atoms to take a line-of-sight route from the source to the substrate. Film thickness (typically 15–50 nm) and deposition rate (3–20 Å/s) are controlled by a gauge based on the resonance frequency of a quartz crystal exposed to the metal vapor. Tunnel junctions and metal-to-metal contacts and were created *in situ* using multiple-angle evaporation, following the method by Dolan [55]. The tunnel barrier was created by oxidizing a freshly deposited aluminum film at an atmosphere of 1–20 mbar of pure O<sub>2</sub> for about 3–10 minutes.

In the final lift-off step, the remaining resist is removed along with the metal deposited on top of it, leaving behind only the metal pattern on the silicon substrate. Lift-off was performed by soaking the sample in acetone. The lift-off process was accelerated by heating the bath to about 70–80 °C, blowing with a syringe, and applying ultrasonic power.

For some samples, we realized large on-chip capacitances using a sample geometry where two vertically overlapping metal layers were galvanically insulated by an AlO<sub>x</sub> layer. The insulating layer was fabricated with the atomic layer deposition (ALD) process [92] in a commercial Beneq TFS-500 system. In early studies such as the one reported in Pub. IV, we used 400 nm of AlO<sub>x</sub> to ensure complete galvanic insulation. For Pub. IX, the layer thickness was reduced to 25 nm without any apparent leakage. From low-temperature *I–V* measurements on such a sample, we were able to infer a lower bound of 10<sup>12</sup> Ω for the leakage resistance through an overlap area of 25000 μm<sup>2</sup>.

The lithography and metal deposition process had to be performed twice to define the metal layers below and on top of the AlO<sub>x</sub> layer. To realize lateral alignment with a sub-1 μm accuracy, dedicated alignment marks were deposited on the sample chip, and all subsequent lithographic exposures were performed in relation to these marks. A relatively heavy element, such as gold, was used as the material of the alignment marks to ensure good visibility when scanned by an electron beam.

Figure 3.1 illustrates a sample that was fabricated by employing all the above techniques. The visible features in panel (a) are six electrical leads from the edges of the pattern to the center, a metallic ground plane that is located underneath the AlO<sub>x</sub> insulator, and four alignment marks at the corners. The material for all these structures is gold. In panel (b), the connections from the Au leads to a Cu/Al pattern forming the active part of the sample are shown. Alignment marks with a checkerboard pattern

can be faintly seen at the corners below a Cu/Al film that was incidentally deposited on top. Panel (c) shows the central part with two SETs that are capacitively coupled by a Cr wire. The fork-shaped tips of the two gate electrodes can be seen on the left and right edges. Typical of the Dolan process, two copies of the original resist pattern reside on the surface. The lower Al film (shifted to the left) has been oxidized before depositing the Cu film (shifted to the right). Tunnel junctions are formed at the regions where the two metals overlap.

### 3.2 Refrigeration

The experiments reported in this work call for cryogenic temperatures partly due to fundamental properties of the used materials, and partly due to technological limitations. To study superconducting thin films and tunnel junctions between superconductors and normal metals, the sample temperature must be below the critical temperature  $T_c$  of the superconductor. For strong single-electron charging effects, the energy scale of thermal fluctuations  $k_B T$  has to be small compared to charging energy  $E_c$ . Studies of electronic cooling or, in general, non-equilibrium phenomena benefit greatly from low temperatures due to the  $T^5$  dependence of the heat load from electron-phonon coupling. In addition, the magnitude of several error sources of electrical measurements is greatly diminished at low temperatures. In the context of this work, these include the Johnson-Nyquist noise from resistive elements, current leaks through semiconducting and insulating materials, and to some degree the  $1/f$ -type charge [93] and resistance [94] noise inherent to tunnel junction devices.

The necessary sub-100 mK temperatures can be reached in a  $^3\text{He}$ - $^4\text{He}$  dilution refrigerator. The cryogenic cooling power of a dilution refrigerator is based on a finite solubility of  $^3\text{He}$  in  $^4\text{He}$  even at absolute zero, and the mixing enthalpy of transferring  $^3\text{He}$  atoms from a pure phase into a dilute  $^3\text{He}$ - $^4\text{He}$  phase. A detailed description of the operating principle of a continuously-operating dilution refrigerator can be found in, e. g., Ref. [66]. The low-temperature measurements performed by the Author for this thesis were carried out in several plastic dilution refrigerators fabricated by the staff of the O.V. Lounasmaa Laboratory. The design is described in detail in Ref. [95] by Pekola and Kauppinen. The dilution unit of the refrigerator is fabricated from either Stycast or Torlon plastic, and is attached to a compact stainless steel frame. The dilution part

houses a spiral heat exchanger, containing approximately 2 m of Teflon (PTFE) tube, and the mixing chamber, to which the sample stage carrying the investigated samples is thermally linked via a sintered silver rod. In operation, the whole assembly is inserted into a dewar filled with liquid helium. The dilution part is situated in a vacuum chamber that can be filled with a small amount of helium gas for initial thermalization, and then evacuated by pumping to realize a sufficient thermal isolation from the relatively hot surroundings. The liquid Helium bath provides an efficient thermalization for all electrical connections running from room temperature to the vacuum chamber of the cryostat.

The temperature of the sample holder was monitored by measuring continuously the resistance of a ruthenium oxide resistor that was thermally anchored to it.  $\text{RuO}_2$  resistors have good thermal sensitivity in the operating temperatures of dilution refrigerators; the particular commercial resistors used in this work would display a resistance of about 1.3 k $\Omega$  at 4 K, and more than 40 k $\Omega$  at 50 mK. The temperature calibration curve for each resistor had been obtained in a dedicated cooldown, where the resistance reading and the temperature obtained from a primary Coulomb Blockade Thermometer (CBT) [96] were recorded throughout a temperature sweep.

### 3.3 Electrical wiring and shielding

The experimental part of this thesis consists of electrical characterization of tunnel junction devices. A common feature to all the studied devices is that their electrical terminals present a high impedance load: For tunnel junctions, the apparent resistance varies from a minimum of approximately  $R_T$  to an essentially infinite resistance occurring either in Coulomb blockade or in a NIS junction biased deep inside the superconducting gap. The smallest  $R_T$  for which we present data is 30 k $\Omega$ , with typical values being 100–1000 k $\Omega$ . Similarly, the gate electrodes of single-electron devices appear as purely capacitive loads.

The experiments were carried out in several different  $^3\text{He}$ – $^4\text{He}$  dilution refrigerators. For the majority of the experiments where only the dc characteristics of the devices were of interest, all device terminals would be connected to what we will refer to as dc wiring. Starting from 12 room temperature BNC connectors, the wiring first runs through the 4 K LHe bath as a loom of 6 twisted pairs of Manganin wire inside a metallic

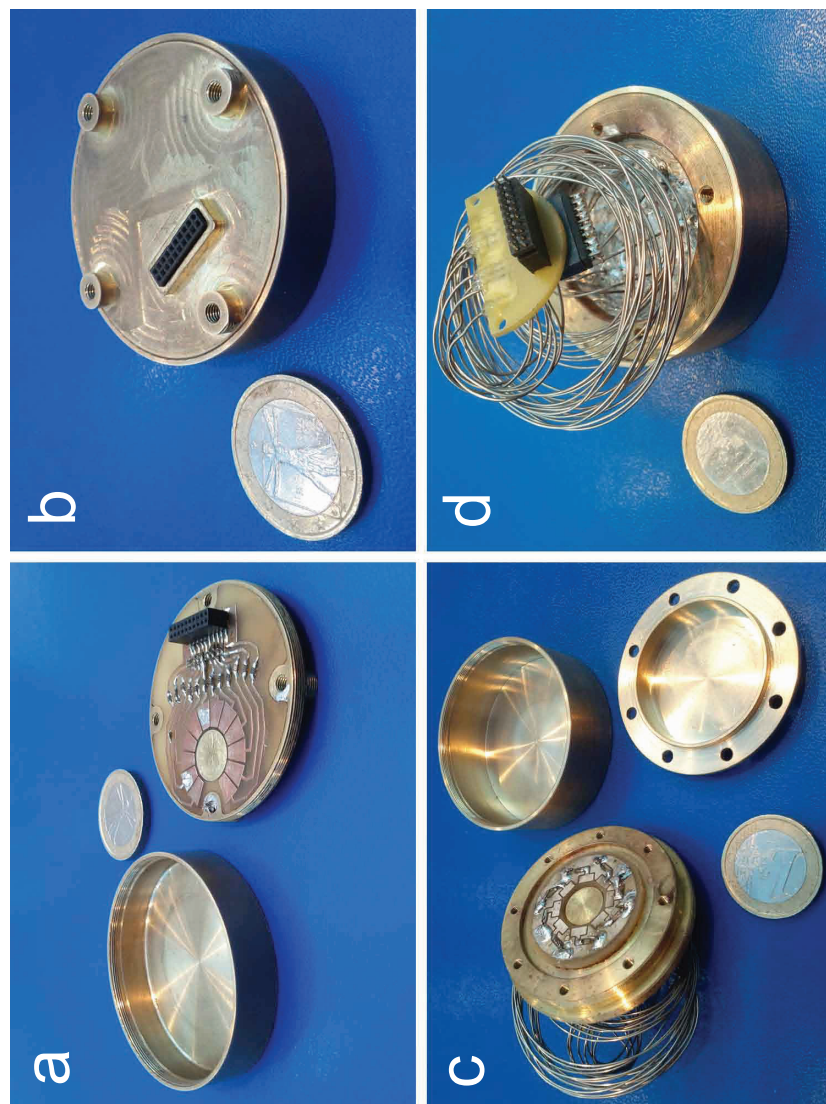


**Figure 3.2.** Models of sample stages used in the low-temperature experiments of this thesis. Diameter of the 1 euro coin provided for reference is 23 mm. Panels (a) and (b) show the baseline design that was used exclusively in Pubs. II, III and IV. Here, the detachable cap is attached by threads visible in panel (a), and the 20-pin dc connector is shielded by the protrusion visible in panel (b). Panels (c), (d) show the highly improved version used in Pubs. VII, IX and XI. In this design, the sample volume is shielded by two nested caps visible in panel (c), of which the inner one can be sealed with an indium seam and 8 M2.5 screws, and the outer one is similar to that in panel (a). In panel (d), it can be seen that the Thermocoax lines serving as high-frequency filters have been integrated into the design after the dc connector. The outer connector of Thermocoax cables is soldered to the body of the sample stage, eliminating microwave leaks.

sheath. At the 1 K pot stage, each of the 12 signal wires is connected to a 0.5 mm outer diameter Thermocoax cable with a length of 1.5–2 m (depending on the particular cryostat) that is thermalized at the sample holder at mixing chamber temperature. All 12 Thermocoax lines terminate to a commercial multi-pin connector. The total resistance per line from room temperature to sample holder connector is about  $200\ \Omega$  both at room temperature and during cryostat operation, sufficient to limit the electronic heat conduction between temperature stages to a level that does not hamper the cryostat operation. It should be noted that the cabling resistance of  $200\ \Omega$  is small compared to even the smallest sample resistances considered in this work, and hence can be neglected in the analysis.

The main drawback of this measurement scheme is slow response time of the room-temperature readout to changes in sample impedance: the effective rise time of an SET electrometer readout is limited by the  $RC$ -product of the sample resistance and the cabling capacitance in parallel. Zorin [97] gives a value of 490 pF/m for the capacitance per unit length for the used Thermocoax cable. Hence, the expected readout bandwidth for a  $100\ \text{k}\Omega$  electrometer measured through a 2 m cable is only 1.5 kHz.

For the experiments in Pubs. III and IV, 1–100 MHz drive signals were applied to the gate electrode of a SINIS turnstile device. In this case, the radio-frequency signal was brought to the sample stage by a coaxial cable transmission line with a  $50\ \Omega$  characteristic impedance, which was thermalized via thermally anchored attenuators at 4 K and at the 1 K pot stage.

In Pub. IV, subgap leakage of NIS devices was linked to microwave irradiation of the tunnel junctions at frequencies of 50 GHz and higher. A central idea in many subsequent studies, including those reported in Pubs. V–IX, was to study the microwave coupling in detail, and to seek technological solutions that help to reduce it. Based on earlier results [98], it was understood that at least a part, if not all, of the photon flux must come from the 4 K parts of the cryostat. There is no fundamental reason why this external flux could not be eliminated. We limited the scope of our study to dc properties only, so that propagation of rf signals in the MHz range did not need to be addressed in the design.

The high-frequency filtering properties of the employed Thermocoax cable are well known and studied in detail in Ref. [97]. Using the general formula given in the article, backed by measurements up to 18 GHz, one

obtains an attenuation of 200 dB/m at  $f = 20$  GHz and 300 dB/m at  $f = 50$  GHz. To see quantitatively that this amount of attenuation is entirely sufficient, consider the spectral density of voltage fluctuations of a  $100 \Omega$  resistor at 300 K:  $S_V(f) = 2k_BTR = 2 \times 10^{-18} \text{ V}^2/\text{Hz}$  for  $f \ll 6$  THz. To reduce this figure below the detection threshold of the most sensitive measurements charted in Fig. 4.4, about 100 dB of attenuation is needed.

In Fig. 3.2, panels (a) and (b) show the typical sample stage employed for dc measurements in the beginning of this work. Two weak spots were identified in this design, namely a leaky dc connector and an inadequately sealed shield cap. Panels (c) and (d) show a refined design where these issues have been addressed while adhering to the space and weight constraints of the plastic dilution refrigerators. Quantitative results on coupling of stray microwaves to tunnel junctions in various setups are presented in Sec. 4.2.

### 3.4 Electron counting with SETs

Many of the experiments reported in this thesis require the ability to detect individual electron tunneling events occurring in a mesoscopic system. There are two basic electrometer realizations that provide sufficient charge sensitivity for electron counting applications: the single-electron transistor (SET) [7, 8], and the quantum point contact (QPC) [99, 100, 101]. In this thesis, we have used exclusively SINIS-type SETs for electrometry. This allows the electrometer to be defined with the same fabrication process as the studied structures, which reduces significantly the complexity of the sample production and improves the yield. For purposes of electrometry, the SINIS SET performs similarly to its fully normal counterpart: The effective gate charge  $n_g$ , which controls the Coulombic energy gap of quasiparticle tunneling, is affected by the distribution of electric charge in the vicinity of the SET. In this manner, the 1–1000 pA quasiparticle current through the device can be modulated by fraction-of- $e$  changes in the effective gate charge.

Figure 3.3(a) illustrates the typical sample layout and electrical connections we have used in electron counting experiments, whereas Fig. 3.3(b) shows an idealized circuit diagram where the current transport through the SET is not explicitly considered. The electrometer is capacitively coupled to electrode R, which in turn is electrically connected only to electrode L via a low-transparency tunnel contact. Electrostatic coupling between

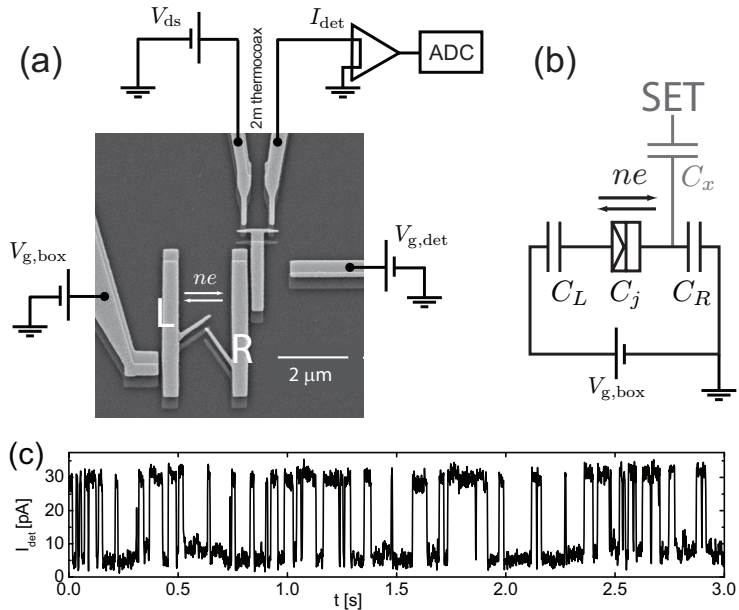


**Figure 3.3.** (a) Scanning electron micrograph of a sample consisting of a single-electron box (with electrodes L and R), and a capacitively coupled single-electron transistor. All control electronics is located at room temperature, and connected to the sample leads through dc wiring according to the illustration. The SET is held in voltage bias, and the instantaneous current is read out by a room-temperature transimpedance amplifier whose output is digitized by an A/D converter. (b) Simplified circuit diagram for description of the charge dynamics of the box. Capacitor  $C_j$  models the total mutual capacitance between the box electrodes L and R,  $C_x$  between the SET island and the electrode R,  $C_L$  between the left gate electrode and electrode L, and  $C_R$  stray and geometric capacitances of the electrode R. (c) Three-second experimental trace illustrating the detector current jumps in response to changes in the charge state of the box.

the electron box and the SET can be studied formally by writing down the relevant terms of the charging energy potential  $F_c$  defined in Sec. 2.2.2. We use variable  $n$  to denote the number of electrons transferred from electrode L to R, so that  $q_R = -q_L = ne$ , and variable  $m$  for the number of electrons on the SET island. For simplifying the algebra, we assume  $C_R$  to vanish and keep only the lowest order in the coupling capacitance  $C_x$ . We obtain

$$F_c = \frac{e^2}{2C_j} n^2 + \frac{e^2 C_x}{C_j C_{SET}} nm + \frac{e^2}{2C_{SET}} m^2, \quad (3.1)$$

where  $C_{SET}$  is the total capacitance of the SET island. From the cross-term of Eq. (3.1), we infer that a quasiparticle tunneling event in the box, changing  $n$  by  $\pm 1$ , also changes the effective gate charge of the SET electrometer by  $(C_x/C_j)e$ . In general, the parameter  $\kappa = C_x/C_{count}$ , where  $C_x$  is the coupling capacitance and  $C_{count}$  is the total capacitance of the count-

ing node, determines the fraction of the detected charge that is coupled to the electrometer, and should be maximized for best signal-to-noise ratio. Figure 3.3(c) shows an experimental time trace of the current through a voltage-biased SET that is sensing the charge state of a single-electron system near charge degeneracy.

The sample of Fig. 3.3(a) has two gate electrodes, whose potentials we refer to as  $V_{\text{det,g}}$  and  $V_{\text{box,g}}$ , respectively. They allow for independent tuning of the effective gate charge for the single-electron box and the electrometer. In an experiment performed on a sample like that of Fig. 3.3(a), one always observes some amount of capacitive cross-coupling between each gate electrode and islands other than the one it is intended to control. It is usually possible to determine the cross-coupling matrix elements by studying the system's response to one- or two-dimensional gate voltage sweeps, although this can be non-trivial to implement in practice for more complex single-electron devices. When the cross-coupling matrix is known, it is possible to determine a linear combination of gate voltage offsets that affects only the gate charge of the single-electron box, for example. This is useful when one wants to manipulate the charge state of the box while keeping the detector at a charge-sensitive operation point.

An overview of general aspects of electrometer performance in single-electron counting measurements has been presented in Ref. [90] by Pekola *et al.*<sup>1</sup> The three most important figures of merit that are discussed in the article in depth are charge sensitivity, back-action on the monitored system, and readout bandwidth. Charge sensitivity of an SET electrometer is typically expressed in units of  $e/\sqrt{\text{Hz}}$ . It is a measure of the noise level of the measurement setup as a whole referred to the "input" of the SET, i. e., the gate charge. For an SET device, a voltage fluctuation  $\delta V$  at the output of the readout chain can be related to a charge fluctuation  $\delta q$  through

$$\delta q = \frac{e}{C_g} \left( \frac{\partial V}{\partial V_g} \right)^{-1} \delta V, \quad (3.2)$$

where  $\frac{\partial V}{\partial V_g}$  is the measured sensitivity of the output to the applied gate voltage  $V_g$ , and  $C_g$  is the conversion factor between applied  $V_g$  and the SET gate charge  $en_g$ . The gate capacitance  $C_g$  can be determined accurately in the experiment from the measured gate modulation period  $V_{1e}$  of the electrometer according to  $C_g = \frac{e}{V_{1e}}$ .

In practice, the low-frequency noise spectrum is dominated by  $1/f$ -type

<sup>1</sup>The section on single-electron readout was composed mainly by the author of this thesis.

charge noise that is found in all metallic single-electron devices [102]. Zorin *et al.* [103] give the charge sensitivity of SET devices as  $10^{-3} - 10^{-4} e/\sqrt{\text{Hz}}$  at  $f = 10$  Hz. We find that the low-frequency charge noise spectrum of the electrometer data from Pub. IX is well fitted by  $2.8 \times 10^{-3} e/\sqrt{f}$ , in line with the literature values stated above. Throughout this thesis, the used electrometers were quite resistive (of the order of 1 M $\Omega$ ) and consequently the probing currents were small (about 30 pA in Pub. IX, for example). This choice reduces electronic back-action and substrate heating. The drawback is that the charge sensitivity at  $f > 100$  Hz set by amplifier noise was relatively poor, about  $3.8 \times 10^{-4} e/\sqrt{\text{Hz}}$ . For reference, the best charge sensitivity reported in the literature is  $0.9 \times 10^{-6} e/\sqrt{\text{Hz}}$ , obtained at  $f = 1.5$  MHz [104].

Any physical measurement perturbs the state of the system being probed. In the case of SET electrometry, the cross-term in Eq. (3.1), which is responsible for coupling the counting charge to the electrometer, also mediates an electronic back-action from the electrometer to the single-electron box. The probing current is transported through the SET by sequential single-electron tunneling events. Hence, the variable  $m$  of Eq. (3.1) fluctuates stochastically between two consecutive integer values. The rate parameter for these fluctuations is  $f_c = I_{\text{det}}/(2e)$ . The induced voltage noise over the junctions of the electron box can have sufficient spectrum content at high frequencies to cause photon-assisted tunneling events. We discuss this mechanism in Sec. 4.2 along with other sources of electromagnetic fluctuations.

The low-frequency part of detector back-action causes the effective gate charge of the box to fluctuate between  $e(n_{g,0} \pm \kappa'/2)$ , where  $n_{g,0}$  denotes the dc gate position without detector fluctuations, and  $\kappa' = C_x/C_{\text{SET}}$  is the charge coupling fraction from the detector island to the box. Turek *et al.* [105] analyze the effect of these fluctuations on dc gate modulation characteristics based on experimental data, and sequential tunneling theory that is equivalent to the one presented here. We have not considered explicitly this back-action mechanism in the analysis of the electron counting data that we present. For estimating the magnitude of the effect, we can assume the gate dependence of tunneling rates to be

$$\Gamma(n_g) = \Gamma_0 e^{2n_g E_c / (k_B T)},$$

where  $\Gamma_0$  is a constant the  $T$  is the temperature. Now, the tunneling rate

observed in the counting experiment is

$$\Gamma_{\text{obs}}(n_g) = \frac{1}{2} [\Gamma(n_g - \kappa'/2) + \Gamma(n_g + \kappa'/2)],$$

and the relative error is  $\cosh[\kappa' E_c / (k_B T)] - 1$ . Substituting  $\kappa' = 0.1$  and  $E_c / k_B = 0.6$  K corresponding to Pub. IX, we find the relative error to be 17% at an effective temperature of 0.1 K.

We also recognize the possibility of phonon-mediated back-action. The Joule heating power  $P = \langle IV \rangle$  dissipated at the detector junctions can cause the substrate to be locally heated. Since the counting node has to be placed physically close to the detector to realize sufficient charge coupling, it is plausible for the phonons of the counting node to be heated as well, which would lead to an elevated electron temperature and increased tunneling rates. A calculation presented in Ref. [90] based on a model of the thermal conductivity of SiO from Ref. [106] shows this to be a potential issue in some electron counting experiments. However, in the case of Pub. IX, we were able to verify the thermalization of the electron system in the counting node down to 50 mK [see Fig. 3(a) of the journal article], ruling out this back-action mechanism.

Finally, we consider the effect of finite detector bandwidth on the extracted tunneling rates. In this thesis, the electrometer read-out was performed with a room-temperature current amplifier through a wiring consisting of sections of twisted-pair and Thermocoax cable. Long cabling combined with the high source impedance of the SET electrometer results in an available read-out bandwidth of about 1–10 kHz, as discussed in Sec. 3.3. Although this bandwidth is sufficient for studying sub-gap quasiparticle tunneling in opaque NIS junctions, the ability to estimate and – to some degree – correct the detector bandwidth bias in experimental data is useful. We make use of the methodology and theory presented by Naaman and Aumentado in Ref. [107]. The theoretical analysis concerns a time-domain measurement of the state of a two-level RTN fluctuator with transition rates  $\Gamma_A$  and  $\Gamma_B$ . Transitions between the two states are determined by threshold detection at the midpoint between the signal levels corresponding to states  $A$  and  $B$ , which is what we have used consequently in the analysis of the experimental data. Finite response time of the detector is modeled by making the process of changing the output state of the detector Markovian with a rate parameter  $\Gamma_{\text{det}}$ .

When analyzing the experimental data for Pub. V, we obtained estimates for the rate parameters  $\Gamma_{A,B}$  from the inverse of the observed mean

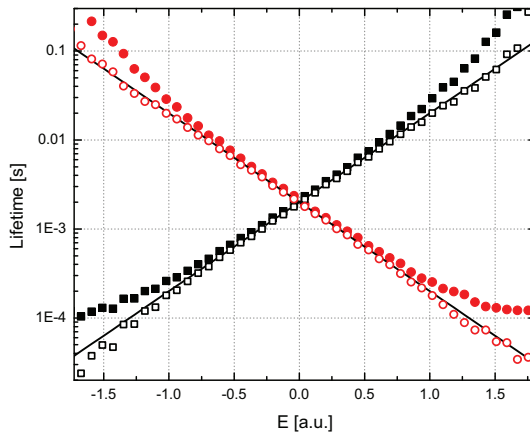


**Figure 3.4.** Effect of finite detector bandwidth on the observed state lifetimes (filled symbols), and the bandwidth-corrected lifetime estimates (open symbols). We used a set of computer-generated RTN traces sampled at  $10^5$  Hz to simulate observations of a two-level system. The true dwell times of the two states are given by the formula  $\tau_{A(B)} = (500 \text{ Hz})^{-1} 10^{\pm E}$ , where  $E$  is a dimensionless variable mimicking the gate charge offset encountered in actual single-electron experiments. Gaussian white noise with an r.m.s amplitude of 0.25 relative to the state separation was added to simulate experimental charge noise. Prior to threshold detection, the signal was low-pass filtered with a 4th order low-pass filter having a cut-off frequency of 5 kHz. In the bandwidth-correction formulas, the detector response time parameter  $\Gamma_{\text{det}}$  was set to 12.5 kHz in order to maximize the parameter range where accurate lifetime estimates are obtained.

dwell times,  $\Gamma_{A,B}^* = 1/\langle\tau_{B,A}^*\rangle$ . According to the theory of Ref. [107], these rate estimates are related to the true rate parameters as

$$\Gamma_A^* = \frac{\Gamma_A \Gamma_{\text{det}}}{\Gamma_A + \Gamma_B + \Gamma_{\text{det}}}, \quad \Gamma_B^* = \frac{\Gamma_B \Gamma_{\text{det}}}{\Gamma_A + \Gamma_B + \Gamma_{\text{det}}}. \quad (3.3)$$

Solving  $\Gamma_{A,B}$  from the above pair of equations yields an expression for the bandwidth-corrected rates. Due to the phenomenological modeling of the detector response,  $\Gamma_{\text{det}}$  for a particular readout setup is to be considered a fit parameter, which nevertheless should be related to the physical rise-time of the detector readout. Following Ref. [107], parameter  $\Gamma_{\text{det}}$  can be fitted from the full distribution of observed dwell times. Detector bandwidth was explicitly accounted for in the published data of Pubs. IX and XI.

In Fig. 3.4, we show results from computer simulations that illustrate the bandwidth-correction procedure in practice. We generated a set of two-level RTN signals with different rate parameters. We added Gaussian white noise that was similar in magnitude to the charge noise typically observed in the experiments, and low-pass filtered the signal. The artificial

detector traces were then processed with the same code that was used to count the tunneling events in the experimental data. We observe that a combination of a high and a low rate parameter, which occurs in electron box experiments away from the degeneracy, causes a significant bias in the uncorrected life-time estimates. Due to the fact that the fastest excursions to the short-lived state are missed, both transition rate parameters are severely underestimated. Based on the simulation results, we conclude that the bandwidth-corrected transition rates from electron counting experiments are usable up to about twice the intrinsic bandwidth of the readout even in the presence of moderate charge noise.

## 4. Results on NIS devices

### 4.1 Gate control of electronic refrigeration

In this section, we present an investigation of the thermal effects in a SINIS-type SET. This structure provides enables a study of the interplay between charging effects and heat transport at mesoscopic scale. In general, to achieve lowest possible electron temperatures in a SINIS cooler, the volume of the island should be minimized in order to reduce the heat load from electron-phonon coupling. It is precisely at low temperatures and in sub-micron structures where charging energy effects manifest themselves. Charging energy effects can be expected to have an influence in the design and analysis of electronic coolers aimed at sub-100 mK temperatures.

Our analysis shows that a Coulomb-blockaded SINIS functions as a gate-controlled single-electron refrigerator, i. e., a heat transistor. We demonstrate experimentally gate modulation of the heat flux out of the normal metal island by more than a factor of three. In addition to cooling properties, the structure displays unique features in the  $I$ - $V$  curves of temperature probe junctions originating from changes in the charge number distribution of the island. The experimental findings are successfully reproduced by an application of the theoretical methods presented in earlier chapters. These results have been reported in Pub. II.

In Fig. 4.1(a), we illustrate a scanning electron micrograph of one of the measured heat transistor samples along with a sketch of the measurement setup. The central normal metal island is a copper block with lateral dimensions  $180 \text{ nm} \times 2300 \text{ nm}$  determined from the SEM micrograph, and thickness of  $20 \pm 3 \text{ nm}$  based on AFM measurements. The superconducting parts of the sample are thin-film aluminum with a similar thickness

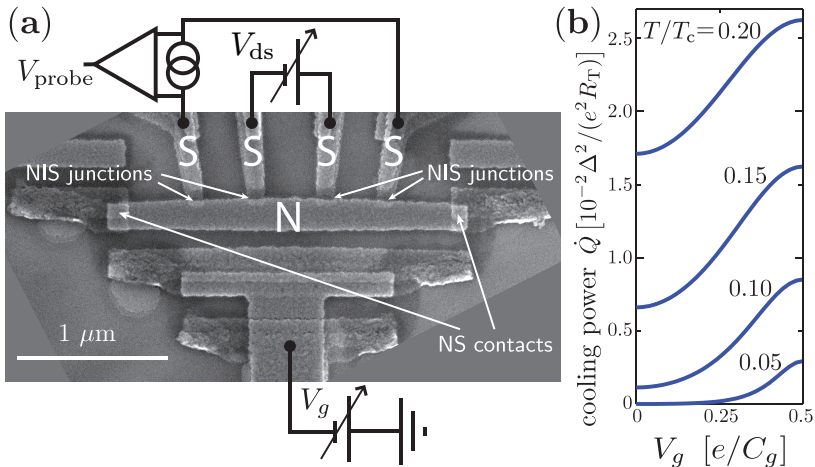


**Figure 4.1.** (a) Scanning electron micrograph of the heat transistor sample, illustrating also the measurement connections and denomination of voltages. (b) Theoretical heat flow from the normal metal island at the optimal bias point  $V_{\text{ds}} \simeq 2(\Delta - 0.66k_{\text{B}}T_{\text{N}})/e$  at different temperatures as a function of the gate voltage. The figure appears in Pub. II as Fig. 1.

thickness as the island. For the experiment, four aluminum-oxide tunnel junctions with approximate dimensions  $120 \text{ nm} \times 40 \text{ nm}$  and specific room-temperature resistance of  $0.6 \text{ k}\Omega \mu\text{m}^2$  were fabricated on the island. The two inner junctions with  $110 \text{ k}\Omega$  resistance were used as a voltage-biased cooler pair. Consistent with the transistor analogy, we denote the bias voltage over the cooler junctions  $V_{\text{ds}}$ . The outer junctions with a resistance of approximately  $150 \text{ k}\Omega$  were current-biased at picoampere-level, enabling accurate thermometry of the island electron temperature by exploiting the temperature sensitivity of  $V_{\text{probe}}$  in the 100-500 mK range. The gate electrode was driven by a variable voltage source. Figure 4.1(b) illustrates the expected normalized cooling power of the heat transistor, displaying the modulation of heat flow with gate voltage at different operating temperatures. For simplicity, effect of the temperature probes has been neglected in this figure.

For a direct verification of the Coulomb blockade effects, we also fabricated and measured a reference sample with similar geometry and junction parameters, except for large capacitor pads attached to the island with NS contacts, suppressing the charging energy but ideally blocking the electronic heat flow by means of Andreev reflection [108]. In the actual heat transistor sample, we preserved only small, 500 nm long superconducting protrusions in order to maintain the same topology with

a minimal suppression of the charging energy. Measurements performed on the reference sample mimic those performed on the heat transistor, and consequently the obtained data could also be analyzed in an almost identical manner. However, since the reference sample as such does not constitute a test bed for any new physical phenomena, we do not present a detailed analysis of it.

An intuitive picture of the gate dependence of the cooling power can be obtained by analyzing the behavior of a SINIS cooler in terms of typical charge state trajectories. With the gate tuned to charge degeneracy, the device operates similarly to a regular SINIS whose electric and heat currents have been scaled by  $1/2$ . We can therefore apply the analytic NIS junction results from Sec. 2.3.2: Taking into account the series connection of two junctions, the optimal cooler bias voltage is  $V_{\text{ds,opt}} = 2(\Delta - 0.66k_{\text{B}}T)/e$ . The maximum cooling power is

$$\dot{Q}^{\text{N}}(\text{open}) \simeq -0.3 \frac{\Delta^{1/2}(k_{\text{B}}T)^{3/2}}{e^2 R_{\parallel}}, \quad (4.1)$$

where  $R_{\parallel}$  is the parallel resistance of the two cooler junctions.

In the case of full Coulomb blockade, i. e., the normalized gate charge  $n_g$  equal to an integer, electric and heat currents through the device are strongly suppressed. Most of the time, the system lies in the minimum energy charge state  $n = n_g$  with excursions into  $n = n_g \pm 1$  occurring at a rate  $\Gamma^{\uparrow} = \Gamma(eV_{\text{ds}}/2 - E_c)$ . The relaxation rate back to  $n = n_g$  is given by  $\Gamma^{\downarrow} = \Gamma(eV_{\text{ds}}/2 + E_c)$ , and is much larger than  $\Gamma^{\uparrow}$  for the bias voltages  $V_{\text{ds}} \approx 2\Delta$  where cooling is observed. The total heat deposited into the normal electrode by these two quasiparticle tunneling events can be written in terms of the  $\langle Q(E) \rangle$  function defined in Eq. (2.68) as

$$\langle \dot{Q}^{\text{N}}(0 \rightarrow 1 \rightarrow 0) \rangle = \langle \dot{Q}^{\text{N}}(eV_{\text{ds}}/2 - E_c) \rangle + \langle \dot{Q}^{\text{N}}(eV_{\text{ds}}/2 + E_c) \rangle. \quad (4.2)$$

To study the strong Coulomb blockade limit, we take  $eV_{\text{ds}} = 2\Delta$  and employ the approximation  $\langle \dot{Q}^{\text{N}}(E) \rangle \approx E - \Delta$  (valid for  $E \ll \Delta$ ) to the first term, and  $\langle \dot{Q}^{\text{N}}(E) \rangle \approx (E - \Delta)/2$  (valid for  $E \gg \Delta$ ) to the second term. The average heat extracted from the normal metal per tunneling electron is thus  $E_c/4$  as opposed to roughly  $k_{\text{B}}T$  in the gate open case. For the on-off-ratio of cooling power, we obtain

$$\dot{Q}^{\text{N}}(\text{closed})/\dot{Q}^{\text{N}}(\text{open}) \simeq \frac{E_c}{4k_{\text{B}}T} \times \frac{4\Gamma^{\uparrow}}{\Gamma(eV_{\text{ds}}/2)} \simeq \frac{E_c}{k_{\text{B}}T} e^{-E_c/k_{\text{B}}T}. \quad (4.3)$$

Above, the factor  $4\Gamma^{\uparrow}$  results from the fact that there are two possible cycles ( $n_g \rightarrow n_g \pm 1 \rightarrow n_g$ ) each involving a transfer of two electrons. Although the total cooling power is suppressed due to Coulomb blockade,

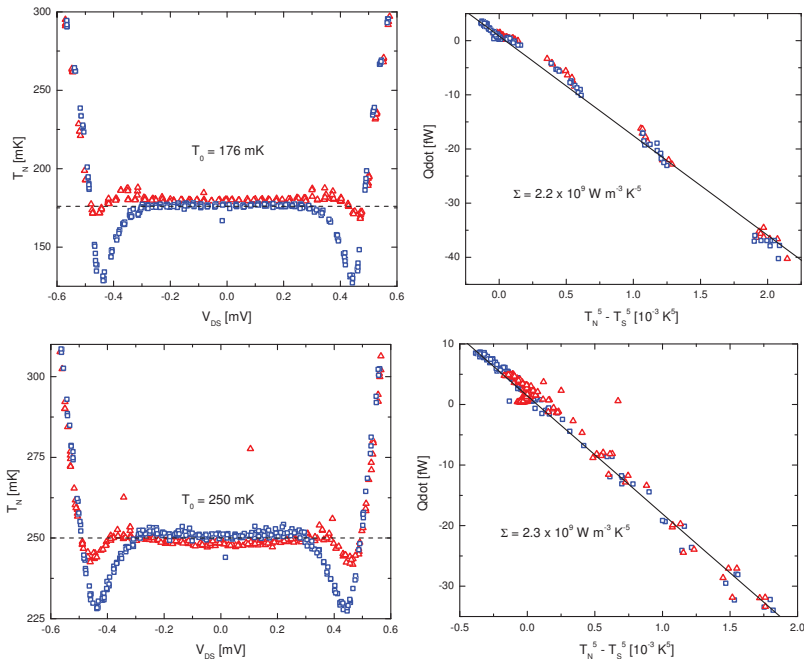


**Figure 4.2.** Left column: Electron temperatures extracted from the data acquired at bath temperatures 176 mK, 214 mK and 250 mK with the gate in open ( $n_g = 1/2$ , blue squares) and closed ( $n_g = 0$ , red triangles) position. Right column: Theoretical cooling power vs.  $T_N^5 - T_S^5$  for each data point on the left, and a line fit. According to Eq. (4.5), the slope is given by  $-\Sigma\mathcal{V}$ .

the efficiency of the device improves by a factor  $E_c/(4k_B T)$ . This could be a beneficial trade-off in realistic coolers, where disposing of the heat deposited into the superconducting leads can be the limiting factor of device performance. However, a similar improvement in performance can be realized in a regular SINIS cooler by driving it with a smaller bias voltage.

The device geometry shown in Fig. 4.1(a) with separate junction pairs for cooling and thermometry is standard for NIS coolers. The significant charging energy of the device makes extracting the island temperature from the observed  $V_{\text{probe}}$  non-trivial. First,  $I_{\text{probe}}$  has an explicit gate dependence. Secondly, the transconductance  $\partial I_{\text{probe}}/\partial V_{\text{ds}}$  does not vanish at fixed island temperature. Two years after Pub. II, Koppinen *et al.* published a more extensive study of NIS thermometry in Coulomb blockaded structures [64]. For a quantitative analysis of the measured data, we constructed a full Master equation based model of the electric and heat transport in the device in the manner described in Sec. 5.1. In a high-

level language, the computational model can be described as

$$\begin{bmatrix} I_{\text{probe}} \\ \dot{Q}^{\text{N}} \end{bmatrix} = f(V_{\text{ds}}, V_{\text{probe}}, n_g, T_{\text{N}}, T_{\text{S}}). \quad (4.4)$$

In the experiment, the variables  $V_{\text{ds}}$ ,  $n_g$ ,  $I_{\text{probe}}$  are controlled by room-temperature voltage and current sources as shown in Fig. 4.1(a). Furthermore, we measure  $V_{\text{probe}}$ , and assume  $T_{\text{S}}$  to coincide with the bath temperature  $T_0$ . Inserting the known values into Eq. (4.4), we can solve for  $T_{\text{N}}$  and also infer  $\dot{Q}^{\text{N}}$ . As a consistency check, we can insert the values obtained in this manner to a heat balance equation. Assuming the standard electron-phonon heat flow of Eq. 2.73 and equilibrium phonons, we have

$$\dot{Q}^{\text{N}} = \Sigma \mathcal{V} (T_{\text{N}}^5 - T_0^5). \quad (4.5)$$

Full analysis of the experimental data is presented in Pub. II, and it is found to be in excellent agreement with the model described above. In Fig. 4.2, we present additional experimental data sets of  $T_{\text{N}}$  and  $\dot{Q}^{\text{N}}$  versus  $V_{\text{ds}}$  that were not included in the journal article due to space constraints. When treating the electron-phonon coupling constant  $\Sigma$  as a fitting parameter, we obtain values  $2.2 - 2.3 \times 10^9$  (in units of  $\text{Wm}^{-3}\text{K}^{-5}$ ) that are close to the literature value of  $2 \times 10^9$  reported for copper. This is an important proof of the quantitative validity of the model.

The work on heat transistor can be considered to be a partial experimental verification of the essential building blocks of the theoretical proposal of Pub. I. In that proposal, we studied electrical refrigeration in a NIS-type single-electron box that is subjected to a radio-frequency gate drive. In contrast to traditional realizations of electrical refrigeration employing dc bias voltages, in the proposed scheme, the heat-extracting quasiparticle tunneling events are actuated by the capacitively coupled gate that drives the box between different charge states.

The operation conditions can be derived based on the approximative expressions for the quasiparticle tunneling rate [Eq. (2.62)] and the amount of heat extracted by a single tunneling event [Eq. (2.68)]. The appropriate scale for the drive frequencies is given by the prefactor of Eq. (2.62), i. e., we require

$$f \lesssim \frac{\sqrt{\pi k_{\text{B}} T \Delta / 2}}{e^2 R_T}. \quad (4.6)$$

At these drive frequencies, the tunneling events take place when the change in the energy of the tunneling quasiparticle is approximately  $\Delta$ , in which case an amount of heat proportional to  $k_{\text{B}}T$  is extracted. Hence,

we can write suggestively the total cooling power of the rf single-electron refrigerator as

$$\dot{Q}^N = -\alpha f k_B T, \quad (4.7)$$

where the prefactor  $\alpha$  is expected to be of the order unity in the optimal range of operation parameters. In Pub. I, a quantitative analysis of the expected cooler performance is presented using Monte Carlo and master equation based simulation methods. An experimental demonstration of these ideas was presented later by Kafanov *et al.* [109]. Instead of the single-electron box topology of the original proposition, the experiment was performed with a single-electron transistor in order to allow *in situ* electron thermometry based on the electric current through the device. The authors used a low dc bias voltage of  $0.25\Delta/e$  over the SET to create a small probe current that was sensitive to the temperature of the normal metal island.

## 4.2 Effect of the electromagnetic environment

An intuitive idea of the behavior of devices based on single-electron tunneling can often be obtained by considering only the energetics of the system. Accounting for bias voltages and changes in the electrostatic charging energy, one can sort the possible tunneling processes into energetically favorable and unfavorable ones. Superconducting hybrid structures can be treated in this manner as well by including an energy cost of  $\Delta$  for each quasiparticle excitation created in a superconducting electrode. For quantitative results, one needs to consider the numerical values of the rate parameters  $\Gamma$  of various processes. From general thermodynamical arguments, one expects a detailed balance equation of the form

$$\Gamma(-\Delta E) = e^{-\Delta E/k_B T} \Gamma(\Delta E), \quad (4.8)$$

where  $\Delta E$  is the change in energy in the tunneling event, to hold in thermal equilibrium. From Eq. (4.8), one sees that energetically unfavorable ( $\Delta E < 0$ ) processes have a finite probability to occur, and that probability will go to zero in the limit  $T \rightarrow 0$ . A second observation is that a single-electron device cooled down to millikelvin temperatures should exhibit an exponential dependence of the type  $\exp(eV_b/k_B T)$  for charge tunneling rates versus voltage changes, enabling very sensitive voltage amplifiers and tunneling spectroscopy with good energy resolution. Finally, this reasoning can be used to obtain a temperature dependence of  $\exp(-E_c/k_B T)$

for the error probability of single-electron pumps and turnstiles, where  $E_c$  is the charging energy of the device. Substituting  $E_c/k_B = 4$  K and  $T = 50$  mK, routinely reachable values for samples defined with electron-beam lithography and cooled in a dilution refrigerator as described in Sec. 3, one obtains a remarkably low probability of  $1.5 \times 10^{-35}$ . Such numbers are not, however, observed in the experiments, for which we will discuss several mechanism in this and the following chapters.

It is often non-trivial to realize the full thermal equilibrium in the sense described above. One can also take the viewpoint that improving the performance of single-electron devices is akin to improving the thermalization of the device toward the sample holder temperature. One possible mechanism for Eq. (4.8) to fail is interaction with the electromagnetic environment. This interaction is described by the  $P(E)$  theory [see Sec. 2.2.1], and affects the tunneling processes by giving the tunneling quasiparticle a finite probability to exchange energy with the environment. It is helpful to make a distinction between two kinds of environmental couplings, which we will call *strong* and *weak*.

In the case of strong coupling, the real part of the impedance  $Z_t(\omega)$  seen from the junction at some angular frequency  $\omega$  is comparable to the resistance quantum  $R_K = 25.8$  k $\Omega$  or larger. To achieve strong coupling in the frequency range interesting for single-electron devices, it is necessary to fabricate the resistive element lithographically close to the junction in order to prevent capacitive shunting. For the operation of single-electron devices, a high impedance on-chip environment is usually beneficial for several reasons: It creates a local  $RC$  filter that cuts the coupling of high-frequency noise to the junction, reduces the rates for higher-order events causing leakage, and provides an additional charging energy barrier for tunneling electrons without the need for a gate electrode. An on-chip resistive environment has been implemented in many earlier studies. In this thesis, such a design was employed in the devices measured in Pubs. VI and VII. Although the effect of the on-chip resistor was not thoroughly investigated, it was included in the environment used for theoretical modeling as described in Sec. 2.2.1 and Pub. VI, and the observed charge trapping times observed in these structures were extremely long.

For a weakly coupled environment, the  $P(E)$  function can be evaluated for large values of  $E$  from the voltage fluctuation spectrum using Eq. (2.27), or from the environmental impedance  $Z_t(\omega)$  and environment temperature  $T_{\text{env}}$  using Eq. (2.30). The resulting  $P(E)$  function has most

of its probability mass centered at  $E = 0$ , but the long tail for negative  $E$  extending up to  $k_B T_{\text{env}}$  is potentially harmful for device performance: A "hot" environmental fluctuator, i. e., one with  $T_{\text{env}} \gtrsim E_c/k_B$  for single-electron devices or  $T_{\text{env}} \gtrsim \Delta/k_B$  for an NIS device, enables energetically unfavorable processes to occur via photon absorption.

Of the experiments included in this thesis, the one reported in Pub. IV is the first one where the hot environment model was explicitly employed. There, it was shown that sub-gap leakage currents of NIS junctions can be attributed to photon assisted tunneling. The environment was modeled as an  $RC$  circuit at a temperature of 4 K corresponding to the temperature of the liquid helium bath and the vacuum chamber surrounding the dilution unit of the cryostat. The main theoretical result of the study was that the  $I$ - $V$  characteristic in such an environment is identical to that produced by a sub-gap quasiparticle density of states in the superconductor corresponding to Dynes parameter

$$\gamma = 2\pi R/R_K \times k_B T_{\text{env}}/\Delta. \quad (4.9)$$

Furthermore, we showed that the sub-gap leakage could be reduced by an order of magnitude by fabricating the junctions on a ground plane acting as a capacitive shunt. A similar improvement in the performance of single-electron turnstile devices containing a capacitive shunt was also observed.

In Pub. V, the on-chip capacitive shunting technique was used to shield a single-electron box. The single-electron box is not galvanically connected to electrical leads, and thus cannot be subjected to a usual  $I$ - $V$  measurement. Instead, we probed the charge state of the box as a function of external gate voltage using a capacitively coupled SET electrometer. From the single-electron box measurements, the influence of the electrical environment could be assessed in two ways: First, by measuring the width of the Coulomb blockade steps in gate modulation curves, the effective temperature of the box could be determined. As reported in the article, for the unshunted sample, a minimum width was observed around 200 mK, after which the Coulomb step started to widen as a function of temperature. This can be understood through the transition rates plotted in Fig. 4.3(a): At low enough temperatures, the ratio  $\Gamma(E)/\Gamma(-E)$  determining the shape of the Coulomb step does not measure the electronic temperature of the box electrodes, but is instead set by the decay of the tail of the  $P(E)$  function for negative energies. For the shielded sample, no clear saturation of the step width was observed at least for  $T > 80$  mK.

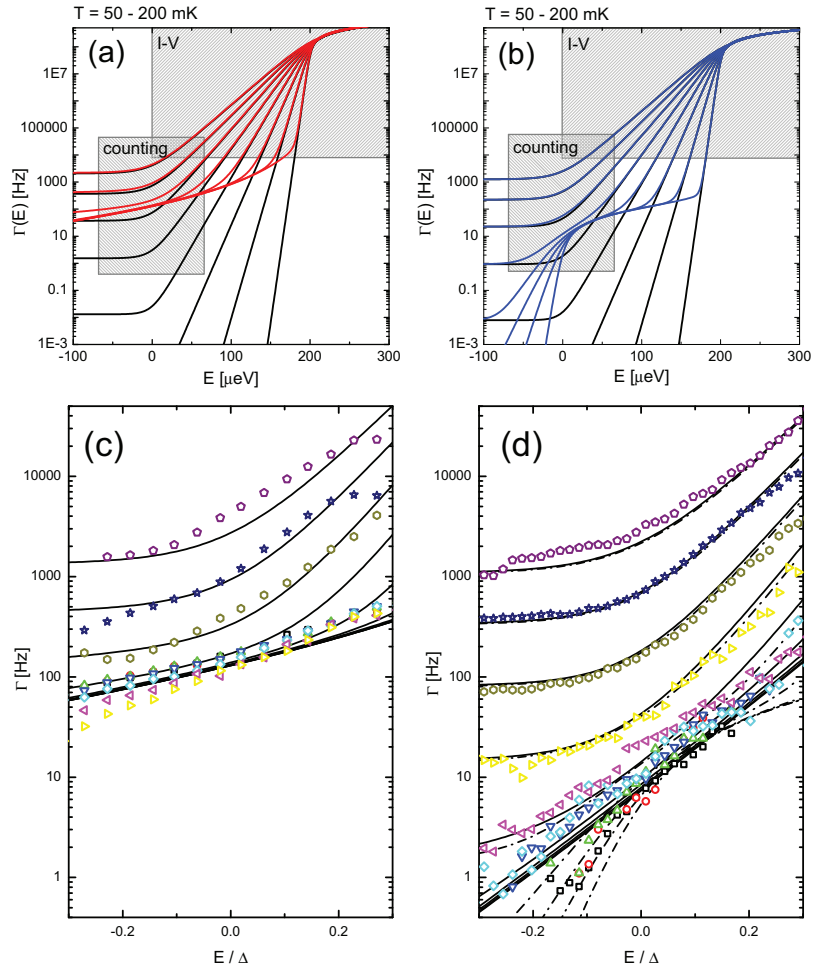


**Figure 4.3.** (a), (b) Theoretical single-electron tunneling rates for NIS junctions using sample parameters from Pub. V [(a)  $\Delta = 200 \mu\text{eV}$ ,  $R_T = 2.0 \text{ M}\Omega$  (sample "R1"); (b)  $\Delta = 200 \mu\text{eV}$ ,  $R_T = 3.3 \text{ M}\Omega$  (sample "G1")]. Black curves are thermal equilibrium rates. In panel (a), red curves incorporate the effect of a resistive  $RC$  environment 4 K. In panel (b), blue curves include sub-gap states in the superconductor corresponding to Dynes parameter  $\gamma = 5 \times 10^{-7}$ . Shaded boxes indicate the range that would be accessible in a typical galvanic  $I$ - $V$  measurement, and the range that was studied in the performed counting measurement. (c), (d) Re-analyzed tunneling rates from the data of Pub. V for sample R1 and G1, respectively, incorporating detector bandwidth correction (colored markers), and the theoretical predictions including the effect of a best-fit  $RC$  environment (solid black lines). In panel (d), dash-dotted lines give the theoretical curves corresponding to Dynes parameter  $\gamma = 5 \times 10^{-7}$  as in panel (b).

Secondly, we detected the electron tunneling events in real time and determined the tunneling rates  $\Gamma(E)$  in the energy range  $-60 \mu\text{eV} \dots 60 \mu\text{eV}$  at temperatures up to 200 mK. As illustrated by the shaded regions in Figs. 4.3(a) and (b),  $I$ - $V$  and counting measurements enable the probing of complementary bias voltage and tunneling rate ranges. The measured tunneling rates are presented in Figs. 4.3(c) and (d), corrected for finite detector bandwidth. The saturation background set by environmental noise is evident in the data for the unshunted sample, whereas the lowest rates observed for the shunted sample are more than an order of magnitude smaller. Nevertheless, the lowest temperature rates differ from the thermal equilibrium curves also for the shunted sample. The rates could be plausibly explained by environmental coupling or by a small density of sub-gap states in the superconductor. As is evident from comparing Figs. 4.3(a) and (b), the predicted tunneling rates for the  $P(E)$  and Dynes case differ for negative  $E$ , but the quality of the data for the shunted sample is not sufficient to differentiate between them. The main conclusion of this measurement is nevertheless clear: the low-temperature dynamics of the unshunted sample was set by interaction with a hot electromagnetic environment, and the isolation could be significantly improved by an on-chip capacitive shunt.

The conclusions made in Pub. V were later confirmed by the results of Pubs. IX, VI and VII. In these studies, efforts were made to improve the decoupling from environment through sample and sample stage design. In Fig. 4.4, we have plotted the power spectra of voltage fluctuations inferred from all the quasiparticle transport measurements performed for this thesis. Different device topologies and measurement schemes probe the tunneling rates at different energy ranges:  $I$ - $V$  measurements are best suited for determining the relatively large tunneling rates  $\Gamma(E)$  realized when  $E$  is close to the gap parameter  $\Delta$  and offer essentially zero visibility in the range  $E < 0$ . Electron counting measurements on single-electron boxes and transistors can be used to map the region around  $E = 0$ . The measurable  $E$  range is in practice limited by the requirement that both rates  $\Gamma(E)$  and  $\Gamma(-E)$  are within the detector bandwidth. Finally, electron traps can be used to probe the deep negative  $E$  range. In Pub. VII, the trapping times were of the order of several hours, in which case obtaining proper statistics on the escape processes becomes challenging due to long measurement times needed.

In the preceding discussion, the origin of the high-frequency photons

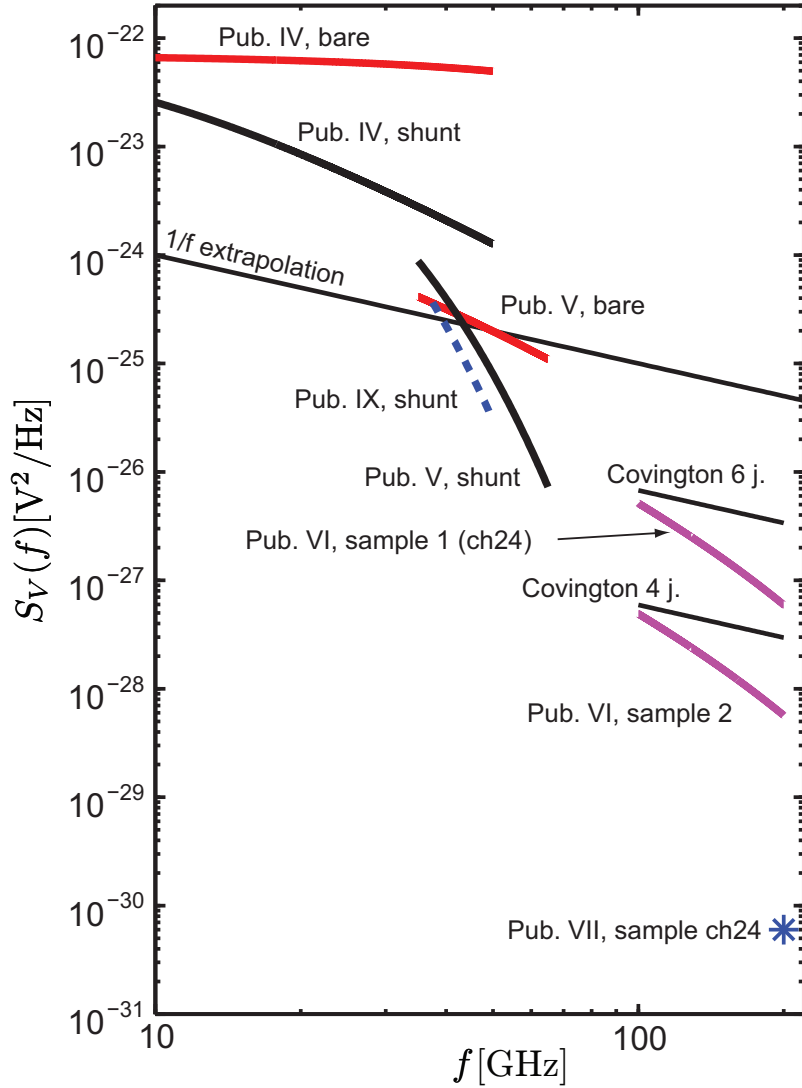


**Figure 4.4.** Noise spectra in the 10 – 200 GHz range extracted from various experiments on single-electron devices. The curve sections for which no measurement with a smaller noise power is available should be treated as upper bounds. "Shunted" devices were fabricated on a ground plane, whereas "bare" devices resided on a SiO/Si substrate. The sample stage used in Pubs. IV and V was the baseline design, whereas in Pub. IX the light-tight design was used [see Sec. 3.3]. Measurements of Pub. IX were repeated in an independent light-tight setup at MIKES designed by A. Kemppinen with identical results. For Pub. VI, we used an improved version of the baseline design with two nested shield caps, but a leaky dc connector. For Pub. VII, the marker above corresponds to the longest hold times which were obtained in the MIKES setup. The hold times observed in the light-tight design described in Sec. 3.3 were about one order of magnitude shorter. For reference, we have plotted also the three spectra given by Covington *et al.* in Ref. [110]: An extrapolation of  $1/f$  charge noise data from Ref. [103], and best fits to the data obtained from 4 and 6-junction electron pumps, respectively.

has been taken to reside outside the sample stage. This hypothesis can be verified in practice if the measured tunneling rates are found to diminish when the sample stage shielding or filtering is improved. The outstanding question is then what is the source of the weakest observed voltage fluctuations:  $S_V(f) = 3 \times 10^{-26} \text{ V}^2/\text{Hz}$  at 50 GHz, and  $6 \times 10^{-31} \text{ V}^2/\text{Hz}$  at 200 GHz. It must be said, however, that these numbers are mere upper bounds extracted from the observed tunneling rate data: it is possible that the true voltage fluctuations are even weaker still, and the observed tunneling events are caused by a process other than PAT. Nevertheless, it is expected that when the microwave shielding is sufficiently improved, sources from inside the sample stage begin to dominate. A simple thermodynamical argument tells that any material in thermal equilibrium with the sample stage cannot emit a significant quantity of photons at frequencies above  $f_{th} = k_B T/h$ . At  $T = 50 \text{ mK}$ ,  $f_{th} = 1 \text{ GHz}$ , and we conclude that the possible on-chip microwave sources must be in inequilibrium. In Ref. [110], Covington *et al.* proposed that the  $1/f$ -type charge noise originating from glassy sample chip materials extends up to microwave frequencies. However, the upper bound obtained from the data of Pub. VII at 200 GHz is 50 dB below the expected level for charge noise stated in Ref. [110], calling for a re-evaluation of the argument.

In counting experiments, the high-frequency component of the back-action of the electrometer is a possible source of voltage fluctuations. However, being externally tunable, the severity of the back-action is easily checked in the experiments by measuring the dependence (if any) of the tunneling rates on the operation point of the detector. To summarize the findings, no detectable back-action was observed in Pubs. VI and VII. In Pub. V, for the unshunted sample, detector back-action was negligible compared to the external microwave noise, whereas for the shunted sample, the back-action could be observed but was not quantitatively studied. In Pub. IX, a weak linear dependence of the tunneling rates on the detector current was found. In the case of Pub. IX, the two SETs were placed relatively far from each other (about  $5 \mu\text{m}$ ) and the capacitive coupling between the SET islands was realized with a resistive Cr wire. We were expecting that the resistive wire would exhibit inherent low-pass filtering properties, which would result in diminished back-action. We have not assessed this hypothesis quantitatively in light of the measurement results. In a recent work by Lotkhov and Zorin [111], the authors studied photon-assisted escape processes from an electron trap irradiated by pho-

tons originating from a SINIS-type SET. The escape rate was found to be proportional to the emitted flux of photons that are more energetic than the energy barrier of the trap, in agreement with the photonic back-action model.

### 4.3 Sub-gap processes in SINIS single-electron transistors

In this section, we will review measurements of tunneling processes in a SINIS-type SET, where quasiparticles in the superconducting leads were efficiently evacuated (see Sec. 2.4), and the junctions were well shielded from microwave irradiation (Sec. 4.2). We take the viewpoint that the sub-gap tunneling processes, i. e., those observed at bias voltages less than  $\Delta/e$  per junction, are a measure of the inherent quality of the device. The measurement results presented in this section have been reported in Pub. IX, although some of the analysis is new. The sample layout can be seen in Fig. 3.1. At the heart of the sample chip there are two capacitively coupled SINIS SETs. These precautions were made to enable the study of the inherent transport properties of the SETs. The sample design is symmetric so that either one of the SETs can be employed as an electrometer that probes the other SET, which we will refer to as the device under test (DUT). The sample design includes a ground plane for capacitive shunting of bias and gate leads, superconducting leads that make a large area ( $8 \times 8 \mu\text{m}^2$ ) contact to gold electrodes for efficient quasiparticle evacuation, and a resistive Cr wire for realizing a coupling between the two SETs that cuts a part of the high-frequency back-action.

$I$ - $V$  measurements are the standard method for probing the subgap transport of NIS structures. However, subgap characterization of high-quality NIS and SINIS samples is challenging due to small transport current and high device impedance. In the  $I$ - $V$  measurements of low-temperature samples for this thesis, the best current noise levels were of the order of a few  $\text{fA}/\sqrt{\text{Hz}}$ . The smallest nonzero current readings we obtained were about  $0.1 \text{ fA}$  at a bias voltage of  $250 \mu\text{V}$ , which required an overnight measurement for a single  $I$ - $V$  curve. The true sub-gap resistance of the SINIS samples of Pub. IX inferred from electron counting measurements was about  $10^{13} \Omega$  at zero bias. Even if the current noise of the amplifier could be eliminated, parasitic conductance along the sample chip or sample holder might shunt the sample. The above-mentioned best subgap  $I$ - $V$  measurements yield a resistance of  $10^{12} \Omega$ . When measuring

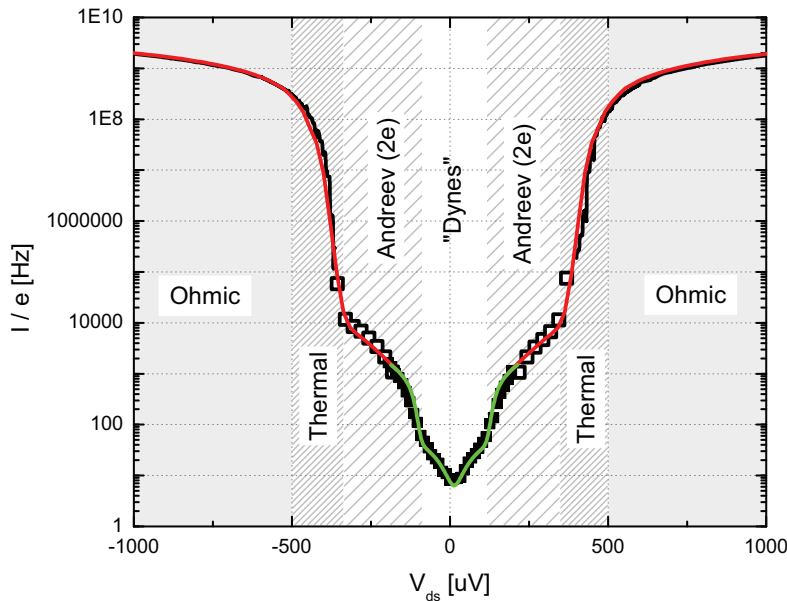


**Figure 4.5.** Combination plot of measured process rates in a SINIS SET. Black curves and markers are experimental data, whereas the colored curves are theoretical predictions. Experimental data for  $|V_{ds}| > 250 \mu\text{V}$  (black lines and open squares) is obtained from  $I$ - $V$  measurements averaged over gate modulation. Experimental data for  $|V_{ds}| < 250 \mu\text{V}$  (filled black squares) is the observed process rate in electron counting traces. Theoretical predictions have been calculated with parameters  $T = 50 \text{ mK}$ ,  $R_T = 1.1 \text{ M}\Omega$  per junction,  $\Delta = 210 \mu\text{V}$ ,  $E_c = 0.25\Delta$ , normalized conductance per channel  $g/N = 10^{-5}$ , and Dynes parameter  $\gamma = 1.5 \times 10^{-7}$ .

such high-impedance samples, it is crucial that the input of the current amplifier is kept at ground potential to prevent leakage currents through cabling and connectors from interfering with the measurement. For example, the BNC connectors that we used for room-temperature connections have their ground leakage resistance rated typically at  $5 \times 10^9 \Omega$ .

In the sample topology with two capacitively coupled SETs, it is possible to characterize the sample parameters  $R_T$ ,  $E_c$ , and  $\Delta$  from ordinary  $IV$  measurements with currents of the order of  $1 \text{ pA}$  and higher. In this way, the tunneling rates obtained from electron counting near zero bias can be compared to theoretical estimates calculated with the known sample parameters. This method was employed in the article to obtain the upper bounds  $\gamma < 1.6 \times 10^{-7}$  for the Dynes density of states and  $n_{qp} < 0.033 \mu\text{m}^{-3}$  for the density of non-equilibrium quasiparticles in the superconductor.

Following the original reasoning of Dynes *et al.* [17], we can infer an estimate for the quasiparticle recombination time from the experimental

broadening term. We have then  $\tau_r = \frac{\hbar}{2\gamma\Delta} = 10 \mu\text{s}$  as the experimental figure. The equilibrium result for quasiparticle relaxation time at low temperatures can be written as [89, 112]

$$\tau_r = \frac{\tau_0}{n_{\text{qp}}} \frac{N_0(k_{\text{B}}T_c)^3}{2\Delta^2}, \quad (4.10)$$

where  $\tau_0$  is a material parameter and assumes the value 460 ns for aluminum [89]. For the measured record-low quasiparticle density of  $n_{\text{qp}} = 0.033 \mu\text{m}^{-3}$ , the predicted recombination time is 6 s. Clearly, quasiparticle–quasiparticle relaxation is not responsible for the observed lifetime broadening. However, in the measured sample, the dominant quasiparticle evacuation mechanism is via the normal-metal traps located at a distance of  $L = 10 \mu\text{m}$  from the junction. Assuming a thermal distribution of quasiparticle energies, the average diffusion time to the trap site can be calculated according to

$$\tau_d = L^2/D_{\text{qp}}, \quad D_{\text{qp}} = D\sqrt{k_{\text{B}}T_{\text{S}}/(2\pi\Delta)}, \quad (4.11)$$

where  $D = 60 \text{ cm}^2/\text{s}$  is the diffusion constant for aluminum [70]. At temperature  $T_{\text{S}} = 122 \text{ mK}$  corresponding to the  $n_{\text{qp}}$  value stated above, we arrive at  $\tau_d = 200 \text{ ns}$ , which is shorter than the experimental life-time estimate by a factor 50. Although it is physically motivated to expect a quasiparticle trap placed too close to the junction site to induce effective subgap states, the simple model presented above appears to be too naive to capture the correct physics of the experimental scenario. One can also adopt the view that the Dynes parameter as employed here does not arise from a finite life-time of the quasiparticle states, but instead only characterizes the density of quasiparticle states in the superconducting gap at the junction site.

When both the electron counting and  $I$ – $V$  measurement techniques are pushed to their limits, it is possible to produce a semi-continuous plot of process rates as a function of bias voltage ranging from 8 Hz to  $2 \times 10^9$  Hz, which is illustrated in Fig. 4.5. The fact that there is an apparently seamless transition between the two data sets around  $|V_{\text{ds}}| = 250 \mu\text{V}$  is even surprising, as the count rates are obtained with the gate at degeneracy, whereas the plotted  $I$ – $V$  curve is an average over gate modulation. The explanation is two-fold. First, around that bias point, the quasiparticle transport is dominated by  $2e$  Andreev processes and gate modulation of the total current is relatively weak. Second, due to a mechanism explained shortly below, each Andreev event results in a passage of one

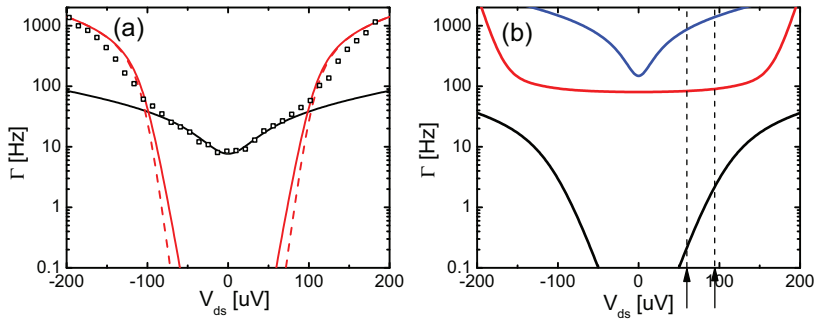


**Figure 4.6.** Rate parameters for first and second order tunneling processes in a SINIS-type SET as a function of  $V_{ds}$ . Sample parameters for theory calculations are as in Fig. 4.5. In panel (a), corresponding to the case of charge degeneracy, black markers show the rates inferred from  $1e$  jumps observed in the experimental data. Solid black and red curves are theoretical predictions for subgap states only and Andreev processes (followed by a fast  $1e$  relaxation) only, respectively. The dashed red curve accounts for the fact that some of the  $n = 2$  excitations relax back to  $n = 0$  via another  $2e$  Andreev process, and are not observed in the experiment. In panel (b), corresponding to the case of full Coulomb blockade, we plot the experimental rates for following processes:  $1e$  excitation from  $n = 0$  to  $n = \pm 1$  (black),  $1e$  relaxation from  $n = \pm 1$  to  $n = 0$  (red), and  $2e$  Andreev process from  $\pm 1$  to  $\mp 1$  (blue). Experimental electrometer traces measured at the two bias points indicated by arrows are presented in Fig. 4.7.

quasiparticle through the device in the direction of bias voltage, which enables the correspondence  $I_{\text{obs}} = e\Gamma_{\text{obs}}$  to be made.

In Pub. IX, the  $2e$  Andreev rates were not quantitatively analyzed, although they were considered to be a plausible explanation for some of the observed rates. Later, we learned that the electron count rates for  $|V_{ds}| > 100 \mu\text{V}$  and the low-bias behavior in measured  $I$ - $V$  curves could be relatively well explained by the theory of  $2e$  Andreev events presented in [71] and experimentally verified for an NIS single-electron box in Pub. VIII. For the theoretical calculations, the parameter  $g/\mathcal{N}$  describing normalized conductance per channel was set to the best-fit value of  $10^{-5}$ . This value is in good agreement with the value  $g/\mathcal{N} = 4 \times 10^{-5}$  obtained in Pub. VIII when adjusted for differing junction resistance and size. Contribution to electron counting traces is detailed in Fig. 4.6(a), where a baseline due to Dynes density of states is assumed.

For a more explicit proof that Andreev events were indeed occurring in the measured SET, we present electron counting traces obtained when the gate charge was tuned to full Coulomb blockade. The idea is the same that was employed earlier in Pub. VIII. In the electrometer traces on which the gate open data presented in Fig. 4.6(a) is based, actual  $2e$  jumps cannot be

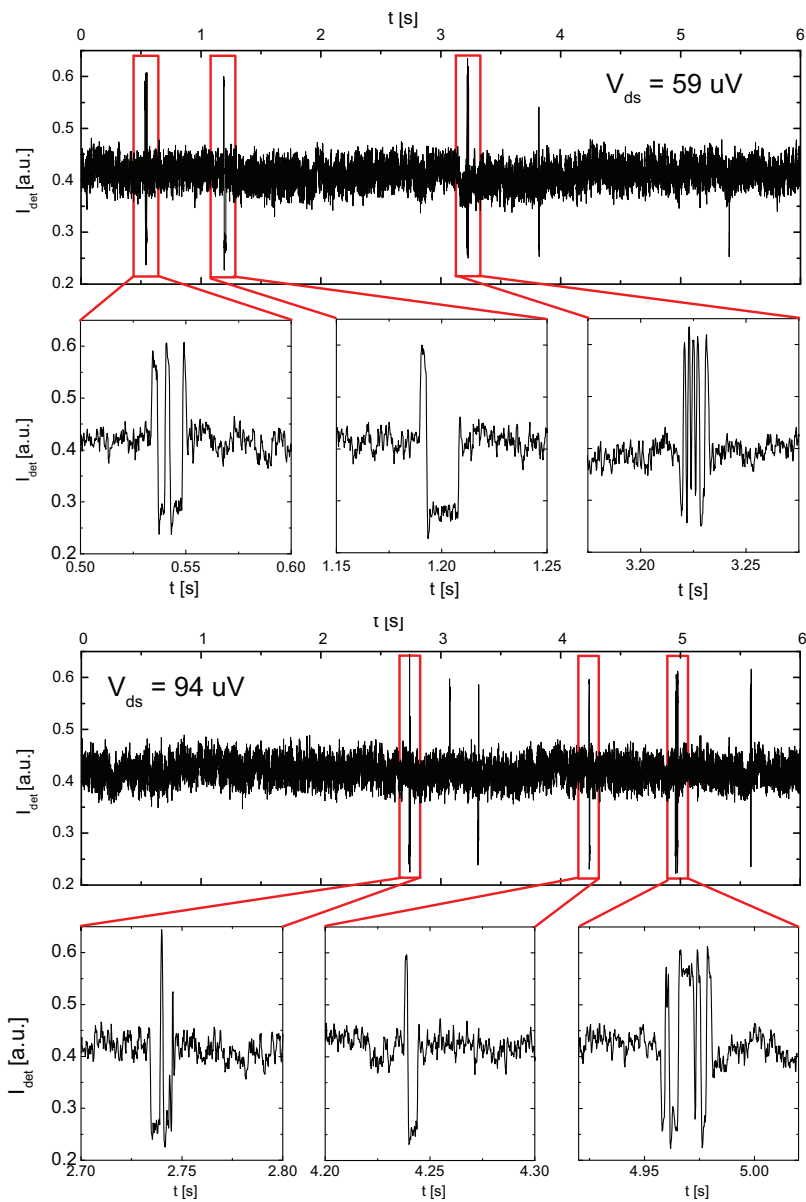


**Figure 4.7.** Experimental traces demonstrating  $2e$  oscillations in a Coulomb-blockaded SINIS-type SET.

observed, as the  $n = 2$  charge state populated by an Andreev event tends to relax into  $n = 1$  state via ordinary  $1e$  tunneling. Similar process takes place for  $n = -1$  that relaxes into  $n = 0$ . The rate parameter for the decay process is much larger than the bandwidth of the electrometer readout, and hence only a  $1e$  jump is observed. On the contrary, in full Coulomb blockade and suitable biasing, it is possible to observe characteristic  $2e$  oscillations in the charge state. This can be understood through the process rates plotted in 4.6(b): Once the system is excited into a state  $n = 1$  (case  $n = -1$  is similar) by  $1e$  tunneling, it is more likely to switch to the state  $n = -1$  via  $2e$  Andreev process than relax back to  $n = 0$  via  $1e$  process. Hence, in the experimental traces, one expects to see occasional bunches of rapid  $2e$  oscillations, with each bunch containing on average  $\Gamma^{2e}(1 \leftrightarrow -1)/\Gamma^{1e}(\pm 1 \rightarrow 0)$  jumps. The optimal bias voltage range, accounting for limited detector bandwidth and trace lengths of 6 seconds, is 50–100  $\mu V$ . Two such experimental traces, matching qualitatively the theoretical predictions, are shown in Fig. 4.7. Unfortunately, the amount of recorded electrometer traces does not allow for a quantitative analysis of the process parameters in the Coulomb blockaded case. In retrospect, the SINIS SET appears to be better suited for observation of  $2e$  events than the NIS single-electron box employed in Pub. VIII, as the process rates under biased conditions are more favorable for data acquisition.

#### 4.4 A quantized current source: The SINIS turnstile

In the preceding sections, we have established the high quality of the SINIS SET as a circuit element with experiments and theory spanning more than eight orders of magnitude in process rates for a single device. Furthermore, in Pub. VII, the charge trapping times in excess of 10 h were observed in an electron trap realized with a SINIS SET. These features combined with a relatively simple fabrication process and low number of control signals needed for device operation – one bias voltage and one gate voltage – make it a viable candidate for realizing an accurate source of quantized current. Chronologically, the first experimental and theoretical work on the current source idea, called the SINIS turnstile, was done shortly after the theory for rf-refrigeration (Pub. I) and the experiments on the heat transistor (Pub. II). The article included in this thesis, Pub. III, is the first experimental demonstration of current plateaus by an rf-driven SINIS turnstile.

The principal motivation for studying quantized current sources is two-fold [16]: First, an accurate single-electron source that produces a sufficiently high output current would enable a new definition of ampere in the SI system of units. Secondly, when viewed as a frequency-to-current converter, the current source would enable a consistency check between two already established quantum standards of electrical quantities: the resistance standard based on quantum Hall effect, and the voltage standard based on Josephson effect. Performing this experiment is said to close the quantum metrological triangle, and is considered to be one of the most important challenges in electrical metrology at the moment. The exact requirements on the current source depend on the specifics of the measurement setup. For a comparison performed on a current or voltage balance based on Ohm's law, a current of at least 100 pA at an accuracy of  $10^{-7}$  is required to produce metrologically interesting results [90]. Another variant is known as the electron counting capacitance standard (ECCS) [113, 114], where the current source is used to charge a cryogenic capacitance with a known number  $N$  of electrons, and the generated voltage is compared against the Josephson voltage standard. Compared to the direct Ohm's law scheme, the ECCS can be realized with a current source capable of producing smaller currents, but suffers from an additional source of uncertainty in the frequency dependence of the capacitor. The 7-junction normal metal pump used in the NIST ECCS experiment had an error rate of  $1.5 \times 10^{-8}$  when operated at a frequency of 5.05 MHz [115].

As is the case for all single-electron current sources, the basic operation principle of the SINIS turnstile is to transfer an integer number  $N$  of electrons from the source electrode to the drain in each cycle of an external drive signal at frequency  $f$ . The generated current is thus ideally  $I = Nef$ . The direction of current flow is set by voltage biasing the device at approximately  $V_{ds} = \Delta/e$ , i. e.,  $\Delta/(2e)$  per junction. For producing the  $N = 1$  plateau, which gives the highest accuracy in real devices, a cyclic drive signal of the form  $n_g(t) = -\frac{1}{2} + A_g \sin(2\pi ft)$  with  $A_g \sim \frac{1}{2}$  is applied to the gate. A square wave drive yields generally a better accuracy, but the signal shape can get distorted due to frequency dispersion present in real rf wiring. In Fig. 4.8(a), the simulated turnstile current as a function of  $A_g$  is plotted in the case of a sinusoidal drive and a few bias voltages around  $V_{ds} = \Delta/e$ , displaying a wide plateau.

For an elementary analysis of turnstile errors, we consider rate param-

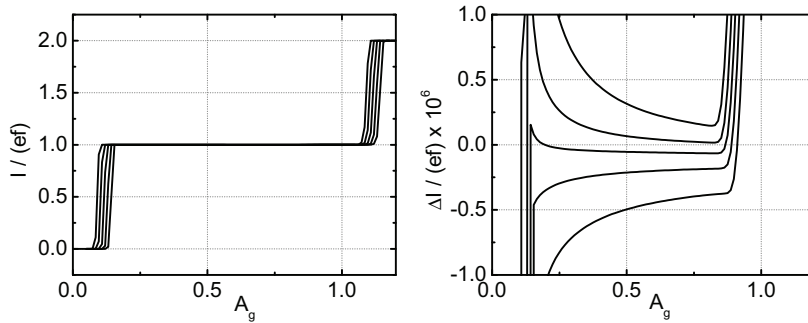


**Figure 4.8.** Simulated quantized current plateaus for  $f = 10$  MHz and  $V_{\text{ds}}/\Delta = 0.8, 0.9, 1.0, 1.1, 1.2$  in the order of increasing current. The rate parameters have been calculated with the same theoretical model as for Fig. 4.5, except that device parameters have been changed to  $E_c = 5$  K and  $R_T = 250$  k $\Omega$ .

eters for various tunneling properties in a scenario where the turnstile charge state is initially  $n = 0$ , and the gate charge is changed sharply to  $n_g = -1$  for the duration  $\tau = 1/(2f)$  of half a cycle, corresponding to an ideal square wave drive with  $A_g = 1/2$ . We assume the tunnel junctions are identical, so that the electron tunneling rates can be described by a single function  $\Gamma(E)$ . The rate parameter for an electron to tunnel in from the source lead is  $\Gamma(E_c + eV_{\text{ds}}/2)$ , which is what should occur in normal operation. The probability that this tunneling process is missed is

$$p_{\text{miss}} = \exp[-\tau\Gamma(E_c + eV_{\text{ds}}/2)]. \quad (4.12)$$

Furthermore, after the charge state  $n = 1$  has been occupied, another tunneling process to state  $n = 2$  can take place with rate parameter  $\Gamma(-E_c + eV_{\text{ds}}/2)$ . Assuming  $p_{\text{miss}}$  to be small, the probability of an extra electron tunneling during the cycle is

$$p_{\text{extra}} = 1 - \exp[-\tau\Gamma(-E_c + eV_{\text{ds}}/2)]. \quad (4.13)$$

In order to obtain an illustrative analytical answer for the minimized total error probability  $p_{\text{miss}} + p_{\text{extra}}$ , we assume that both  $\Gamma(E_c + eV_{\text{ds}}/2)$  and  $\Gamma(-E_c + eV_{\text{ds}}/2)$  lie in the range of thermal activation illustrated in Fig. 4.5. Then, we write  $\Gamma(\pm E_c + eV_{\text{ds}}/2) = \Gamma(eV_{\text{ds}}/2) \exp(\pm E_c/k_B T)$ , and the optimal total error probability is found to be

$$p_{\text{err}} = \frac{2E_c}{k_B T} e^{-2E_c/k_B T} \quad (4.14)$$

irrespective of the frequency  $f$ . However, the result is undoubtedly too optimistic and the practical performance is limited by features not described by the above approximation. Firstly, the forward transition rate ceases to

grow exponentially beyond  $V_{\text{ds}} > \Delta/e$ , and the generated current cannot exceed  $\Delta/(eR_{\text{T}})$ . Secondly, the leakage current does not decrease without bound as the  $E_{\text{c}}/k_{\text{B}}T$  ratio is increased, but is limited by the subgap processes.

For a more comprehensive estimate of turnstile performance, we have performed master equation based simulations incorporating the full theory for subgap behavior presented in Sec. 4.3 including  $2e$  Andreev processes. We assumed the same values for the Dynes parameter  $\gamma$  and normalized conductance per channel  $g/\mathcal{N}$ , but increased the charging energy to 5 K and decreased the junction resistance to 250 k $\Omega$ , which are still achievable values. In Fig. 4.8(b), close-ups of the plateau reveal differences from the ideal behavior at the  $10^{-7}$  relative error level for the best bias voltage  $V_{\text{ds}} = \Delta/e$ . An alternative view to turnstile accuracy is given in Fig. 4.9, where the distribution of the number  $n$  of electrons transferred per cycle is illustrated. Here, we observe that some amount of error cancellation takes place, as the probabilities for  $n = 0$  and  $n = 2$  are of the same order of magnitude near the best pumping parameters. The minimized total error probability is  $5 \times 10^{-7}$ . Depending on the application, the appropriate figure of merit may be either  $\delta I/I$  or  $1 - P(n = 1)$ . In the QMT experiment, only the average error  $\delta I$  is important, whereas an electron counting error measurement detects all pumping errors, and hence measures the total error probability  $1 - P(n = 1)$ .

The progression of the turnstile accuracy demonstrated in the experiments can be summarized as follows: In the first proof-of-concept demonstration (Pub. III), the accuracy was of the order of 1% for pumping frequencies up to 80 MHz. A significant improvement to better than  $10^{-3}$  accuracy at  $f = 10$  MHz was shown in Pub. IV by implementing the on-chip capacitive shunt and optimizing junction parameters. The best turnstile pumping result presented to date is an accuracy of  $10^{-4}$  at  $f = 20$  MHz by Knowles *et al.* [116], where an rf-tight sample stage was used and the geometry of the superconducting leads was improved to aid diffusion of injected quasiparticles away from the junctions. In light of the present knowledge about quasiparticle transport in SINIS structures, it is still plausible that an optimized SINIS turnstile could be used to perform the ECCS experiment, and that a parallelized array of turnstiles could be used as a metrological current source. However, to realize these ambitious goals, at least the following two technical challenges need to be solved.

First, thermalization of both the normal metal island and the super-

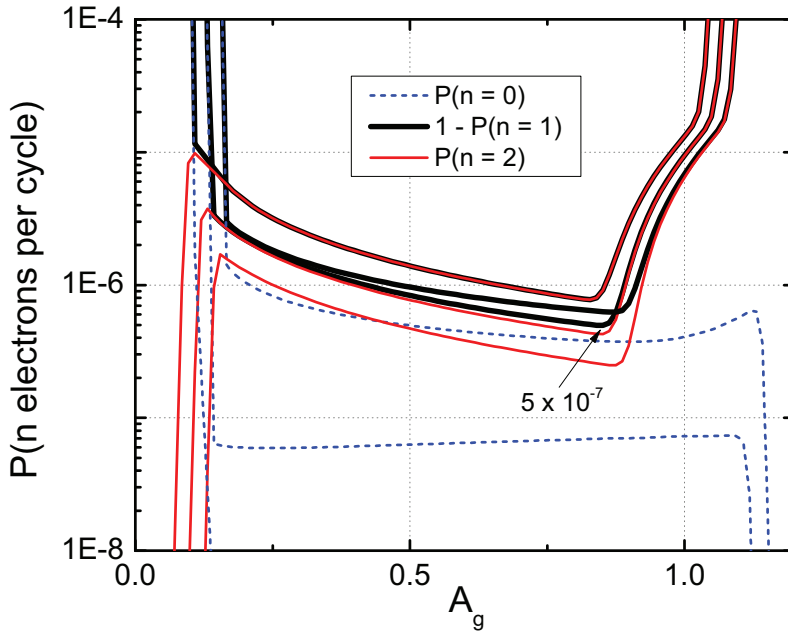


**Figure 4.9.** Distribution of simulated pumping errors for the curves  $V_{ds}/\Delta = 0.8, 1.0, 1.2$  from Fig. 4.8.  $P(n = 0)$  is the probability miss an electron transfer during a cycle (thin dashed line),  $P(n = 2)$  is the probability to transfer two electrons through the device (thin solid line), and  $1 - P(n = 1)$  gives the total error probability (thick solid line).

conducting leads deserve a detailed study. The volume of the turnstile island has to be kept small in order to maximize  $E_c$ , reducing the total effectiveness of electron-phonon coupling for island thermalization. Fortunately, it has been shown [109] that in an operation point where quantized current plateaus are produced, the normal island is actually cooled in a manner similar to the rf-refrigerator concept presented in Sec. 4.1. In the superconducting leads, the heating problem is more severe. Each electron transported through the turnstile creates a quasiparticle excitation in both superconducting leads. Hence, the local heating power injected to the superconductor at the junction is approximately equal to  $I\Delta/e$ . As discussed in Sec. 2.4, the electron-phonon coupling in superconducting materials is remarkably weak, and to dispose of this heat in practice, the hot quasiparticles have to be evacuated to a specifically designed quasiparticle trap. However, the normal metallic traps cannot be placed too close to the turnstile in order to avoid the degradation of the superconductivity at the turnstile junctions through inverse proximity effect.

Second, the experimentally observed area participation ratios of less

than 10% (see Sec. 2.3.2) are a concern for the design of high-performance turnstile devices. An optimized turnstile possesses a low tunneling resistance to enable high pumping speeds, a low junction capacitance to maximize  $E_c$ , and a low barrier transparency to hinder higher-order error processes. A low participation ratio necessitates a larger junction area to realize a given conductance, which results in a larger capacitance. For example, in the theoretical analysis of turnstile performance presented in Ref. [71], the authors predict a  $10^{-8}$  accuracy at a current level of 100 pA for a device with  $E_c = 10$  K and  $\mathcal{N} = 1000$  quantum channels. Using the theoretical estimate  $A_{\text{ch}} = 1.4 \text{ nm}^2$  (see Sec. 2.1.2), such a two-junction device with  $\text{AlO}_x$  barriers could have a charging energy up to 7.5 K. On the other hand, a calculation with the experimental value  $A_{\text{ch}} = 30 \text{ nm}^2$  leads to a charging energy of just 0.4 K. We envision that the ideal turnstile junction would be formed on the face of a single-crystalline aluminum grain, leading to a uniform barrier and thus a high participation ratio.

#### 4.5 Statistical mechanics of driven single-electron transitions

In the final experimental investigation of this thesis, we consider the process of charging mesoscopic conductors by individual electrons from the point of view of statistical physics. In Sec. 4.1, we have already considered the average heat deposited to or extracted from the electrodes of single-electron devices: the heat transistor concept deals with fixed gate charges only, i. e., the rate of change of the gate charges in the experiment is slow compared to the rate parameters of the typical tunneling processes. In the rf-refrigerator scheme, a small number of tunneling events takes place in each cycle of the external gate drive. From the same theoretical footing, it is possible to make a connection to some key topics of modern non-equilibrium statistical physics by extending the analysis to cover the full distribution of the thermodynamic quantities instead of the mean values only.

The physical system that we study is a single-electron box whose charge state is controlled by an external gate voltage. We demonstrate a method for determining the total amount of heat generated in a single gate ramp, and use this method to obtain the full distribution of generated heat. The properties of the obtained distributions are shown to obey the Jarzynski [14] and Crooks [15] fluctuation relations (FRs), which are two fundamental results of non-equilibrium statistical physics. Classical ther-

modynamics governs the behavior of a wide range of physical systems and man-designed machines. However, thermodynamical theorems are usually formulated in the limit of large systems, i. e., when the particle number and number of degrees of freedom approaches infinity. Some of the established notions need to be re-evaluated when dealing with small systems having a very restricted number of degrees of freedom. In this sense, the single-electron box can be thought of as one of the "smallest" systems possible, having only one discrete degree of freedom: the number  $n$  of elementary charges transferred from, say, the left electrode to the right. This fact, combined with an excellent microscopic understanding of the dynamics of  $n$ , makes the single-electron box an ideal testbed of FRs in mesoscopic physics.

Consider a system obeying classical mechanics described by a Hamiltonian  $H = H(\mathbf{x}, \lambda)$ , where the vector  $\mathbf{x}$  represents the internal degrees of freedom and  $\lambda$  is an external control parameter. The setting for the equilibrium FRs that are of interest here is the response of the system, initially in thermal equilibrium at temperature  $T$  at time  $t = t_i$ , to a variation of the control parameter along a predetermined trajectory  $\lambda = \lambda(t)$  lasting until time  $t_f$ . This is referred to as the *protocol*. We define the dissipated work  $W_{\text{dis}}$  as

$$W_{\text{dis}} = W - \Delta F, \quad (4.15)$$

where  $W$  denotes the thermodynamical work performed on the system during the protocol, and  $\Delta F = F(\lambda(t_f)) - F(\lambda(t_i))$  the change in Helmholtz free energy. The general definition of  $W$  applicable here is

$$W = \int_{t_i}^{t_f} \frac{\partial H}{\partial \lambda} \dot{\lambda} dt, \quad (4.16)$$

and the free energy is defined through the partition function  $Z(\lambda)$  as

$$Z(\lambda) = \sum_{\mathbf{x}} e^{-\beta H(\mathbf{x}, \lambda)} \quad (4.17)$$

$$F(\lambda) = -\beta^{-1} \ln Z(\lambda), \quad (4.18)$$

where  $\beta = 1/(k_B T)$ . The Second Law can be now formulated as

$$\langle W_{\text{dis}} \rangle \geq 0, \quad (4.19)$$

where the ensemble average is taken over microscopic realizations of the protocol. It states that the average work exerted on the system in changing the control parameter  $\lambda$  must be larger or equal to the free energy difference at the end points of the protocol. However, the work performed on

the system depends on the microscopic trajectory traversed by the system, and hence fluctuates between repetitions of the protocol. In particular, for some trajectories, one may find  $W < \Delta F$ , although  $\langle W \rangle \geq \Delta F$  holds for the mean value.

It is a characteristic feature of small system experiments that such entropy-reducing trajectories can make up a significant fraction of the observed trajectories. The landmark Jarzynski equality states that, for a system starting in thermal equilibrium,

$$\left\langle e^{-\beta W_{\text{dis}}} \right\rangle = 1, \quad (4.20)$$

where the ensemble average again is taken over microscopic realizations. The Crooks relation is a stronger result that can be written for  $W_{\text{dis}}$  as

$$\frac{P_F(-W_{\text{dis}})}{P_R(W_{\text{dis}})} = e^{-\beta W_{\text{dis}}}, \quad (4.21)$$

where  $P_F$  and  $P_R$  are the probability distributions of  $W_{\text{dis}}$  when the protocol is performed in the forward (usual) direction and in reverse, i. e.,  $\bar{\lambda}(t) = \lambda(t_i + t_f - t)$ , respectively. In the past 10 years, a number of experimental tests [117, 118, 119, 120, 121, 122] have been performed probing various aspects of FRs. The experiment we report in Pub. XI is the first such test in an electronic system where the control parameter protocol could be implemented. Compared to previous experimental investigations of Eqs. (4.20) and (4.21), the implementation on an electronic platform brings about a comprehensive microscopic theory and the ability to collect statistics over  $10^5$  repetitions of the control protocol.

Equations (4.19)-(4.18) constitute a general formal recipe allowing the FRs (4.20) and (4.21) to be applied to any classical system. We have implemented this method in Pub. X, starting from the construction of the classical Hamiltonian for the single-electron box circuit and the voltage source controlling the gate charge. However, the experimental method employed in Pub. XI can be derived with a much shorter reasoning that we will present here. We take advantage of the simplifying conditions that (i) the experiment was performed in Coulomb blockade, i. e.,  $E_c/(k_B T) \gg 1$  and (ii) the gate protocol started at  $n_g = 0$  and ended at  $n_g = 1$ . At the highest employed experimental temperature of 214 mK, the  $E_c/(k_B T)$  ratio was 9.1. Consequently, at the beginning and end of the protocol, the charge state of the box would essentially always be the minimum-energy state  $n = n_g$ . As we show in detail in Pub. X, the essential source of fluctuations in  $W_{\text{dis}}$  is the behavior in the middle of the sweep when  $n_g$  is close

to degeneracy. The fluctuations of the charge state at the endpoints can be ignored at the level of statistical accuracy achieved in the experiment. Hence, we obtain

$$W_{\text{dis}} = W - \Delta F = W - \Delta U + T\Delta S = W - \Delta U = Q, \quad (4.22)$$

where  $Q$  is the total heat generated during the protocol application. In the above derivation, we have utilized the general theorem  $F = U - TS$  and the fact that  $S = 0$  at the endpoints as per the preceding reasoning. The above equality thus allows us to write the FRs (4.20) and (4.21) in terms of the generated heat  $Q$ .

Now, the heat  $Q$  could be determined in a calorimetric manner by relating it to the observed temperature change in the box electrodes. However, the technical requirements of a true calorimetry scheme are beyond those presently demonstrated, although in principle feasible. In the experiments of Pub. XI, we determined  $Q$  for an individual trajectory from the observed timing of the electron tunneling events. In an elastic tunneling event from electrode  $L$  to  $R$ , the heat extracted from electrode  $L$  equals  $E - \mu_L$  and the heat deposited to electrode  $R$  equals  $E - \mu_R$ , where  $E$  is the kinetic energy of the tunneling quasiparticle. Hence, the total heat deposited into both electrodes equals  $Q = \mu_L - \mu_R = 2E_c(n_g - \frac{1}{2})$ .

We are now in a position to describe the complete experimental method of Pub. XI. We apply a sinusoidal drive signal  $n_g = \frac{1}{2} + \frac{1}{2} \cos(2\pi ft)$  to the gate of a NIS single-electron box, and monitor simultaneously the charge state with an SET electrometer. To ensure that the tunneling dynamics were governed by the equilibrium thermal fluctuations, the experimental data was acquired at relatively high temperatures up to 214 mK. As illustrated by Fig. 4.3, the crossover temperature to non-thermal behavior in a single-electron box experiment is below 150 mK. The employed drive frequencies  $f$  were 1–20 Hz in order to accommodate for the low detector bandwidth of approximately 1000 Hz. Each half cycle constituted an individual realization of the gate protocol, transforming the system state from  $n = n_g = 0$  to  $n = n_g = 1$ , or vice versa. From the observed stochastic tunneling times  $\tau_i$ , the total heat generated in the sweep can be evaluated as the sum

$$Q = \sum_{i=1}^N (-1)^{i+1} 2E_c(n_g(\tau_i) - \frac{1}{2}), \quad (4.23)$$

where  $N$  is the number of tunneling events in the trace. Equation 4.23 was originally presented in Ref. [13].

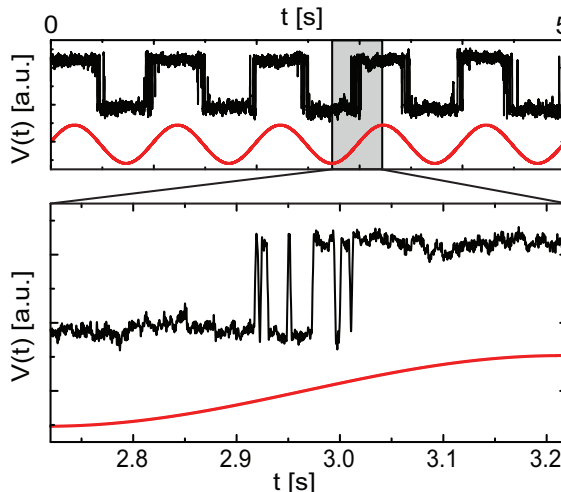


**Figure 4.10.** Experimental trace from the data of Pub. XI. The red trace shows the sinusoidal drive applied to the gate of the box, and black trace is the electrometer response, illustrating that the charge state is synchronized to the drive signal. Peak-to-peak amplitude of the drive corresponds to approximately  $1e$  in gate charge. The close-up shows one half cycle of the drive (shaded area in the top panel), corresponding to one instance of the gate control protocol used for tests of fluctuation relations.

A typical experimental time trace acquired in the experiment is shown in Fig. 4.10. After the switching events have been identified by threshold detection from the electrometer trace, evaluation of  $Q$  for this particular trajectory is straightforward by application of Eq. 4.23. For determining the full  $Q$  distribution, we recorded the electrometer traces for at least 1000 repetitions of the gate protocol. In Fig. 4.11, we show a set of experimental distributions obtained at 182 mK for drive frequencies 1–20 Hz. In Figs. 2(b) and (c) of Pub. XI, the first and second moment of  $Q$  distribution as a function of frequency at 182 mK is computed from this data. The largest datasets for a single  $Q$  distribution we acquired contain  $1\text{--}4 \times 10^5$  repetitions of the gate protocol. These distributions were used for the most accurate test of the Jarzynski and Crooks fluctuation relations. The Jarzynski-type exponential average  $\langle e^{-\beta Q} \rangle$  could be evaluated to 3 % accuracy, with the offset attributed to charge noise and finite detector bandwidth. The noise level in the determination of  $Q$  for a single trajectory was found to be  $0.032 k_B T$  at 214 mK.

Theoretical description of the  $Q$  distributions at a qualitative level is possible from general thermodynamic principles. The single microscopic parameter that is needed is a rate parameter  $f_c$  describing internal en-

ergy relaxation of the system. At frequencies much smaller than  $f_c$ , the drive can be considered adiabatic, and both  $\langle Q \rangle$  and  $\langle Q^2 \rangle$  vanish, i. e., all individual trajectories show zero dissipation. In general, for  $f \lesssim f_c$ , the distribution of  $Q$  is approximately Gaussian and the first and second moments are related by  $\langle (Q - \langle Q \rangle)^2 \rangle = 2k_B T \langle Q \rangle$ . This can be shown by a series expansion of JE or by an application of the Fluctuation-Dissipation Theorem [13].

For  $f \gg f_c$ , the drive is nonadiabatic and heat generation is maximized. For the single-electron box,  $f_c$  can be taken to be the tunneling rate at degeneracy. At 182 mK, this rate was found to be 9 Hz by observing the stochastic tunneling without a gate drive. The distributions presented in Fig. 4.11 fit well to the above description: For the highest studied frequencies, about  $E_c/2$  of heat is dissipated in each trajectory, but the distribution contains a long tail extending to negative  $Q$  values. As the drive frequency is lowered below 5 Hz, the peak of the distribution starts to move toward zero. Observing the fully adiabatic regime would require even lower drive frequencies. This is explained by the fact that for the sinusoidal  $n_g$  drive employed here, the rate of change near the charge degeneracy point is  $2\pi f$ . Hence, near the degeneracy, even the 1 Hz drive is fast enough so that the system cannot follow it adiabatically.

The theoretical framework we have established allows the charge state of the single-electron box in response to an external gate drive to be simulated. Following the procedure of Pub. V, we extract the parameters  $R_T$ ,  $E_c$ , and  $\Delta$  by observing the stochastic quasiparticle tunneling events for different constant values of the gate charge  $n_g$  and temperatures  $T$ . The data sets of parameter extraction are shown in the supplemental material of Pub. XI. For the purposes of testing the FRs (4.20) and (4.21), it is crucial that the charge degree of freedom is coupled to an equilibrium environment at a single temperature  $T$ . Hence, we will assume fully thermalized quasiparticle distributions in the box electrodes, and a negligible coupling to fluctuations of the electromagnetic environment. Given the tunneling rate as a function of energy  $\Gamma(E)$ , the full  $Q$  distribution can be evaluated efficiently without a Monte Carlo simulation using the method described in Sec. 5.2. In Fig. 4.11, we show the theoretical distributions obtained in this manner. We find them to be in good agreement with the experimental data.

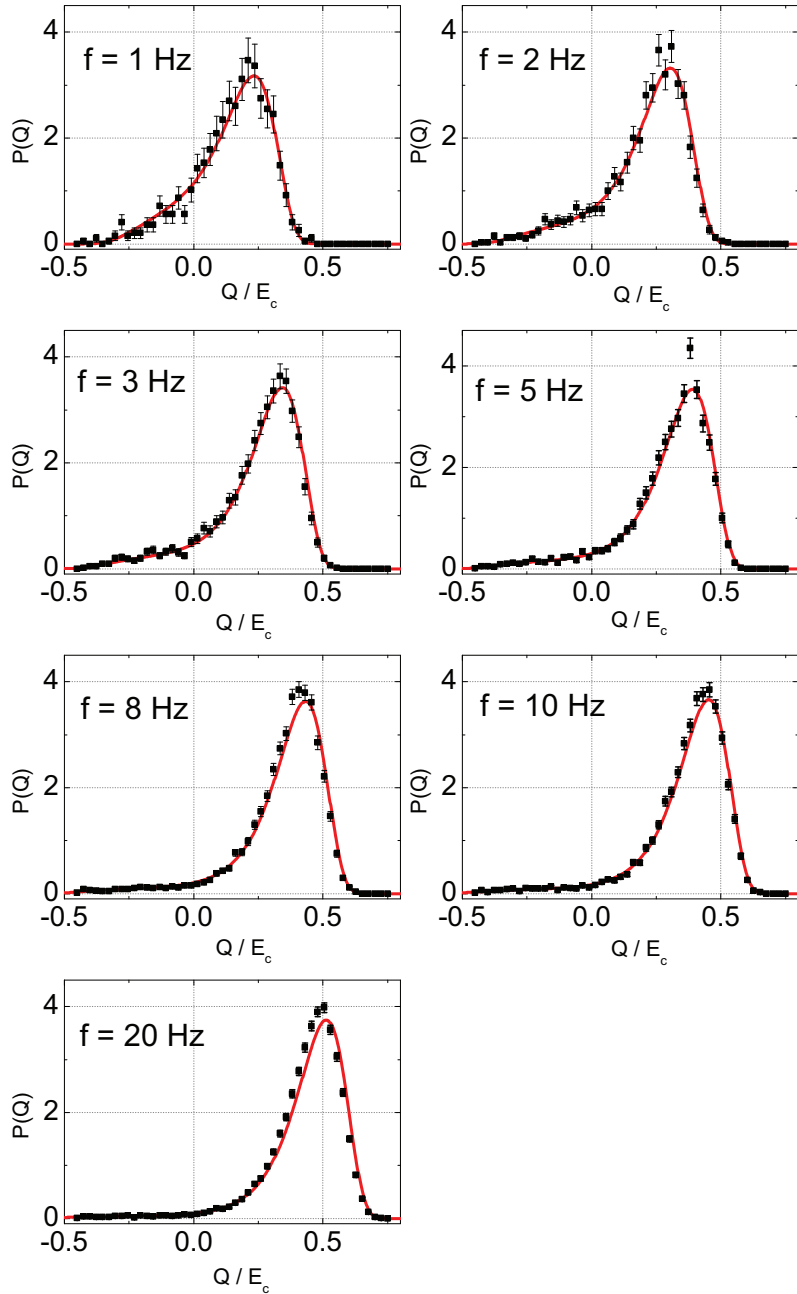


**Figure 4.11.** Full distributions of generated heat at 182 mK for drive frequencies 1–20 Hz. The gate drive is sinusoidal, centered at the charge-degeneracy point  $n_g = 1/2$ , and has a peak-to-peak amplitude corresponding to  $1e$  in gate charge. Black markers show the experimental distribution obtained from a data set with total length of 500 s. Red curves are simulated distributions for the known sample parameters at  $T = 182$  mK, which was determined by an independent thermometer on the sample stage.



# 5. Numerical methods

## 5.1 Master equations for single-electron transport

In this section, we present a general framework for calculating time-averaged electric and heat currents in a single-electron system with a master equation approach. As in Sec. 2.2.2, we assume a general setting of  $N$  islands and  $M$  voltage terminals. For clarity, we will use the indexing variable  $i$  to refer to the voltage terminals only, and variables  $j$  and  $k$  for the islands. The system state at any given time  $t$  is specified by the vector  $\mathbf{V}$  of external voltages  $V_i$ , and the integer vector  $\mathbf{n}$ , where the component  $n_j$  expresses the excess charge of island  $j$  in units of the elementary charge. An effective way to perform the averaging over the stochastic charge state trajectory is to consider the probability distribution  $p(\mathbf{n}, t)$  of different charge states  $\mathbf{n}$ . The time-dependence of  $p$  is given by the master equation

$$\frac{dp(\mathbf{n}, t)}{dt} = - \sum_{\mathbf{n}' \neq \mathbf{n}} \gamma(\mathbf{n}, \mathbf{n}') p(\mathbf{n}, t) + \sum_{\mathbf{n}' \neq \mathbf{n}} \gamma(\mathbf{n}', \mathbf{n}) p(\mathbf{n}', t), \quad (5.1)$$

where  $\gamma(\mathbf{n}, \mathbf{n}')$  denotes the total transition rate of all elementary processes that change the charge state from  $\mathbf{n}$  to  $\mathbf{n}'$ .

Let us consider how to construct the rate matrix elements  $\gamma(\mathbf{n}, \mathbf{n}')$ . Single-electron tunneling events between a lead and an island contribute according to

$$\gamma([\dots n_j \dots], [\dots (n_j \pm 1) \dots]) = \sum_i \Gamma_{ij}^{1e}(-\Delta F_c \pm eV_j), \quad (5.2)$$

where  $\Delta F_c = F_c(\mathbf{n}') - F_c(\mathbf{n})$  is the change in the charging energy potential defined in Eq. (2.45), and  $\Gamma_{ij}^{1e}$  is the tunneling rate from orthodox theory [Eq. (2.7)] for the junction between lead  $i$  and island  $j$ . The absence of a tunnel junction is formally equivalent to  $R_T = \infty$  in the present context.

Two-electron Andreev processes can be treated similarly,

$$\gamma([\dots n_j \dots], [\dots (n_j \pm 2) \dots]) = \sum_i \Gamma_{ij}^{2e}(-\Delta F_c \pm 2eV_j). \quad (5.3)$$

Finally, if the system has multiple islands with tunnel junctions between them, the inter-island processes contribute terms of the type

$$\gamma([\dots n_j \dots n_k \dots], [\dots (n_j \pm 1) \dots (n_k \mp 1) \dots]) = \Gamma_{jk}^{1e}(-\Delta F_c), \quad (5.4)$$

$$\gamma([\dots n_j \dots n_k \dots], [\dots (n_j \pm 2) \dots (n_k \mp 2) \dots]) = \Gamma_{jk}^{2e}(-\Delta F_c). \quad (5.5)$$

For all combinations of charge states  $\mathbf{n}$  and  $\mathbf{n}'$  except for those explicitly listed above,  $\gamma(\mathbf{n}, \mathbf{n}') = 0$ . It should be noted that if the voltages  $V_j$  are time (in)dependent, the same holds for the rates  $\gamma(\mathbf{n}, \mathbf{n}')$ .

If the distribution  $p(\mathbf{n}, t)$  is known, the expectation value of the electric current to lead  $i$  can be obtained from

$$\langle I_i(t) \rangle = e \sum_{\mathbf{n}} p(\mathbf{n}, t) \left( \Gamma_{i,\mathbf{n}}^{1e,\text{in}} - \Gamma_{i,\mathbf{n}}^{1e,\text{out}} \right) + 2e \sum_{\mathbf{n}} p(\mathbf{n}, t) \left( \Gamma_{i,\mathbf{n}}^{2e,\text{in}} - \Gamma_{i,\mathbf{n}}^{2e,\text{out}} \right), \quad (5.6)$$

where  $\Gamma_{i,\mathbf{n}}^{1e,\text{in(out)}}$  is the rate parameter for  $1e$  tunneling to (from) lead  $i$  when the system is in charge state  $\mathbf{n}$ , and  $\Gamma_{i,\mathbf{n}}^{2e,\text{in(out)}}$  is the rate for the  $2e$  Andreev processes. Each term in Eqs. (5.2)-(5.3) corresponds to exactly one term in Eq. (5.6).

In the modeling work for this thesis, we only considered the heat flow to a normal metal island due to  $1e$  events in either single-electron box or single-electron transistor configuration. In this case, we can write simply

$$\langle \dot{Q}^N(t) \rangle = \sum_{\mathbf{n}} p(\mathbf{n}, t) \left( \dot{Q}_{i,\mathbf{n}}^{N,1e,\text{in}} + \dot{Q}_{i,\mathbf{n}}^{N,1e,\text{out}} \right). \quad (5.7)$$

For a numerical implementation, one chooses a representative set of charge states  $\{\mathbf{n}_\lambda\}_{\lambda=1}^L$  so that the probability mass of the states outside this set is negligible. The master equation (5.1) can be written in matrix form as

$$\frac{d\mathbf{p}(t)}{dt} = A(t)\mathbf{p}(t), \quad (5.8)$$

where  $A_{\lambda,\lambda} = -\sum_{\lambda' \neq \lambda} \gamma(\mathbf{n}_\lambda, \mathbf{n}_{\lambda'})$ ,  $A_{\lambda',\lambda} = \gamma(\mathbf{n}_\lambda, \mathbf{n}_{\lambda'})$  for  $\lambda' \neq \lambda$ , and  $p_\lambda(t) = p(\mathbf{n}_\lambda, t)$ .

If the external voltages are constant in time, also the matrix  $A(t)$  is constant and the distribution  $\mathbf{p}(t)$  tends to the steady-state solution  $\mathbf{p}^{\text{eq}}$  defined by

$$A\mathbf{p}^{\text{eq}} = 0, \quad \sum_j p_j^{\text{eq}} = 1. \quad (5.9)$$

Average electric and heat currents can be computed by direct evaluation of Eqs. (5.6) and (5.7).

The second case we consider is that of a time-dependent cyclic drive, i. e.,  $\mathbf{V}(t + \tau) = \mathbf{V}(t)$  for some cycle length  $\tau$ . It follows that the probability density should converge to a steady-state solution  $\mathbf{p}^{\text{eq}}(t)$  that has the same periodicity,  $\mathbf{p}^{\text{eq}}(t + \tau) = \mathbf{p}^{\text{eq}}(t)$ . We discretize the cycle into  $N_t$  time steps of length  $\Delta t = \tau/N_t$ , and approximate  $A(t)$  during the time interval  $[m \Delta t, (m + 1) \Delta t]$  by the constant  $A_m = A(m \Delta t)$  for  $m = 0 \dots N_t - 1$ . The propagator for the probability density over the full cycle is then given by

$$U(\tau) = \exp(\Delta t A_{N_t-1}) \cdots \exp(\Delta t A_1) \exp(\Delta t A_0). \quad (5.10)$$

Solution by matrix exponentiation is much preferred over solving Eq. (5.8) by explicit methods due to the fact that the non-zero transitions rates contained in  $A(t)$  can easily vary by 10 orders of magnitude, making the problem very stiff. The steady state distribution at the beginning of the drive cycle,  $\mathbf{p}^{\text{eq}}(0)$ , is determined by the equations

$$U(\tau)\mathbf{p}^{\text{eq}}(0) = \mathbf{p}^{\text{eq}}(0), \quad \sum_j p_j^{\text{eq}}(0) = 1. \quad (5.11)$$

The density at an arbitrary point of the cycle can be then calculated as  $\mathbf{p}^{\text{eq}}(t) = U(t)\mathbf{p}^{\text{eq}}(0)$ , where  $U(t)$  is the natural generalization of Eq. (5.10) for  $t < \tau$ .

Finally, we show how to calculate accurately the total charge transferred to the lead  $i$  during the steady-state cycle. We define  $\langle q_i(\tau') \rangle = \int_0^{\tau'} dt \langle I_i(t) \rangle$ , and construct an augmented state vector  $\tilde{\mathbf{p}}(t) = \begin{bmatrix} \mathbf{p}(t) \\ \langle q_i(t) \rangle \end{bmatrix}$ .

The time development of  $\tilde{\mathbf{p}}$  is given by

$$\frac{d\tilde{\mathbf{p}}(t)}{dt} = \begin{bmatrix} A(t) & \mathbf{0} \\ \mathbf{b}(t) & 1 \end{bmatrix} \tilde{\mathbf{p}}(t) \equiv \tilde{A}(t)\tilde{\mathbf{p}}(t), \quad (5.12)$$

where the matrix  $A(t)$  defined similarly as in Eq. 5.8, and the components of the row vector  $\mathbf{b}(t)$  are

$$b_\lambda(t) = e \left( \Gamma_{i,\mathbf{n}_\lambda}^{1e,\text{in}} - \Gamma_{i,\mathbf{n}_\lambda}^{1e,\text{out}} \right) + 2e \left( \Gamma_{i,\mathbf{n}_\lambda}^{2e,\text{in}} - \Gamma_{i,\mathbf{n}_\lambda}^{2e,\text{out}} \right) \quad (5.13)$$

in accordance with Eq. (5.6). We construct the augmented propagator  $\tilde{U}(\tau)$  following the earlier procedure, and decompose it as

$$\tilde{U}(\tau) = \begin{bmatrix} U(\tau) & \mathbf{0} \\ U_{q_i}(\tau) & 1 \end{bmatrix}, \quad (5.14)$$

where  $U(\tau)$  defined by the above equation is equal to that given in Eq. (5.10) by construction. The expectation value of the charge transferred in the steady-state cycle is then given by

$$\langle q_i(\tau) \rangle_{\text{eq}} = U_{q_i}(\tau)\mathbf{p}^{\text{eq}}(0), \quad (5.15)$$

where  $p^{\text{eq}}(0)$  is obtained from Eq. (5.11). The same procedure can be used to find the expectation value of total heat deposited to an island,  $\langle Q_i^N(\tau) \rangle_{\text{eq}}$ .

## 5.2 Computation of the distribution of dissipated heat in a driven two-level system

In Sec. 4.5, we analyzed the statistics of heat generated in a single-electron box subjected to a gate drive. We showed that the dissipated heat in a single instance of a gate protocol that drives the charge state from  $n = 0$  to  $n = 1$  is given by

$$Q = 2E_c \sum_i (-1)^{i+1} \left[ n_g(\tau_i) - \frac{1}{2} \right], \quad (5.16)$$

where  $E_c$  is the charging energy of the box,  $n_g(t)$  is the gate charge in units of  $e$  at time  $t$ , and  $\tau_i$  is the time instant of the  $i$ th tunneling transition during the sweep. The time-dependent energy difference of the two charge states is

$$\Delta E = F_c(n = 1) - F_c(n = 0) = -2E_c \left[ n_g(t) - \frac{1}{2} \right]. \quad (5.17)$$

The tunneling processes are Markovian, and the rate parameters for the  $0 \rightarrow 1$  and  $1 \rightarrow 0$  transitions (denoted by  $+$  and  $-$ , respectively) are given by  $\Gamma^\pm(t) = \Gamma(\mp \Delta E)$ , where the function  $\Gamma(E)$  is determined by junction properties.

We wish to study the distribution of  $Q$  for a particular gate protocol  $n_g(t)$  averaged over the stochastic tunneling trajectories. We will denote the density function of this distribution by  $p_Q(Q)$ , so that the expectation value of any function  $f(Q)$  can be evaluated as  $\langle f(Q) \rangle = \int dQ p_Q(Q) f(Q)$ .

Without loss of generality, we assume that the gate protocol begins at time instant  $t = 0$  and finishes at  $t = T$ . In this case, Eq. (5.16) can be rewritten as

$$\frac{Q}{2E_c} = \int_0^T dt n_g(t) \frac{dn(t)}{dt} = n_g(t)n(t)|_0^T - \int_0^T dt \frac{dn_g(t)}{dt} n(t), \quad (5.18)$$

where  $n(t)$  is the charge state of the box (either 0 or 1) at time  $t$ . For treating the remaining integral term, we define a new function  $W(t)$  by

$$W(t) = \int_0^t d\tau \frac{dn_g(\tau)}{d\tau} n(\tau), \quad (5.19)$$

so that  $Q/(2E_c) = 1 - W(T)$ , if we make the simplifying assumptions  $n(0) = n_g(0) = 0$  and  $n(T) = n_g(T) = 1$ . In the remaining, we will consider the time evolution of the density function of  $W$ , which we denote by

$\rho(W, t)$ . The density function  $p_Q$  defined above is related to  $\rho$  through

$$p_Q(Q) = \frac{1}{2E_c} \rho\left(1 - \frac{Q}{2E_c}, T\right). \quad (5.20)$$

We decompose the  $W$  distribution into two terms

$$\rho(W, t) = \rho^-(W, t) + \rho^+(W, t), \quad (5.21)$$

where  $\rho^-(W, \tau)$  is the  $W$  distribution over trajectories for which  $n(\tau) = 0$ , normalized so that  $\int dW \rho^-(W, \tau)$  gives the occupation probability of the state  $n = 0$  at  $t = \tau$ . The conditional distribution  $\rho^+(W, \tau)$  is defined similarly with respect to state  $n = 1$ . Let us consider the time-dependent Fourier components of the conditional distributions, defined as

$$C^\pm(k, \tau) = \int_{-\infty}^{\infty} dW e^{-i2\pi k W} \rho^\pm(W, t). \quad (5.22)$$

At  $\tau = 0$ , we have  $\rho^-(W) = \delta(W)$  and  $\rho^+(W) = 0$ , which translate into  $C^-(k, 0) \equiv 1$  and  $C^+(k, 0) \equiv 0$ . In a numerical implementation, it is preferable to choose a Gaussian wave packet  $C^-(k, 0) = e^{-(\sigma k)^2}$  as the initial condition to avoid truncation artifacts in the final result.

Let us consider a small time step from  $t = \tau$  to  $t = \tau + \Delta t$ , and derive an update rule for  $C^\pm(k, t)$  that is accurate to first order in  $\Delta t$ . If  $n(\tau) = 0$ , and no transition occurs during the time step, the value of the  $W$  integral does not change. On the other hand, if  $n(\tau) = 1$ , and no transition occurs, the increment to  $W$  is given by

$$W(\tau + \Delta t) - W(\tau) = \int_{\tau}^{\tau + \Delta t} dt \frac{dn_g(t)}{d\tau} = n_g(\tau + \Delta t) - n_g(\tau) \equiv \Delta n_g(\tau). \quad (5.23)$$

This is equivalent to shifting the distribution  $\rho^+(W, \tau)$  by  $\Delta n_g(\tau)$ . Hence, without state transitions, the exact update rule reads

$$C^-(k, \tau + \Delta t) = C^-(k, \tau) \quad (5.24)$$

$$C^+(k, \tau + \Delta t) = e^{-i2\pi k \Delta n_g(\tau)} C^+(k, \tau). \quad (5.25)$$

To account for state transitions, we first define  $P_{ij}$  as the Markovian transition probability from charge state  $j$  to  $i$ , i. e.,

$$P_{ij} = P(n(\tau + \Delta t) = i | n(\tau) = j). \quad (5.26)$$

Approximating the transition rates  $\Gamma^\pm(t)$  during the time step by their values at  $t = \tau$ , the  $P_{ij}$  can be conveniently evaluated with matrix exponentiation as

$$\begin{bmatrix} P_{00} & P_{01} \\ P_{10} & P_{11} \end{bmatrix} = e^{\Gamma(\tau)\Delta t} = \begin{bmatrix} 1 - \Gamma^+(\tau)\Delta t & \Gamma^-(\tau)\Delta t \\ \Gamma^+(\tau)\Delta t & 1 - \Gamma^-(\tau)\Delta t \end{bmatrix} + O(\Delta t^2). \quad (5.27)$$

The matrix exponential form is preferred in numerical implementations for its inherent stability even with large  $\Gamma(\tau)\Delta t$ . The non-diagonal terms  $P_{01}$  and  $P_{10}$  account for the possibility to change the charge state during the time step, which promotes mixing of the conditional distributions. Since the diagonal terms are already first order in  $\Delta t$ , accumulation of phase during the time step can be neglected if the transition occurs. We can now write the full update rule for  $C^\pm(k, t)$  in a short time step  $\Delta t$  as

$$C^-(k, \tau + \Delta t) = P_{00}C^-(k, \tau) + P_{01}C^+(k, \tau), \quad (5.28)$$

$$C^+(k, \tau + \Delta t) = P_{11}e^{-2i\pi k\Delta n_g(\tau)}C^+(k, \tau) + P_{10}C^-(k, \tau). \quad (5.29)$$

Using the above equations, the time dependence of an arbitrary collection of Fourier coefficients can be solved numerically in an efficient manner. We note that the dc-component  $C^\pm(0, \tau)$  gives the probability of occupying state  $n = 0$  ( $n = 1$ ) at time instant  $t = \tau$ .

At the end of the simulation, the density function  $p_Q(Q)$  can be determined from the Fourier components  $C^+(k, T)$ , whereas  $C^-(k, T)$  should all equal to zero. Assuming the protocol  $n_g(t)$  is nondecreasing,  $W(T)$  lies in the interval  $[0, 1]$ . Hence, it is sufficient to determine the Fourier coefficients only at wave numbers  $k = n/2$  for  $n = 0 \dots N$ , where  $N$  is a sufficiently large integer. The full density function  $\rho(W, t)$  with a  $W$ -discretization of  $2/N$  can be then obtained by Fast Fourier Transform.

# Bibliography

- [1] N. Ashcroft and N. Mermin, *Solid State Physics* (Holt, Rinehart and Winston, United States, 1976).
- [2] P. J. Mohr, B. N. Taylor, and D. B. Newell, *Rev. Mod. Phys.* **84**, 1527 (2012).
- [3] R. A. Millikan., *Phys. Rev.* **2**, 109 (1913).
- [4] *Nobel Lectures, Physics 1922–1941* (Elsevier, Amsterdam, 1965).
- [5] W. Lu, Z. Ji, L. Pfeiffer, K. W. West, and A. J. Rimberg, *Nature* **423**, 422 (2003).
- [6] S. Gustavsson, R. Leturcq, B. Simovič, R. Schleser, T. Ihn, P. Studerus, K. Ensslin, D. C. Driscoll, and A. C. Gossard, *Phys. Rev. Lett.* **96**, 076605 (2006).
- [7] T. A. Fulton and G. J. Dolan, *Phys. Rev. Lett.* **59**, 109 (1987).
- [8] L. Kuzmin, P. Delsing, T. Claeson, and K. Likharev, *Phys. Rev. Lett.* **62**, 2539 (1989).
- [9] I. Giaever, *Phys. Rev. Lett.* **5**, 147 (1960).
- [10] M. Nahum, T. M. Eiles, and J. M. Martinis, *Appl. Phys. Lett.* **65**, 3123 (1994).
- [11] M. M. Leivo, J. P. Pekola, and D. V. Averin, *Appl. Phys. Lett.* **68**, 1996 (1996).
- [12] P. Lafarge, H. Pothier, E. Williams, D. Esteve, C. Urbina, and M. Devoret, *Z. Phys B* **85**, 327 (1991).
- [13] D. V. Averin and J. P. Pekola, *Europhys. Lett.* **96**, 67004 (2011).
- [14] C. Jarzynski, *Phys. Rev. Lett.* **78**, 2690 (1997).
- [15] G. E. Crooks, *Phys. Rev. E* **1**, 1 (1999).
- [16] N. Feltin and F. Piquemal, *Eur. Phys. J. - Special Topics* **172**, 267 (2009).
- [17] R. C. Dynes, V. Narayanamurti, and J. P. Garno, *Phys. Rev. Lett.* **41**, 1509 (1978).
- [18] R. C. Dynes, J. P. Garno, G. B. Hertel, and T. P. Orlando, *Phys. Rev. Lett.* **53**, 2437 (1984).

- [19] J. Nicol, S. Shapiro, and P. H. Smith, *Phys. Rev. Lett.* **5**, 461 (1960).
- [20] D. V. Averin and K. K. Likharev, “Mesoscopic phenomena in solids,” (Nature Publishing Group, Amsterdam, 1991) pp. 173–271.
- [21] G. L. Ingold and Y. V. Nazarov, “Single charge tunneling,” (Plenum Press, New York, 1992) pp. 21–107.
- [22] M. Cohen, L. Falicov, and J. Phillips, *Phys. Rev. Lett.* **8**, 316 (1962).
- [23] S. Chaudhuri and I. J. Maasilta, *Phys. Rev. B* **85**, 014519 (2012).
- [24] P. K. Day, H. G. LeDuc, B. A. Mazin, A. Vayonakis, and J. Zmuidzinas, *Nature* **425**, 817 (2003).
- [25] Y. M. Blanter and M. Büttiker, *Phys. Rep.* **336**, 1 (2000).
- [26] M. A. Sillanpää, T. T. Heikkilä, R. K. Lindell, and P. J. Hakonen, *Europhys. Lett.* **56**, 590 (2001).
- [27] H. le Sueur, P. Joyez, H. Pothier, C. Urbina, and D. Esteve, *Phys. Rev. Lett.* **100**, 197002 (2008).
- [28] M. Meschke, J. T. Peltonen, J. P. Pekola, and F. Giazotto, *Phys. Rev. B* **84**, 214514 (2011).
- [29] J. T. Peltonen, P. Virtanen, M. Meschke, J. V. Koski, T. T. Heikkilä, and J. P. Pekola, *Phys. Rev. Lett.* **105**, 097004 (2010).
- [30] H. Pothier, S. Guéron, N. O. Birge, D. Esteve, and M. H. Devoret, *Phys. Rev. Lett.* **79**, 3490 (1997).
- [31] F. W. J. Hekking and Y. V. Nazarov, *Phys. Rev. B* **49**, 6847 (1994).
- [32] J. G. Simmons, *J. Appl. Phys.* **34**, 1793 (1963).
- [33] J. Bardeen, *Phys. Rev. Lett.* **6**, 57 (1961).
- [34] E. Prada and F. Sols, *Eur. Phys. J. B* **40**, 379 (2004).
- [35] K. Gloos, P. J. Koppinen, and J. P. Pekola, *J. Phys.: Condens. Matter* **15**, 1733 (2003).
- [36] L. D. Bell and W. J. Kaiser, *Phys. Rev. Lett.* **61**, 2368 (1988).
- [37] H. De Raedt, N. Garca, and J. Sáenz, *Phys. Rev. Lett.* **63**, 2260 (1989).
- [38] M. Prunnila, M. Meschke, D. Gunnarsson, S. Enouz-Vedrenne, J. M. Kivioja, and J. P. Pekola, *J. Vac. Sci. Technol. B* **28**, 1026 (2010).
- [39] U. Weiss, *Quantum dissipative systems* (World Scientific, 1999).
- [40] Y. V. Nazarov, *Sov. Phys. JETP* **68**, 561 (1989).
- [41] A. A. Clerk, M. H. Devoret, S. M. Girvin, F. Marquardt, and R. J. Schoelkopf, *Rev. Mod. Phys.* **82**, 1155 (2010).
- [42] J. M. Martinis and M. Nahum, *Phys. Rev. B* **48**, 18316 (1993).
- [43] J. Basset, H. Bouchiat, and R. Deblock, *Phys. Rev. Lett.* **105**, 166801 (2010).

- [44] A. O. Caldeira and A. J. Leggett, *Phys. Rev. Lett.* **46**, 211 (1981).
- [45] H. B. Callen and T. A. Welton, *Phys. Rev.* **83**, 34 (1951).
- [46] G. Falci, V. Bubanja, and G. Schön, *Z. Phys. B Con. Mat.* **85**, 451 (1991).
- [47] S. Farhangfar, A. J. Manninen, and J. P. Pekola, *Europhys. Lett.* **49**, 237 (2000).
- [48] G.-L. Ingold, H. Grabert, and U. Eberhardt, *Phys. Rev. B* **50**, 395 (1994).
- [49] L. C. Venema, J. W. G. Wildöer, J. W. Janssen, S. J. Tans, H. L. J. T. Tuinstra, L. P. Kouwenhoven, and C. Dekker, *Science* **283**, 52 (1999).
- [50] C. Wasshuber, *Computational Single-Electronics* (Springer, 2001).
- [51] C. Gorter, *Physica* **17**, 777 (1951).
- [52] C. A. Neugebauer and M. B. Webb, *J. Appl. Phys.* **33**, 74 (1962).
- [53] H. R. Zeller and I. Giaever, *Phys. Rev.* **181**, 789 (1969).
- [54] J. Lambe and R. C. Jaklevic, *Phys. Rev. Lett.* **22**, 1371 (1969).
- [55] G. J. Dolan, *Appl. Phys. Lett.* **31**, 337 (1977).
- [56] M. Tinkham, *Introduction to superconductivity*, 2nd ed. (Dover, New York, 1996).
- [57] J. Bardeen, L. N. Cooper, and J. R. Schrieffer, *Phys. Rev.* **106**, 162 (1957).
- [58] J. Bardeen, L. N. Cooper, and J. R. Schrieffer, *Phys. Rev.* **108**, 1175 (1957).
- [59] N. A. Court, A. J. Ferguson, and R. G. Clark, *Supercond. Sci. Tech.* **21**, 015013 (2008).
- [60] D. C. Ralph, C. T. Black, and M. Tinkham, *Phys. Rev. Lett.* **74**, 3241 (1995).
- [61] H. Courtois, S. Rajauria, P. Gandit, F. Hekking, and B. Pannetier, *J. Low Temp. Phys.* **153**, 325 (2008).
- [62] G. O'Neil, D. Schmidt, N. Miller, J. Ullom, K. Iwrin, A. Williams, G. Arnold, and S. Ruggiero, *J. Low Temp. Phys.* **151**, 70 (2008).
- [63] H. Jung, Y. Kim, K. Jung, H. Im, Y. A. Pashkin, O. Astafiev, Y. Nakamura, H. Lee, Y. Miyamoto, and J. S. Tsai, *Phys. Rev. B* **80**, 125413 (2009).
- [64] P. J. Koppinen, T. Kühn, and I. J. Maasilta, *J. Low Temp. Phys.* **154**, 179 (2009).
- [65] T. Greibe, M. P. V. Stenberg, C. M. Wilson, T. Bauch, V. S. Shumeiko, and P. Delsing, *Phys. Rev. Lett.* **106**, 097001 (2011).
- [66] F. Pobell, *Matter and Methods at Low Temperatures*, 3rd ed. (Springer, 2007).
- [67] P. Townsend, S. Gregory, and R. G. Taylor, *Phys. Rev. B* **5**, 54 (1972).
- [68] R. Meservey and P. M. Tedrow, *J. Appl. Phys.* **42**, 51 (1971).
- [69] D. V. Anghel and J. P. Pekola, *J. Low Temp. Phys.* **127**, 197 (2001).

- [70] J. M. Martinis, M. Ansmann, and J. Aumentado, Phys. Rev. Lett. **103**, 097002 (2009).
- [71] D. V. Averin and J. P. Pekola, Phys. Rev. Lett. **101**, 066801 (2008).
- [72] J. M. Hergenrother, M. T. Tuominen, and M. Tinkham, Phys. Rev. Lett. **72**, 1742 (1994).
- [73] H. Pothier, S. Guéron, D. Esteve, and M. H. Devoret, Phys. Rev. Lett. **73**, 2488 (1994).
- [74] B. J. van Wees, P. de Vries, P. Magnée, and T. M. Klapwijk, Phys. Rev. Lett. **69**, 510 (1992).
- [75] F. Giazotto, T. T. Heikkilä, A. Luukanen, A. M. Savin, and J. P. Pekola, Rev. Mod. Phys. **78**, 217 (2006).
- [76] J. P. Pekola, T. T. Heikkilä, A. M. Savin, J. T. Flyktman, F. Giazotto, and F. W. J. Hekking, Phys. Rev. Lett. **92**, 056804 (2004).
- [77] A. Sergeev and V. Mitin, Phys. Rev. B **61**, 6041 (2000).
- [78] V. F. Gantmakher, Rep. Progr. Phys. **37**, 317 (1974).
- [79] L. J. Taskinen, J. T. Karvonen, and I. J. Maasilta, *phys. status solidi (c)* **1**, 2856 (2004).
- [80] M. L. Roukes, M. R. Freeman, R. S. Germain, R. C. Richardson, and M. B. Ketchen, Phys. Rev. Lett. **55** (1985).
- [81] M. Meschke, J. Pekola, F. Gay, R. E. Rapp, and G. H. J. Low Temp. Phys. **134**, 1119 (2004).
- [82] F. C. Wellstood, C. Urbina, and J. Clarke, Phys. Rev. B **49**, 5942 (1994).
- [83] S. I. Dorozhkin, F. Lell, and W. Schoepe, Solid State Commun. **60**, 245 (1986).
- [84] E. T. Swartz and R. O. Pohl, Rev. Mod. Phys. **61**, 605 (1989).
- [85] S. Rajauria, P. S. Luo, T. Fournier, F. W. J. Hekking, H. Courtois, and B. Pannetier, Phys. Rev. Lett. **99**, 047004 (2007).
- [86] A. V. Timofeev, C. P. García, N. B. Kopnin, A. M. Savin, M. Meschke, F. Giazotto, and J. P. Pekola, Phys. Rev. Lett. **102**, 017003 (2009).
- [87] J. P. Pekola, D. V. Anghel, T. I. Suppala, J. K. Suoknuuti, A. J. Manninen, and M. Manninen, Appl. Phys. Lett. **76**, 2782 (2000).
- [88] A. M. Clark, A. Williams, S. T. Ruggiero, M. L. van den Berg, and J. N. Ullom, Appl. Phys. Lett. **84**, 625 (2004).
- [89] P. J. de Visser, J. J. A. Baselmans, P. Diener, S. J. C. Yates, A. Endo, and T. M. Klapwijk, Phys. Rev. Lett. **106**, 167004 (2011).
- [90] J. P. Pekola, O.-P. Saira, V. F. Maisi, A. Kemppinen, M. Möttönen, Y. A. Pashkin, and D. V. Averin, ArXiv e-prints (2012), arXiv:1208.4030 [cond-mat.mes-hall].
- [91] S. Franssila, *Introduction to microfabrication* (Wiley, West Sussex, 2004).

- [92] T. Suntola and J. Antson, *Method for Producing Compound Thin Films*, U.S. Patent #4,058,430 (1977).
- [93] Y. A. Pashkin, Y. Nakamura, and J. S. Tsai, *Appl. Phys. Lett.* **76**, 2256 (2000).
- [94] J. K. Julin, P. J. Koppinen, and I. J. Maasilta, *Appl. Phys. Lett.* **97**, 152501 (2010).
- [95] J. Pekola and J. Kauppinen, *Cryogenics* **34**, 843 (1994).
- [96] J. P. Pekola, K. P. Hirvi, J. P. Kauppinen, and M. A. Paalanen, *Phys. Rev. Lett.* **73**, 2903 (1994).
- [97] A. B. Zorin, *Rev. Sci. Instr.* **66**, 4296 (1995).
- [98] J. M. Hergenrother, J. G. Lu, M. T. Tuominen, D. C. Ralph, and M. Tinkham, *Phys. Rev. B* **51**, 9407 (1995).
- [99] T. Thornton, M. Pepper, H. Ahmed, D. Andrews, and G. Davies, *Phys. Rev. Lett.* **56**, 1198 (1986).
- [100] K. Berggren, T. Thornton, D. Newson, and M. Pepper, *Phys. Rev. Lett.* **57**, 1769 (1986).
- [101] M. Field, C. Smith, M. Pepper, D. Ritchie, J. Frost, G. Jones, and D. Hasko, *Phys. Rev. Lett.* **70**, 1311 (1993).
- [102] B. Starmark, T. Henning, T. Claeson, P. Delsing, and A. N. Korotkov, *J. Appl. Phys.* **86**, 2132 (1999).
- [103] A. B. Zorin, F.-J. Ahlers, J. Niemeyer, T. Weimann, H. Wolf, V. A. Krupenin, and S. V. Lotkhov, *Phys. Rev. B* **53**, 13682 (1996).
- [104] H. Brenning, S. Kafanov, T. Duty, S. Kubatkin, and P. Delsing, *J. Appl. Phys.* **100**, 114321 (2006).
- [105] B. A. Turek, K. W. Lehnert, A. Clerk, D. Gunnarsson, K. Bladh, P. Delsing, and R. J. Schoelkopf, *Phys. Rev. B* **71**, 193304 (2005).
- [106] A. M. Savin, M. Meschke, J. P. Pekola, Y. A. Pashkin, T. F. Li, H. Im, and J. S. Tsai, *Appl. Phys. Lett.* **91**, 063512 (2007).
- [107] O. Naaman and J. Aumentado, *Phys. Rev. Lett.* **96**, 100201 (2006).
- [108] A. F. Andreev, *Zh. Eksp. Theor. Fiz.* **46**, 1823 (1964), [*Sov.Phys. JETP* **19**, 1228 (1964)].
- [109] S. Kafanov, A. Kemppinen, Y. A. Pashkin, M. Meschke, J. S. Tsai, and J. P. Pekola, *Phys. Rev. Lett.* **103**, 120801 (2009).
- [110] M. Covington, M. W. Keller, R. L. Kautz, and J. M. Martinis, *Phys. Rev. Lett.* **84**, 5192 (2000).
- [111] S. V. Lotkhov and A. B. Zorin, *Appl. Phys. Lett.* **100**, 242601 (2012).
- [112] S. B. Kaplan, C. C. Chi, D. N. Langenberg, J. J. Chang, S. Jafarey, and D. J. Scalapino, *Phys. Rev. B* **14**, 4854 (1976).

- [113] M. W. Keller, A. L. Eichenberger, J. M. Martinis, and N. M. Zimmerman, *Science* **285**, 1706 (1999).
- [114] M. W. Keller, N. M. Zimmerman, and A. L. Eichenberger, *Metrologia* **44**, 505 (2007).
- [115] M. W. Keller, J. M. Martinis, N. M. Zimmerman, and A. H. Steinbach, *Appl. Phys. Lett.* **69**, 1804 (1996).
- [116] H. S. Knowles, V. F. Maisi, and J. P. Pekola, *Appl. Phys. Lett.* **100**, 262601 (2012).
- [117] J. Liphardt, S. Dumont, S. B. Smith, I. Tinoco, and C. Bustamante, *Science* **296**, 1832 (2002).
- [118] D. Collin, F. Ritort, C. Jarzynski, S. B. Smith, I. Tinoco, and C. Bustamante, *Nature* **437**, 231 (2005).
- [119] I. Junier, A. Mossa, M. Manosas, and F. Ritort, *Phys. Rev. Lett.* **102**, 070602 (2009).
- [120] N. Garnier and S. Ciliberto, *Phys. Rev. E* **71**, 060101 (2005).
- [121] Y. Utsumi, D. S. Golubev, M. Marthaler, K. Saito, T. Fujisawa, and G. Schön, *Phys. Rev. B* **81**, 125331 (2010).
- [122] B. Küng, C. Rössler, M. Beck, M. Marthaler, D. S. Golubev, Y. Utsumi, T. Ihn, and K. Ensslin, *Phys. Rev. X* **2**, 011001 (2012).

ISBN 978-952-60-3628-1  
ISBN 978-952-60-5076-8 (pdf)  
ISSN-L 1799-4934  
ISSN 1799-4934  
ISSN 1799-4942 (pdf)

**Aalto University**  
**School of Science**  
**O. V. Lounasmaa Laboratory**  
[www.aalto.fi](http://www.aalto.fi)

**BUSINESS +  
ECONOMY**

**ART +  
DESIGN +  
ARCHITECTURE**

**SCIENCE +  
TECHNOLOGY**

**CROSSOVER**

**DOCTORAL  
DISSERTATIONS**